Delineation of Surface Water Features Using RADARSAT-2 Imagery and a TOPAZ Masking Approach over the Prairie Pothole Region in Canada

A Thesis
Submitted to the College of Graduate and Postdoctoral Studies
In Partial Fulfillment of the Requirements for the Degree of

Master of Science

In the
Department of Geography and Planning
University of Saskatchewan
Saskatoon, Saskatchewan, Canada

By

Mohammadreza Zarcheshm

March, 2018

PERMISSION TO USE

In presenting this thesis in partial fulfillment of the requirements for a Postgraduate degree from the University of Saskatchewan, I hereby agree that the Libraries of this University may make it freely available for inspection. I further agree that permission for copying of this thesis in any manner, in whole or in part, for scholarly purposes may be granted by the professor or professors who supervised my thesis work or, in their absence, by the Head of the Department of Geography and Planning or the Dean of the College of Art and Science in which my thesis work was done. It is understood that any copying or publication or use of this thesis or parts thereof for financial gain shall not be allowed without my written permission. It is also understood that due recognition shall be given to me and to the University of Saskatchewan in any scholarly use which may be made of any material in my thesis.

Requests for permission to copy or to make other uses of materials in this thesis, in whole or part should be addressed to:

Head of the Department of Geography and Planning
Kirk Hall Building 117 Science Place University of Saskatchewan
Saskatoon, Saskatchewan S7N 5C8
Canada

OR

Dean
College of Graduate and Postdoctoral Studies
University of Saskatchewan
116 Thorvaldson Building, 110 Science Place
Saskatoon, Saskatchewan S7N 5C9
Canada

Abstract

The Prairie Pothole Region (PPR) is one of the most rapidly changing environments in the world. In the PPR of North America, topographic depressions are common, and they are an essential water storage element in the regional hydrological system. The accurate delineation of surface water bodies is important for a variety of reasons, including conservation, environmental management, and better understanding of hydrological and climate modeling. There are numerous surface water bodies across the northern Prairie Region, making it challenging to provide near-real-time monitoring and in situ measurements of the spatial and temporal variation in the surface water area. Satellite remote sensing is the only practical approach to delineating the surface water area of Prairie potholes on an ongoing and cost-effective basis. Optical satellite imagery is able to detect surface water but only under cloud-free conditions, a substantial limitation for operational monitoring of surface water variability. However, as an active sensor, RADARSAT-2 (RS-2) has the ability to provide data for surface water detection that can overcome the limitation of optical sensors. In this research, a threshold-based procedure was developed using Fine Wide (F0W3), Wide (W2) and Standard (S3) modes to delineate the extent of surface water areas in the St. Denis and Smith Creek study basins, Saskatchewan, Canada. RS-2 thresholding results yielded a higher number of apparent water surfaces than were visible in high-resolution optical imagery (SPOT) of comparable resolution acquired at nearly the same time. TOPAZ software was used to determine the maximum possible extent of water ponding on the surface by analyzing high-resolution LiDAR-based DEM data. Removing water bodies outside the depressions mapped by TOPAZ improved the resulting images, which corresponded more closely to the SPOT surface water images. The results demonstrate the potential of TOPAZ masking for RS-2 surface water mapping used for operational purposes.

Acknowledgments

I would like to begin by thanking my supervisor, Dr. Lawrence Martz, for his constant support, guidance and extreme patience throughout the entire graduation process at the University of Saskatchewan. Without his never-ending assistance it would have not been possible to complete the research required to accomplish this project. I would also like to thank my supervisory committee: Dr. Alain Pietroniro for his technical assistance over the course of my graduate studies.

I would like to acknowledge and thank my external examiner, Dr. Warren Helgason, for his comments and constructive criticism.

I would also like to thank those who provided financial support during the completion of my thesis project. Mainly, Dr. Lawrence Martz for providing a research assistantship funding. Acknowledgment is given to all members of the Department of Geography and Planning, at the University of Saskatchewan.

I would also like to acknowledge the following organizations for the contribution to this research. It include the Environment of Canada team for providing RADARSAT-2 data and the Center for Hydrology, for providing the data sources regarding this research.

Special thanks to my fellow graduate students for providing support, advice, critical remark and for making this experience I'll never forget in Saskatoon while I was away from my hometown.

Last but not least, I would like to thank my parents, and my great sisters for their continuous support and encouragement. Without your help, this journey would have been much more arduous.

Contents

List of Figures

List of tables

List of Symbols

AGRG	Applied Geomatics Research Group
AOI	Area of Interest
APT	Acquisition Planning Tool
BAQ	Block Adaptive Quantization
CCMEO	Canada Centre for Mapping and Earth Observation
DEM	Digital Elevation Model
dB	decibel
ET	Evapotranspiration
EMR	Electromagnetic Radiation
GIS	Geographical Information System
GCPs	Ground Control Points
HRV	High-Resolution Visible
INS	Inertial Navigation System
LiDAR	Light Detection and Ranging
LSI	LiDAR Services International
MLC	Maximum Likelihood Classification
MNDWI	Modified Normalized Difference Water Index
MDA	MacDonald Dett-wiler and Associates
NDWI	Normalized Difference Water Index
NAD83	North American Datum of 1983
NIR	Near-infrared
NIC	Nominal Image Coverage
NESZ	Noise-Equivalent Sigma-Zero
PPR	Prairie Pothole Region
RS-2	RADARSAT-2
RMS	Root Mean Square
RCM	RADARSAT Constellation Mission
RADAR	Radio Detection and Ranging

SCRB	Smith Creek Research Basin
SWIR	Short Wave Infra-red
SDNWA	St. Denis National Wildlife Area
SLC	Single-look complex
SLI	Side Looking Imagery
SPOT	Le Systeme pour I'Observation de la Terre
SAR	Synthetic Aperture Radar
TOPAZ	Topographic PArametriZation
UTM	Universal Transverse Mercator

Chapter 1

Introduction

1.1 Prairie Pothole Region characteristics

Almost 2.25 million square kilometers (23%) of Canada's total land area is covered by surface water in the form of rivers, ponds, and Prairie wetlands (Brisco et al., 2009). The Prairie Pothole Region (PPR), located in mid-central North America, extends over 750,000 km^2, and spans three Canadian provinces (Alberta, Saskatchewan, and Manitoba) and four American states (Montana, North Dakota, Minnesota, and Iowa) (Millet et al., 2009). The region has unique hydrology formed from physiographic characteristics that include numerous small depressions, which, along with geologic settings and atmospheric water, perform key ecological and hydrological functions (Winter, 1988). Since the topography in the Prairie region is a low-relief terrain landscape that lacks a developed drainage network, many potholes are isolated and do not contribute to streamflow (Winter et al., 1984; Brinson, 1993).

The Canadian portion of the PPR is characterized by long, cold winters (Figure 1.1). Atmospheric water (i.e., precipitation) is the most important water source for the Prairie region (Hayashi et al., 1998; Conly and van der Kamp, 2001). Average annual precipitation of less than 500 mm/year supplies water to the region. Approximately 25% to 30% of the total annual precipitation falls as snow, with continuous snow cover and frozen soils throughout most of the region (Burn, 2008; Pomeroy et al., 2009). Although snow from November to April comprises only 20% to 30% of the region's precipitation, snowmelt water is the major constituent (75% - 85%) of the PPR runoff, (Sloan, 1972; Akinremi and McGinn, 2001; Dumanski et al., 2015).

Figure 1.1 The Prairie Pothole Region (PPR) in mid-central North America (Gala et al., 2011)

The water balance of the PPR is controlled by interactions between precipitation, evapotranspiration, overland flow, and subsurface flow (Winter, 1989; Winter and Rosenberry, 1995; van der Kamp and Hayashi, 2009). Snow precipitation supplies water to the PPR by two mechanisms: first, in winter, prevailing winds redistribute snowfalls across vast areas over the PPR landscape so that more snow accumulates in the depressions than in the uplands (LaBaugh et al., 1998). Surface depressions act as a sink for blowing snow due to their low topographic elevation and the existence of vegetation in the landscape (van der Kamp et al., 2003; Fang and Pomeroy, 2008). Second, in spring, the snowmelt runoff from the uplands is trapped in depressions, increasing the surface water area and providing the majority of water that fills potholes in wetland

areas (Fang and Pomeroy 2008). Moreover, the in situ accumulated snowmelt in depressions contributes water directly to Prairie potholes in the melting season (Pomeroy and Gray, 1995; Essery and Pomeroy, 1999). The water levels of the PPR gradually decline because net evapotranspiration exceeds net precipitation in the summer, and, to a lesser extent, because of groundwater interaction. Small, shallow potholes, which are mostly seasonal or ephemeral, are dependent on net precipitation and evapotranspiration (Winter and Rosenberry, 1995).

The majority of rainfall occurs in June and July, and the source is usually convective storms, which supply intense rainfalls over small areas (Bonsal et al., 1999). Due to unsaturated soil conditions and high rates of evapotranspiration (ET), rainfall events tend to produce negligible runoff in the summer and, consequently, minimal surface runoff (Armstrong et al., 2008; Granger and Gray, 1989; Hayashi et al., 1998; Shook and Pomeroy, 2012). The Canadian Prairies are prone to drought, mainly due to their mid-continental location, their long distance from large water bodies, high potential ET, and high precipitation variability (Bonsal et al., 2013). Precipitation deficits and reduced soil moisture during drought have critical hydrological impacts on both streamflow and the replenishing of water bodies (Fang and Pomeroy, 2007).

In recent years, long-term climate variability and short-term localized human modification have impacted the PPR's water resources, making them one of the most dynamic hydrological systems in the world (Todhunter and Rundquist, 2004). Owing to its large storage capacity, the PPR can mitigate peak runoff during a flood event; however, since the late 1800s, the role of potholes in flood control has been affected by drainage, filling, leveling, and conversion to agriculture (Hayashi et al., 2003; Gleason et al., 2008). Research has suggested that increased downstream flooding on the Prairie in recent years may be largely due to human impact on drainage patterns (Hubbard and Linder, 1986; Gleason et al., 2007; Pomeroy et al., 2014).

Mapping and monitoring surface water features are essential to providing up-to-date information on the spatial and temporal variability of surface water, information that is needed to effectively manage and conserve water resources. This information can also be used as input to modeling atmospheric behavior and weather prediction in the PPR (Brisco et al., 2011). Satellite remote sensing is the only practical approach that can be used to monitor surface water efficiently and in a timely manner (Rundquist and Narayanan, 2001).

Extensive surface water monitoring can lead to a better understanding of hydrological processes in the PPR. Both RADAR and optical data can be used to monitor surface water in the PPR and can provide information on the region's high spatial and temporal variability. Some applications of multispectral optical sensors in detecting surface water are limited by cloudy sky conditions, haze, and cloud shadows (Brisco et al., 2009). However, Synthetic Aperture RADAR (SAR) and, specifically, RADARSAT-2 sensors can penetrate cloud cover and provide information about surface water, thus overcoming the limitations of optical sensors (Bolanos et al., 2016). As RADARSAT-2 is the only SAR sensor used in this study, the terms RADARSAT-2 and SAR are used interchangeably.

1.2 Research strategies and objectives

This research concerns the mapping and monitoring of surface water bodies in the Canadian PPR, which are indicators of the overall status of freshwater resources. A method is introduced for extracting surface water information from RADARSAT-2 data for the purposes of operational study.

A reliable method to estimate open surface water areas in the PPR is essential for assessing the functions and variability of these water bodies. RADARSAT-2 has been used as a tool in a

variety of locations to map open surface water activities (White et al., 2014; Bolanos et al., 2016). In this research, large coverage beam modes were selected to determine the capability of RADARSAT-2 data in detecting surface water areas over two study basins in the PPR, SK, Canada.

The grey-level RADARSAT-2 thresholding method is a common classification method to quickly and inexpensively delineate water bodies in various SAR data studies (Brisco et al., 2009; Li and Wang, 2015). Because the thresholding method offers an efficient, flexible, and user-controlled scene-specific approach, for our case studies, we chose a user-selected RADARSAT-2 threshold approach to map surface water. In the RADARSAT-2 thresholding method, all pixels with a backscatter coefficient lower than a specified threshold value in an intensity image are considered as water (Henry et al., 2006; Brisco et al., 2009; Martinis, 2010). However, RADARSAT-2 can confuse roughness, high moisture content, and the dielectric constant in soil with open surface water areas (Bolanos et al., 2016). Therefore, to prevent spurious detection of surface water areas, the RADARSAT-2 thresholding image needs to be masked. A mask is an image in which some of the pixel values are considered as zero values (non-water) and others are classified as non-zero (water). When the pixel value is zero in the mask image, the pixel value of the image is set to the background values (non-water). Surface water thresholding can be masked in different ways based on the availability of data and the characteristics of the study area. In this study, a mask image was produced using LiDAR-based DEM and Topographic PArametrization (TOPAZ) software. TOPAZ applied surface depression filling to identify the maximum surface depression areas (Martz and Garbrecht, 1998). TOPAZ was selected because it is a widely adopted and robust method for detecting maximum surface depression.

The purpose of this study is to develop and optimize delineation of open surface water using microwave remote sensing data (RADARSAT-2) in PPR. This research is intended to provide the basis for the operational context in the routine mapping and monitoring of the surface water areas in the dynamic PPR. This research examines the effects of RADARSAT-2 sensor parameters and beam mode resolution. It also addresses the impact of the landscape for mapping surface water in the PPR.

The objectives of this research are as follows

1) To develop an accurate, semi-automatic, and rapid monitoring of the PPR using RADARSAT-2;

2) To evaluate the effectiveness of the TOPAZ as a masking approach for RADARSAT-2 surface water thresholding images;

3) To examine the effect of RADARSAT-2 sensor parameters, beam mode resolution and to address the impact of the topography/landscape for mapping surface water over study areas in PPR;

4) To use the classification results to evaluate the spatial frequency distribution of potholes in the study areas.

1.3. Literature review

This chapter addresses background information and reviews previous research on the use of remote sensing technologies to collect information from surface water areas. Also presented are parameters that affect the response of surface water areas in optical and RADAR imagery, as well as the benefits and limitations of applying these technologies.

1.3.1 Background and fundamentals of Prairie Pothole Regions (PPR)

Knowing the variability of surface water in PPR would allow for a better assessment of their functions and impact on many applications, including hydrological modeling, drought and flood forecasting, and weather and climate prediction (Bolanos et al., 2015). Long-term monitoring of water level data of Prairie potholes has depicted intra or inter-annual variabilities in response to weather conditions and the atmospheric water balance (Hayashi et al., 1998; Johnson et al., 2005; Millet et al., 2009). Surface water boundaries in PPR fluctuate, depending on many factors including snowmelt, rainfall, evaporation, groundwater flow, and land use manipulation. Because water resources are becoming increasingly strained, there is an increasing need for effective freshwater resource management. For the continuous management and protection of surface water resources, PPR inventories are critical tools. Although the annual amount of precipitation has not significantly changed in the last half-century, the PPR's surface water and water storage have dramatically altered (Millet et al., 2009).

Topographic depressions or potholes are the most common physiographic characteristic of the PPR. It is estimated that about 1.5 million potholes exist in the agricultural portion of Saskatchewan, with almost 80% of them having a surface area less than 1 ha (Huel, 2000). The hummocky landscape enables surface runoff to drain into the depressions to form potholes or sloughs internally (Fang et al., 2007). These depressions are typically geographically isolated and act as closed basins (Hayashi et al., 2003). These topographic depressions are typically small and shallow, with an estimated depth of less than one meter (Huang et al., 2011). During wetter periods, increased connectivity between depressions can occur through intermittent surface-water

connections, which may result in a temporary increase in areas that contribute to streamflow (Leibowitz and Vining, 2003).

1.3.2 Spectral differences of various land cover types in optical remote sensing

Remote sensing can acquire information about the earth's surface without repeatedly physically interacting with the earth. Remote sensing has many advantages over traditional field studies methods used to monitor Prairie pothole environments. Some of the key benefits of remote sensing imagery are as follows:

1) provision of large spatial coverage of the earth's surface;
2) temporal monitoring capability (frequent revisit);
3) access to information on remote areas (ungauged basins); and
4) collection of information based on a wide range of wavelengths.

Because remote areas are typically inaccessible, taking *in situ* measurements of surface water in these regions presents challenges (Martinis et al, 2009). Unlike the satellite Remote sensing imaging, the *in situ* measurement of surface water cannot provide the data of a large spatial area in a short time. The concurrent mapping of a large area (hundreds of kilometers wide) is especially critical when the surface water extent is quickly changing due to high climate variability and the dynamic nature of most ephemeral/seasonal ponding water areas in PPR. Remote sensing provides a unique approach to overcoming these difficulties (Baker et al., 2006). One of the most significant benefits of remote sensing imaging is that, depending on the resolution and swath width of the sensor, a large area can be captured at one time with one or two images. A second benefit is that the information collected in remote sensing imagery is unbiased, as it is a consistent representation of energy interactions with a ground target. A third and even more significant

benefit is the continuous coverage that remote sensing imagery provides for monitoring the earth surface change trends (Li and Chen, 2005; Campbell, 2011). With various satellite sensors available for environmental monitoring, PPR studies can take advantage of different resolutions, image geometry, spatial coverage, and various spectral ranges to collect exactly the type of information required. Remote sensing, then, has several benefits in the mapping and monitoring of surface water areas both generally across the globe and, more specifically, in the PPR (Milton et al., 2003).

Optical sensor systems need to deal with the varying illumination conditions of the sun. These systems are considerably influenced by atmospheric conditions. Using spectral signatures of optically remotely-sensed objects allows for the earth's surface to be categorized into a number of classifications of land cover (Richards and Jia, 2006). The sensor's spectral resolution is the range of electromagnetic radiation (EMR) wavelengths that the sensor monitors. Remote sensing operates in several regions of the electromagnetic spectrum (Figure 1.2). The subranges of the measured EMR are called bands. In addition to spectral resolution, remotely sensed data depend on three other kinds of resolution: spatial resolution, temporal resolution, and radiometric resolution (Lillesand et al., 2014). Spatial resolution refers to the size of the ground area represented by a pixel in the remotely sensed data. For example, the SPOT-6 multispectral sensor has a spatial resolution of 6m, meaning that each pixel of the image represents an area on the ground 6m along the x-axis and 6m along the y-axis. Temporal resolution is a measure of how frequently a satellite passes over and collects data from the same location. Temporal resolution is measured in days and is also known as revisit time. Radiometric resolution refers to the number of computer bits available to process each pixel of the image data (Richards and Jia, 2006).

Every pixel making up the image data has an assigned numerical value called the digital number. The range of digital numbers depends on the radiometric resolution of the data (Lillesand et al., 2014). If the data are 8-bits, there will be a total of 256 values, ranging from 0 (the least bright) to 255 (the brightest).

Remote sensing records the amount of electromagnetic radiation (EMR) and is described by wavelength and frequency. Wavelength is the distance between two successive wave crests, and frequency is the number of wave cycles for a fixed period (Lillesand et al., 2014).

The visible region of the EM spectrum occupies a relatively small portion of the EM spectrum. The longer wavelengths used for remote sensing are in the thermal infrared and microwave regions (Kerle et al., 2004). Thermal infrared provides information about surface temperature, which can be related, for example, to the mineral composition of rocks or the condition of vegetation. Microwave regions can provide information on surface roughness and the properties of the surface such as water content (Kerle et al., 2004).

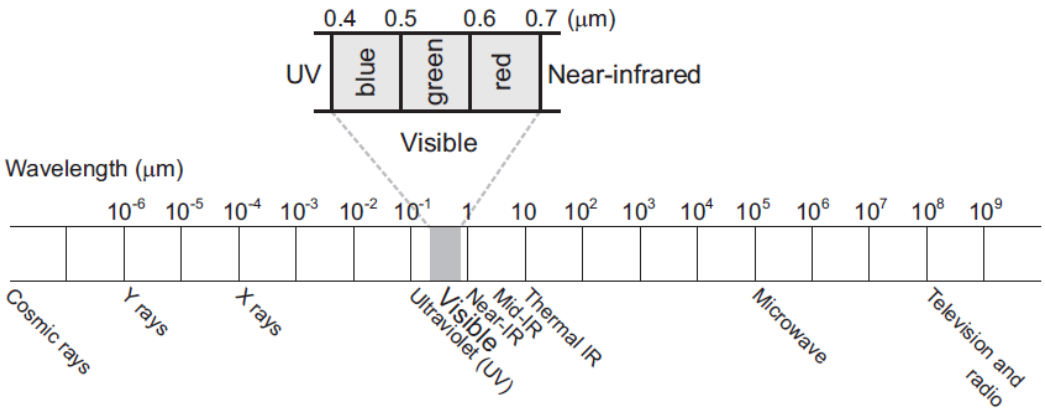

Figure 1.2 Electromagnetic spectrum shown in meter units. Short wavelengths are shown on the left, the visible spectrum in the middle, and long wavelengths on the right (ITC, 2004)

1.3.3 Mapping Prairie Pothole Region (PPR) using optical remote sensing

Remote sensing, particularly using optical images, has been used to detect features and surface water extraction based on visible-near-infrared channels (0.4 to 2 um), which help to visually identify and interpret surface water features (Campos et al., 2012; Huang et al., 2012). The classification of optical images provides useful information on land use/land cover of many study areas (Du et al., 2012; Feyisa et al., 2014; Klemas and Pieterse, 2015).

In optical remote sensing, the three main land cover types (water, land, vegetation) illustrate differences in the spectral response at various wavelengths. In optical imagery, land appears much brighter than water because water strongly absorbs the Near-Infrared wavelength and reflects little, whereas vegetation and soil reflect most of the energy they receive (Klemas and Pieterse, 2015). Consequently, areas of standing water appear dark in sharp contrast to bare soils and vegetation-covered areas, both of which look bright. In most remote sensing reference materials, generalized signature profiles are given for various land cover classes. The three distinct land cover types (vegetation, water, and soil) display differences in spectral response at multiple wavelengths. Figure 1.3 shows the typical spectral reflectance curves for three general land cover classes. In previous research, various optical satellite sensors, such as Landsat (TM & ETM+) and Pour l'Observation de la Terre (SPOT) High-Resolution Visible (HRV) instruments, have been used to detect and monitor surface water (Du et al., 2012; Campos et al., 2012; Tulbure and Broich, 2013). Since, in a given spatial and temporal resolution, the capturing of remote sensing data is repetitive, this method offers an opportunity to detect and monitor surface water in the PPR. Acquiring information over time is beneficial when the data can be captured in different images and then compared with the previous data (Coppin et al., 2004).

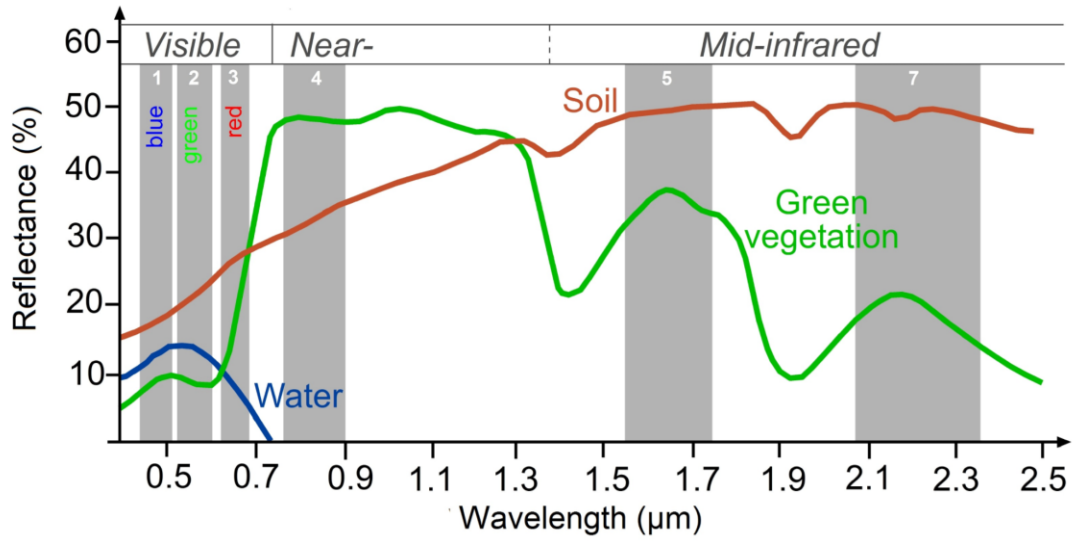

Figure 1.3 Spectral reflectivity for three common cover types of ground surface features, according to their wavelength in optical imagery in the visible and reflective infrared range; the spectral signature of soil, vegetation, and water in different bands of Landsat ETM+ image (Richards and Jia, 2006)

1.3.4 Optical-based methods for detecting surface water

Optical sensors of varying spatial, temporal, and spectral resolution have been widely used to extract and analyze information on surface water (Li and Chen, 2005). The use of these remotely-sensed data commonly starts with the classification of land use/cover types. Common water classification methods for optical imagery can be categorized into several basic categories (Ji et al., 2009):

1. thematic classification (Lira, 2006),

2. single-band thresholding (Jain et al., 2005), and

3. two-band spectral water indices (Jain et al., 2006; Xu, 2006).

Thematic classification (optical-based delineation) is often performed using supervised Maximum Likelihood Classification (MLC) with predefined training areas (Sawunyama et al., 2006; Ran et al., 2012). This method needs cloud-free conditions and yields good results in delineating the water surface. Single-band thresholding and two-band indices are commonly used in surface water extraction methods because they are easy to use and are computationally less time-

consuming than alternative approaches (Ryu et al., 2002; Feyisa et al., 2014). Regarding two-band indices, McFeeters (1996) introduced the Normalized Difference Water Index (NDWI) to delineate open water features using the green (band 2) and near-infrared (band 4) of Landsat ETM+. McFeeters (1996) proposed a threshold of 0 for extracting surface water using the raw digital number (DN) of Landsat, where all positive NDWI values would be classified as water and negative values as non-water. Xu (2006) proposed another index, called Modified Normalized Difference Water Index (MNDWI), where McFeeters (1996) NDWI was modified by replacing NIR (band 4) with SWIR (band 5) of Landsat ETM+. The MNDWI of Xu (2006) is one of the most widely-used water indices for various applications, including surface water detection and monitoring, land use/cover change analyses, and ecological research. The breakdown of multispectral sensors used in the literature for surface water mapping is presented in Table 1.1.

Table 1.1. Overview of the literature on the mapping of surface water areas using multi-spectral remote sensing for surface water studies

Reference	Applied Method	Optical Sensor	Study area
Water Surface Variation Monitoring and Analysis (Huang et al., 2012)	Integrated threshold method	Terra/MODIS	Dongting Lake, China
Performance of normalized difference water indexes in detecting water (Campos et al., 2012)	normalized different water index (NDWI)	Landsat 7 ETM+	Gorgol, Akhdar and Garfa basins, Muritania
Estimating surface water area changes (Du et al., 2012)	normalized different water index (NDWI), the modified NDWI (MNDWI), and Otsu image segmentation	Landsat ETM+	Qingjiang River basin, China
Spatiotemporal dynamic of surface water bodies (Tulbure and Broich, 2013)	A decision-tree classification algorithm	Landsat TM and ETM+	Southwest Western Australia
Mapping wetlands using optical, RADAR and DEM data (Li and Chen, 2005)	A rule-based method	ETM+ & RADARSAT-1	Eastern Canada

1.4 Principles of RADAR remote sensing

The ability of multispectral sensors to collect optical imagery can be inhibited by cloud cover, thus possibly missing the critical post-snow melt for surface water inventory (Li and Wang, 2015). Radio Detection and Ranging (RADAR) data can provide exclusive information about surface features beyond the spectral response measured with optical data. Long-wave RADAR signals are not sensitive to atmospheric conditions, do not require daylight hours for acquisition, and can provide images of the earth's surface during both day and night, thereby increasing the possibility of frequent data collection (Hess et al., 1990; Parmuchi et al., 2002). The sensor's ability to penetrate cloud cover and detect surface water areas makes the RADAR system a powerful tool for surface water monitoring throughout the PPR (Townsend, 2002). A RADAR sensor uses its own energy source, transmits signals towards the earth's features, and measures backscattered wavelengths to the sensor, and, in this way, gathers information from the earth's surface (Henderson and Lewis, 1998). Electromagnetic (EM) pulses are transmitted with a specific frequency, amplitude, and polarization. After the waves interact with an object, part of the energy of the wave is reflected back and its amplitude and arrival time is recorded at a specific polarization (Lillesand and Kiefer, 2014). These measures are sensitive to the dielectric and geometric characteristics of the object, making it possible to separate surface features.

RADAR systems used in imaging require several components: a transmitter, a receiver, an antenna, and a recorder. The transmitter is used to generate the microwave signals and transmit the energy to the antenna from where it is emitted towards the earth's surface. The recorder then stores the received signal. The RADAR system acquires an image in which each pixel contains a digital number based on the power of the backscattered energy received from the ground. The energy

received from each transmitted RADAR signal can be represented using the so-called RADAR equation (Lucas LF Janssen et al., 2004):

$$P_r = \frac{G^2 \lambda^2 P_t \sigma}{(4\pi)^3 R^4}, \quad \text{(eq 1.1)}$$

Where

- P_r is the received energy,
- G is the antenna gain,
- λ is the wavelength,
- P_t is the transmitted energy,
- σ is the RADAR cross-section (a function of the object characteristics and the size of the illuminated area),
- R is the range from the sensor to the object.

RADAR image resolution depends on the antenna length, frequency, and the distance to the target. The RADAR beam width is proportional to the wavelength and inversely proportional to the antenna length. Thus, the longer the antenna, the narrower the beam, and the higher the spatial resolution of RADAR (Chan and Koo, 2008). Antenna length would be a serious limitation to the practicality of either an airborne or space-borne sensor, as the antenna lengths necessary would be extremely large. Specific properties of the RADAR pulse allow engineers to use the known details of the RADAR satellite's orbit to synthesize a much longer virtual antenna (Lee and Pottier, 2009). This system is known as Synthetic Aperture RADAR (SAR); a SAR sensor will have a short physical antenna but will have the resolution capabilities as if it possessed an antenna several kilometers long (Lee and Pottier, 2009).

1.4.1 Land/ Water boundary delineation using RADAR

In many surface water studies, RADAR has been considered a useful tool for detecting surface water and monitoring open water dynamics (Brisco et al., 2009; Kuenzer et al., 2013; Lu et al., 2014; Martinis et al., 2009; Bartsch et al., 2012). Due to its all-weather capabilities and sensitivity to the specular reflectance characteristics of water, RADAR is recognized as a reliable data source for the characterization of the Prairie region's hydrology (Töyrä et al., 2002; Töyrä and Pietroniro, 2005; Brisco et al., 2009; Manjusree et al., 2012). To detect the extent of a water body's surface, ideally the water surface is smoother than the surrounding land (Martinis et al., 2009). The RADAR backscatter from water is very low and reflects most radiance away from RADAR sensors, so mapping a wet surface is facilitated using RADAR images (Manjusree et al., 2012; Horritt et al., 2003). Consequently, areas of standing water appear as dark tones in sharp contrast to bare soils or areas covered by vegetation, which look brighter in RADAR images (Baldassarre et al., 2011; White et al., 2015). A high contrast between water and land enhances the suitability of RADAR images for hydrological studies because the system can define water boundaries and delineate inundated areas (Pietroniro et al., 1999; Li and Wang, 2015).

1.4.2 RADARSAT-2 characteristics in surface water delineation

The RADARSAT-2 is a Canadian earth observation satellite, among the most widely-used active sensor satellites for water surface and flood mapping. RADARSAT-2 is operated at a single, dual, and fully Polarized C-band microwave at about 5.5 GHz with a resolution up to 3m. The satellite was launched in 2007 for continuity with the RADARSAT-1 mission, which was launched in 1995 and is still operational. The RADARSAT-2 satellite has more capabilities than RADARSAT-1. These capabilities include additional beam modes, higher resolution, multi-polarization, an increased downlink margin, more frequent revisits, and lower-cost receiving

stations. The operation modes have also been extended, adding a full Polarimetric mode to increase the information content. The more frequent revisit period enhances the operational capabilities of the satellite (Brisco et al., 2008).

The RADARSAT-2 mission was designed and constructed with co-operation between Canadian Space Agency (CSA) and private industry (MacDonald Dett-wiler and Associates Ltd. (MDA)). The RADARSAT-2 can acquire data at four different polarizations: horizontal (HH), vertical (VV), and cross (HV & VH) polarizations. Because HH polarization shows better land and water discrimination, it is preferred for surface water mapping (Sokol et al., 2004; Henry et al., 2006, Martinis et al., 2009; Gan et al., 2012). HH has a lower backscatter to wind-induced surface roughness on open water and is therefore preferred over VV for mapping open water if wind speed data or in situ water surface features are not available (Brisco et al., 2008). Over smooth water surfaces, like-polarization (e.g., HH) offers improved land/water separation compared to cross-polarization (Henry et al., 2006; Schumann et al., 2007; Martinis, 2010). As the numbers of sensors and knowledge of this technology increases, RADARSAT-2 imagery is becoming more widely adopted for PPR studies. The proper selection of wavelength and sensor characteristics is important as they dictate what information can be extracted from the images. A more detailed description of RADARSAT-2 is provided by Uher et al., (2004), Morena et al., (2004), and the MDA and CSA websites:

1. (https://mdacorporation.com),
2. (http://www.space.gc.ca/asc/eng/satellites/RADARSAT/),
3. (http://www.asc-csa.gc.ca/eng/satellites/RADARSAT/).

1.4.3 Influence of the dielectric constant and surface roughness in backscattered RADAR signals

RADAR sensors emit waves from their antenna and record the backscatter of the imaged surface. The brightness of pixels in a RADAR image depends on the strength of the backscattered signal. The amount of energy that is backscattered depends on various factors; a key parameter that influences microwave backscatter behavior is the dielectric constant, a parameter that indicates the reflectivity and conductivity of a material and describes the electrical properties of the surface features (Martinis et al., 2009). By convention, grey scale tones in the image represent reflectivity, while bright tones represent high reflectivity. The moisture content of the terrain features affects the electrical properties and therefore the dielectric constant. The RADAR sensor is very sensitive to the presence of water because its dielectric constant is high and the reflectivity increases with increasing soil moisture content (Henderson and Lewis, 1998). Moreover, topography also affects the magnitude of backscatter from a given target area. Increased surface roughness leads to increase backscatter values of the transmitted RADAR signal (Mason et al., 2007). The backscatter of water bodies may behave differently depending on parameters such as RADAR wavelength, incidence angel, polarization, topography, and physical composition of the surface feature (Manjusree et al., 2012).

1.4.4 RADAR backscatter of smooth open water and flooded vegetation

Surface scattering is the primary scattering mechanism due to the low penetration depth of microwaves in the water. An open water body may be simplistically modeled as a perfectly smooth surface with a high dielectric constant, which acts as a specular reflector directing the incident microwave radiation away from a RADAR sensor (Horritt et al., 2003, Mason et al., 2007). The

specular reflectance occurs when RADAR signals interact with open inundated water, and the RADAR signals are reflected away from the satellite sensor.

The backscatter increases over a water surface may not only be induced by waves but also by riparian and flooded vegetation. These areas contrast with the brighter intensities of the rougher surrounding terrain, which is characterized by increased diffuse surface scattering. The penetrated RADAR pulse is backscattered from the horizontal water surface and lower sections of the vegetation, especially in the boundary of land and water, resulting in a strong signal return (Martinis, 2010) (Figure 1.4). However, the signal return from flooded vegetation is very complex and strongly depends on the system's wavelength, the canopy type and structure, and the polarization factor (Hong et al., 2010). Changes in the electrical properties impact the absorption, transmission, and reflection of microwaves, meaning that the moisture content of the surface is an essential component of the total scattering. The type of backscatter, ranging from specular to diffuse, and the strength of the backscatter depend on the surface roughness of the material. The double-bounce effect leads to brighter returns from the flooded vegetation areas in contrast to the very low returns from the non-flooded areas due to specular reflection from smooth water surfaces (Martinis, 2010). Specular and double-bounce scattering are two types of scattering that can be recognized for the detection of surface water areas:

1) Specular scattering (no return to the RADAR sensor) occurs from smooth surfaces. Bright pixels illustrate a high surface roughness, and dark pixels usually indicate flat and smooth surfaces such as open, calm surface water. This distinction occurs because for flat and smooth terrain the local incidence angle is approximately the same as the reflection angle, meaning that most of the signal is reflected away from the RADAR sensor (Martinis, 2010). In this context, "smooth" means the surface roughness is on a scale smaller than the RADAR pulse wavelength

(Finnigan, 2013). On the other hand, rough surfaces reflect the signal in all directions, and a significant portion returns to the RADAR (Figure 1.5).

2) Double-bounce scattering implies that the transmitted RADAR signal has not only been reflected by the surface of the terrain features but also by the objects below the surface, e.g., water beneath the canopy (Henderson et al., 1998). This type of scattering typically occurs when smooth surface water is surrounded by a visible vertical emergent vegetation cover (Hess et al., 2003; Brisco et al., 2008; Brisco et al., 2013; White et al., 2015). The RADAR signal is scattered in different ways, depending on the above-mentioned characteristics of the signal and object.

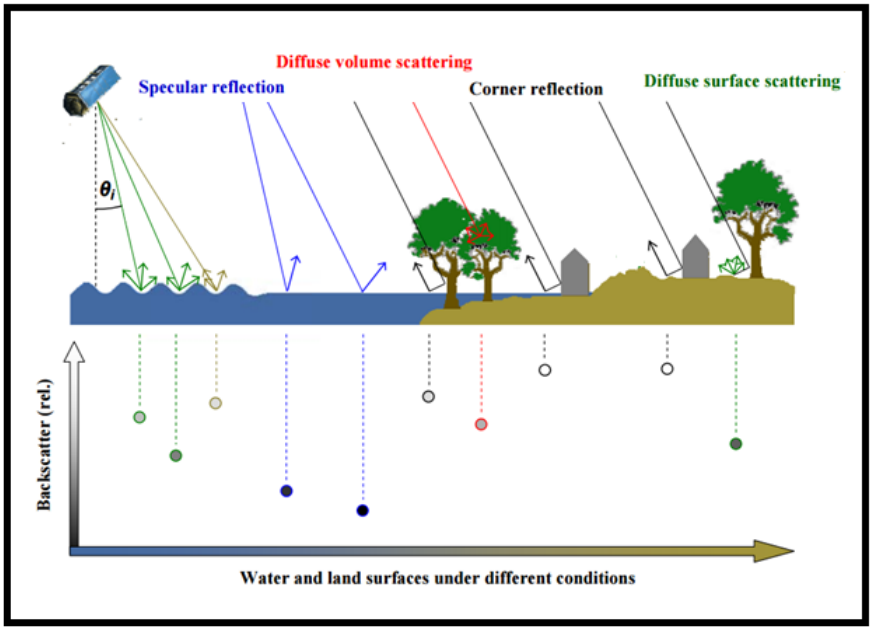

Figure 1.4. Scattering mechanisms of water and land surfaces (Martinis, 2010)

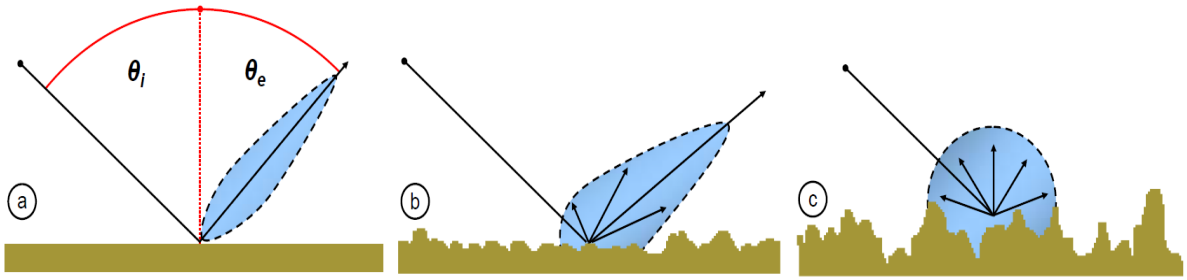

Figure 1.5. RADAR reflection of a) smooth, b) moderately roughened, and c) strongly roughened surfaces (Martinis 2010).

1.4.5 RADARSAT-2 beam modes

The RADARSAT-2 satellite offers a wide range of beam modes well suited to monitor surface water over PPR. RADARSAT-2 has all of the RADARSAT-1 imaging beam modes plus the addition of new modes such as ultrafine, multi-look fine, fine quad-polarization, and standard quad-polarization (Morena et al., 2004). Figure 1.6 illustrates the RADARSAT-2 beam modes of operation. Based on an investigation on water mapping in an operational way by the Canada Centre for Mapping and Earth Observation (CCMEO), the use of Fine resolution with Wide extent beam modes could provide the best trade-off between coverage and detail for surface water mapping (Brisco et al., 2009). Figure 1.7 indicates the available beam positions for each beam mode (in parentheses), where each beam position is related to a particular satellite imaging configuration, concerning swath width, pulse bandwidth, incidence angle, and physical RADAR beam(s) used (MDA, 2016). For a list of all available RADARSAT-2 sensor parameters and modes, refer to Appendix A.

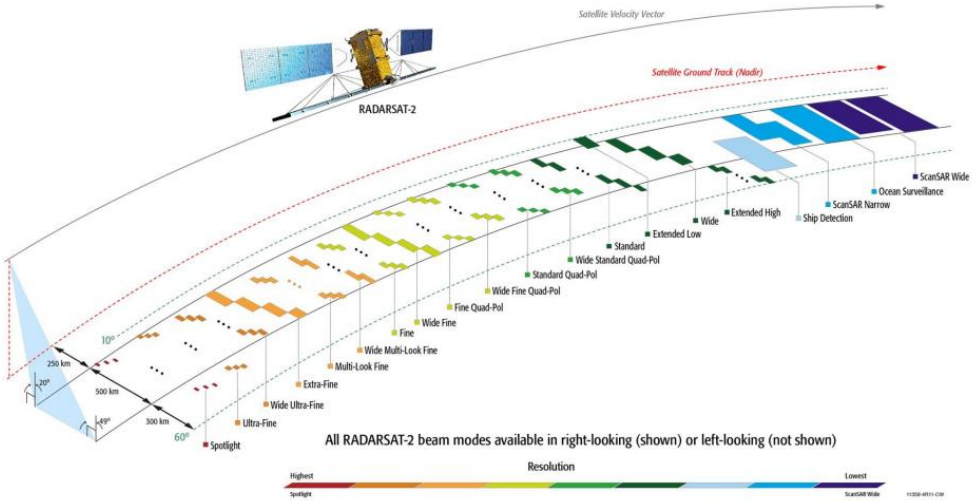

Figure 1.6 RADARSAT-2 operational beam modes (MDA, 2016)

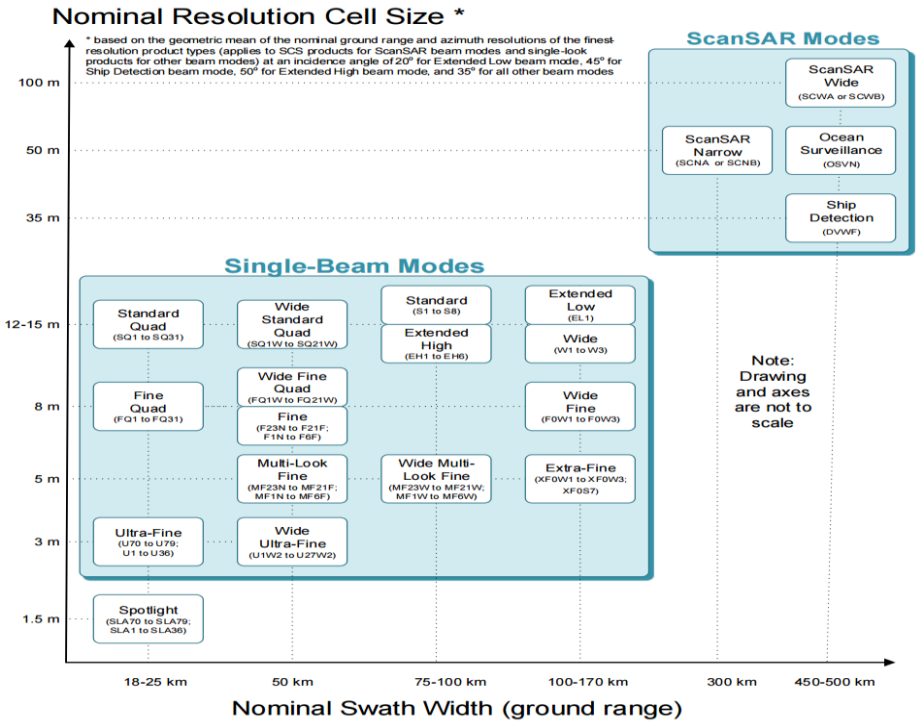

Figure 1.7. Sensor Modes, Beam modes and Beam Positions in terms of their Nominal Swath Width and achievable Product Resolution (MDA, 2016)

1.4.6 Polarization of RADARSAT-2 signal

The polarization of an electromagnetic wave is important in the field of RADAR remote sensing. Depending on the orientation of the transmitted and received RADAR wave, polarization will result in different images. The RADARSAT-2 sensor can send and receive the (H) or (V) polarization (Figure 1.8); therefore, there are four polarization combinations (HH, HV, VH, and VV), where the first letter represents the transmitted polarization and the second is for the received polarization. HH and VV are called co-polarizations (Dual-channel), whereas HV and VH are cross-polarizations. It is possible to work with horizontal, vertical, or cross-polarized RADAR waves.

Using different polarizations is critical in the collection of information for particular applications. The choice of polarization plays an important role in detecting open water areas. The satellite antenna can be tuned to receive only the portions of the returning microwave pulses that are in either a horizontal or vertical orientation. HH polarization provides the most obvious discrimination between water and other types of land cover classes (the highest distinction in backscatter values) and often is the best choice for mapping surface water because it is not as sensitive to small vertical differences in water caused by waves (Ahtonen et al., 2004, Schumann et al., 2007 ; Baghdadi et al., 2001). Thus, HH-polarized images are considered more efficient for water detection than VV or cross-polarized images (Henry et al., 2006).

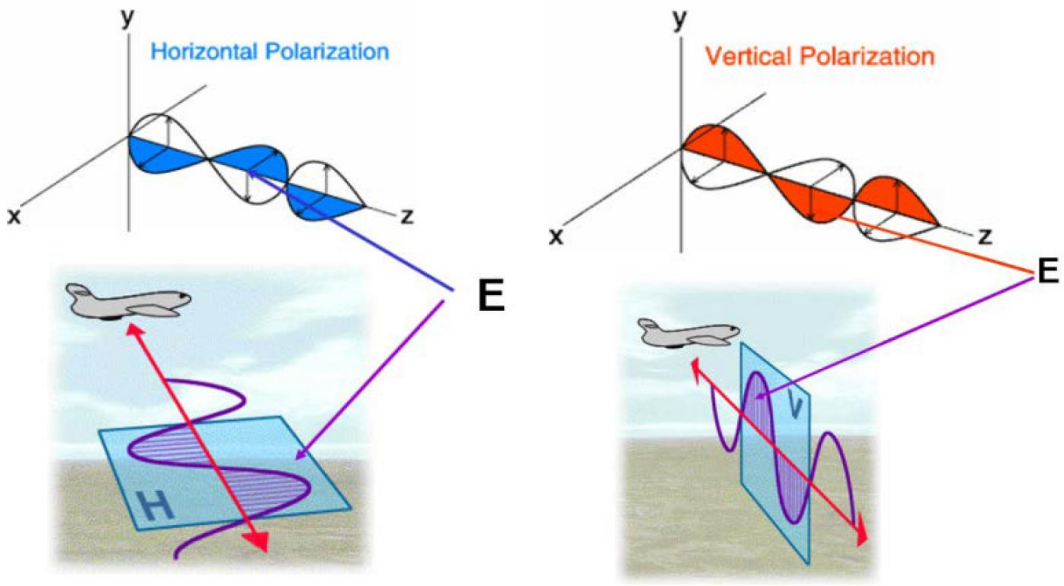

Figure 1.8 RADAR horizontal (H) and vertical (V) wave polarizations. (CCRS, 2008)

1.4.7 RADAR geometry and spatial resolution

After the transmitted signal is scattered back to the sensor, the travel time, backscatter power, and phase are compared to the original pulse. Typically, over a thousand pulses are coherently averaged to form a single pixel. With a RADAR image, the location of each pixel and its resolution is a combination of the time it took to be scattered back to the sensor (x, range resolution) and the time between two pulses relative to the platform velocity (y, azimuth resolution). Due to the different parameters that determine the spatial resolution in range and azimuth resolution, the spatial resolution in the two directions is clearly different (Geomatica SAR training guide, 2016). For RADAR image processing and interpretation, it is useful to resample the image data to regular pixel spacing in both directions. In the case of RADARSAT-2, this spacing can be 8m × 8m in Fine Wide beam mode or 30m × 30m in Wide and Standard mode,

depending on the parameter setting in the processing software (Geomatica SAR training guide, 2016).

The distance line between the RADAR antenna and surface features is called slant range. But the true horizontal distance along the ground corresponding to each measuring point in slant range is called ground range. The portion of the image that is closest to the nadir track of the satellite carrying the RADAR is called near range, while the farthest part of the image from the nadir is called far range (Kerle et al., 2004). Because it takes more time for a RADAR pulse to reach the far range of the RADAR swath, the slant-range resolution is coarser at the far range than the near range (Figure 1.9). Slant-range geometry is the natural result of RADAR-range measurements. In slant range, the spatial resolution is defined as the distance that must separate two features on the ground to give two different echoes in the return signal. The spatial resolution also refers to the ability of the RADAR sensor to discriminate between two spatially adjacent objects on the ground. It is preferable to convert the data from slant range to ground-range geometry, which is often characterized by square pixels. This conversion is usually done using a resampling of the data when it is geocoded. Transformation to the ground range is required at each data point to compensate for incidence angle and local terrain slope and elevation. This is especially true for wide-swath modes, when the swath spans more than hundreds of kilometers (Lee and Pottier, 2009).

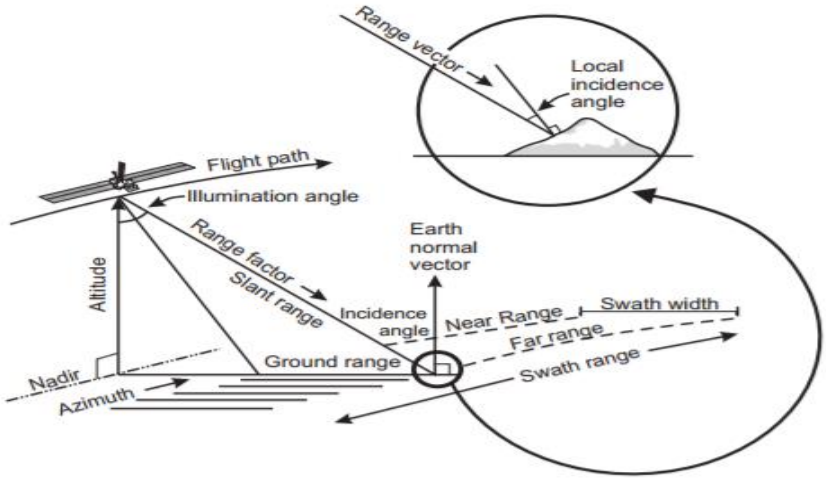

Figure 1.9. RADAR remote sensing geometry (ITC, 2004)

1.4.8 RADAR speckle noise and filters

Speckle noise is a phenomenon that has emerged as a dominant factor in all RADAR imaging systems. Speckle noise, which has a grainy, salt-and-pepper appearance, is formed because the signal is subjected to the random conflict between coherent returns coming from different scatters appearing on a surface (Lee, 1981). In reality, speckle noise is not a noise effect but rather the result of constructive and destructive interferences between the complex returns from the RADAR signal scatters (Sheng and Xia, 1996). However, these speckle features can inhibit the interpretation of accurate images and can create complexities in RADAR image processing. They therefore have to be eliminated.

Speckle filters are used primarily with RADAR data to remove high-frequency noise (speckle) while preserving high-frequency features (edges) (Woodhouse, 2006). There are several types of speckle filters that apply to the parameters of the whole image. The ideal speckle-reduction filter reduces the speckle but loses minimal information. The filter should preserve radiometric information in homogeneous areas. Adaptive speckle filters are designed specifically for RADAR

images to accommodate changes in local properties of the terrain backscatter (Zhang et al., 2012; Long et al., 2014). They modify the image based on statistics extracted from the local environment of each pixel. The main advantage of SAR adaptive filters is that they maintain an accurate estimate of the backscattering coefficient inside homogeneous (stationary) areas, such as surface water bodies, while preserving edge and texture structure in nonstationary scenes (Geomatica SAR training guide, 2016). Examples of SAR adaptive filters are the Frost, Lee, FGamma, and Touzi filters (Frost et al., 1982; Lee et al., 1994).

1.5 RADAR-based methods for detecting surface water

The first algorithm for water detection and extent mapping with RADAR was introduced by Lowry et al., (1979) and has continued to be developed ever since. Among different sources of information for monitoring surface water, the potential of the RADARSAT data has been demonstrated by several previous investigations (Hess et al., 2003; Gala and Melesse, 2012; Gan et al., 2012), and it has been used as a tool in a variety of locations (Brisco et al., 2008; Brisco et al., 2009; White et al., 2014). The most noticeable studies in surface water mapping using RADAR techniques include the following: pixel-based segmentation (Martinis et al., 2009); active contouring-based statistical methods (Hahmann et al., 2010; Heremans et al., 2003); and histogram thresholding approaches (Inglada and Mercier, 2007; Brisco et al., 2009; White et al., 2014; Li and Wang, 2015; Bolanos et al., 2016). An assessment of the various technical methods and a review of previous studies in surface water mapping are discussed here.

1.5.1 RADAR pixel-based, segmentation-based, and object-based classifications

Conventional classification approaches may be based on pixels or segments as the smallest components of raster data and smallest processing units to extract the water bodies from RADAR imagery. Three approaches used to detect water bodies in RADAR data are pixel-based classification, segmentation-based classification techniques (Heremans et al., 2003), and object-based classification. Pixel-based classification uses the brightness or backscatter coefficient of the pixel as the smallest processing unit of raster data. The classification results may exhibit a salt-and-pepper effect, making filtering necessary. A texture-based method for pixel-based classification has been developed for surface water mapping, which makes use of textural variation based on statistics. Texture-based classification uses textural properties, such as local data range, mean, variance, homogeneity, and gray values computed from a small pixel window (Blaschke et al., 2004). Texture-based classification is especially promising for high-resolution RADAR sensors as these images have a very high spectral variance due to the reduced mixed pixel phenomenon. A drawback, however, is the high processing demand and possible blurring of the water-land boundary if the method is used for medium or low-resolution images (Hahmann et al., 2010). Another limitation is threshold value selection, which is necessary to classify water but can be challenging when it comes to choosing the proper window size and the best texture measure (Di Baldassarre et al., 2011; White et al., 2015). In some studies, RADAR textural analysis algorithms for edge detection were used to improve the extraction of the land and water boundary (Touzi et al., 1988; Chen and Shyu, 1998). In one study, Li and Wang (2014) used a RADAR texture-based thresholding method and applied k-means classification results to ensure that there were sufficient pixels for water and land classes to distinguish water bodies from land. Some problems with pixel-based image analysis can be solved by using image segmentation.

Like pixel-based approaches, segmentation-based classification is also commonly used. Segmentation refers to the partitioning of an image into non-overlapping homogeneous regions based on similarity criteria of gray values or textural properties. The objective is to generate segments that resemble real objects on the earth's surface (Pal et al., 1993). Segmentation methods appear promising, especially for data of high-resolution RADAR sensors. Commonly, segmentation of RADAR images classifies them into two categories: one based on gray levels and the other based on texture (Al-Bayati and Zaart, 2013).

Object-based classification uses objects or segments as the smallest processing unit. First, the image segmentation is performed before classification takes place. Based on brightness and spatial continuity, pixels are merged into segments, after which the segments are classified. To perform the segmentation, this technique requires input parameters related to shape, smoothness, and compactness. The main restriction of this approach is that user interaction is necessary for the selection of training samples for land and water areas (Heremans et al., 2003). Object-based classification is thus used less often than pixel- and segmentation-based classification techniques to delineate surface water.

1.5.2 RADAR active contour classification

Another method applied for water and flood boundary detection in RADAR images is the active contour model. Active contour modeling has found many applications in surface water and flood mapping (Horritt et al., 2003; Hahmann and Wessel, 2010). This method uses local tone and texture values to delineate features. There are two types of active contour methods: parametric and geometric models. The parametric model is expressed as parametric curves and the geometric model as two-dimensional functions. Parametric models, also called snakes, use an iterative

algorithm to extract the desired contours (Hahmann and Wessel, 2010). However, geometric models have a significant advantage that allows natural and numerically stable topological change (Modava and Akbarizadeh, 2017). In both parametric and geometric models, active contours are curves that are developed to recover object shapes in 2D digital images. Active contour models (or snakes) are statistical models that find boundaries from noisy images. The active contour modeling takes local statistics (mean and variance) around the snake into account. The snake is put over an approximately homogeneous area (represented by a closed discrete contour of linked nodes, which is the one to be delineated). The snake is driven by an iterative algorithm, which uses a certain energy function to find boundaries in the image based on pixel intensities and the smoothness of the boundary (Hahmann and Wessel, 2010). Effectively, this energy function corresponds to the minimization of energy integrated over the contour, which often favors smooth contours. A rough map of the water bodies is necessary for initialization of the snake. Statistical active contour modeling has been successfully applied by Horritt et al. (2003) and Ahtonen et al. (2005) to flood delineation. The algorithm implementation of the active contour model requires the digitization of a few starting points situated inside the object (i.e., water bodies) to be detected (Hahmann and Wessel, 2010). Some studies use an object-oriented classification technique that applies an active contour algorithm to detect surface water areas on RADAR images (Heremans et al., 2003; Horritt et al., 2003; Silveira and Heleno, 2009). A critical limitation of the active contour method is that a long processing time is needed for parameter adjustment. Thus, this method cannot be appropriately used for operational and near-real-time processing purposes.

1.5.3 RADAR image thresholding approach

The thresholding method in RADAR imagery is the most straightforward and one of the most popular approaches used to delineate waterbodies from land (Brivio et al., 2002; Brisco et al., 2009; Martinis et al., 2010). Whether thresholding procedures apply to surface water detection using RADAR sensors depends on the contrast between the surface water and upland areas. This method is computationally very fast, and most of the extent of a smooth water surface can be derived by this technique (Martinis et al., 2009). In this method, all features with a backscatter coefficient lower than a specified threshold in an image are considered as a water area (Hess et al., 1995, Henry et al., 2006). The thresholding approach is scene specific and has to be defined for each single RADAR image separately (Martinis et al., 2010). The threshold value can be determined by visually inspecting image backscatter histograms, quickly checking the classification results, and, if necessary, refining the threshold until the classification result is visually satisfactory (Brisco et al., 2009). Extensive research has been conducted on semi-automatic or automatic thresholding of RADAR imagery (Brisco et al., 2009; Fan and Lei, 2012; Hahmann and Wessel, 2010; Solbo et al., 2003). Bolanos et al., (2015) used the threshold-based procedure and complemented it with a texture-based indicator to delineate and map locations of the extent of surface open water bodies using RADARSAT-2 in the PPR. Brisco et al. (2009) used a scene-specific automatic estimated threshold value for HH polarized backscatter to map surface water.

In addition to the thresholding approach, several other methods have been established to improve water detection results using RADAR data. Other approaches have been integrated with the thresholding method to improve water classification techniques. These methods incorporate the image-thresholding method, using a contour tracing algorithm over the RADAR images to

enhance the land-water boundary delineation (Heremans et al., 2003; Billa, 2012). However, the main limitation of these approaches is that a user interaction is necessary to select training samples for land and water (Hahmann et al., 2010), and the algorithm relies on ancillary data such as morphological operators (Bolanos et al., 2015). A limitation of the thresholding method is that the threshold needs to be modified on a scene-per-scene basis and to be individually set for every RADAR scene (Hahmann et al., 2009; White et al., 2014; Bolanos et al., 2015). Most applications of thresholding methods have been limited to specific areas with calm, open water and a specular backscatter response (Pulvirenti et al., 2011). An overview of the literature on SAR sensors used for surface water mapping is presented in Table 1.2.

Table 1.2. Overview of the main procedures in the literature to map surface water areas using SAR data

Reference	Applied Method	SAR system	Study area
Multi-sensor approach to wetland flood monitoring (Toyra et al., 2005)	Mahalanobis distance classification, combination of sensors	RADARSAT-1 and SPOT	The Peace-Athabasca Delta (PAD), Alberta
Semi-automatic tool for surface water mapping (Brisco et al., 2009)	Thresholding	RADARSAT-1	Cache Lake in Tuktut Nogait National Park, Northwest Territories
Operational flood detection (Martinis, 2009)	Histogram thresholding, Pixel- based segmentation classification	TerraSAR-X	Tewkesbury basin, Southwest England
Surface body detection (Hahmann, 2010)	Active contour models	TerraSAR-X	Lake Forggensee and Ammersee, Germany
Automatic mapping of inland surface water bodies (Li and Wang, 2015)	Modified Otsu thresholding	QuadPol RADARSAT-2	Spiritwood valley, Manitoba, Canada
Beam mode selection for surface water mapping (White et al., 2014)	Intensity channel thresholding	Fine Quad-Pol, Wide Ultra-Fine, and Spotlight, RADARSAT-2	Smith Creek study basin, SK, Canada
Evaluation of C-band for wetland mapping (Brisco et al., 2011)	Polarization diversity and polarimetry (Cloude Pottier decomposition)	CV-580, SIR-C	Minnedosa pothole region, Southwestern Manitoba, Canada
Monitoring PPR with an integrated optical and RADARsat-1 data (Gala and Melesse, 2012)	Density slicing of ETM-5, Fuzzy thresholding	Landsat ETM+, RADARSAT-1	Allan Hills, , Saskatchewan, Canada
Evaluation of RADARsat-2 Acquisition modes for wetland monitoring (Brisco et al., 2015)	Interferometric SAR (InSAR)	RADARSAT-2	Southern Florida, US
Operational surface water detection and monitoring (Bolanos et al., 2016)	Thresholding and a texture based indicator procedure	RADARSAT-2	Alberta and Saskatchewan, Canada
Automatic detection of inundated areas (Heremans et al., 2003)	Object-oriented classification and Active contour algorithm	ENVISAT/ASAR	Schulens lake in Flanders, Belgium

1.6 RADAR-Optical integrated approaches

The combination of RADAR and optical sensors is a promising approach, as together they provide complementary information (Ramsey et al., 2009). Li and Chen (2005) used a rule-based decision tree to classify Prairie wetlands into three different study sites, using optical images, RADARSAT-1, and topographic (DEM) data. Using this decision tree, the authors integrated decision rules' classification algorithms based on optical images, and, using RADAR data, they were able to distinguish between land and water in the PPR. This study has been shown to be suitable for surface water mapping (Brisco et al., 2011) Other investigations by Henderson and Lewis (2008) and Brisco et al. (2011) also found that both RADAR and optical data, as well as a digital elevation model (DEM), can assist in accurate surface water monitoring.

The RADARSAT-1 (S1) and SPOT combination have contributed complementary data to produce significantly better classification results than when these techniques are used on their own (Töyrä et al., 2001). Toyra and Pietroniro (2005) used a combination of RADARSAT-1, SPOT, and LiDAR to create a flood duration map from 1996 to 2001 and compared it with the satellite-based land cover map. As might be expected, this comparison illustrated a relationship between the spatial distribution of vegetation classes and the spatial-temporal pattern of flooding.

1.7 LiDAR-based DEM and TOPAZ

The Light Detection and Ranging (LiDAR) system is mounted on an aircraft and integrated with the Inertial Navigation System (INS) systems and Global Positioning System (GPS). In the LiDAR system, first, a laser pulse is sent from a transmitter, and a receiver collects the photons that are scattered back to it. Finally, the range is computed by the travel time between the pulse and the return of a signal. The Digital Elevation Model (DEM) is a data source that has a large

spatial extent and can provide information on Prairie pothole landscape characteristics, such as area and depth. DEMs are essentially a grid of elevation values. Traditional GIS analysis, such as "filling" the depressions, artificially raises the elevation value of the depression to the elevation of the surrounding cell (Jenson and Domingue, 1988). Recent advances in data acquisition through LiDAR data have provided DEMs with sub-meter spatial resolution and vertical accuracy. With LiDAR-derived DEMs, it is possible to collect high-resolution topographic data for Prairie depressions (Lindsay and Creed, 2004; Töyrä et al., 2005). In the literature, some studies have been reported for extracting water areas from LiDAR data. For instance, Hofle et al. (2009) used geometrical and intensity information of the airborne LiDAR data for extracting water surfaces by a seeded region-growing segmentation algorithm. In Hofle et al.'s study, a LiDAR-derived DEM was chosen as one of the data sources to apply in TOPAZ to delineate the maximum extent of depressions due to masking out surface water areas in thresholding image.

Landscape analysis tools, such as TOpographic ParamteriZation (TOPAZ), use a DEM as input to identify potholes and their contributing areas and to provide channel network information (Martz and Garbrecht, 1992). The core concept in TOPAZ is the subtraction of the "original DEM" from the "filled" DEM. The output of this process can map the extent of the maximum surface depression. However, the results depend on DEM resolution and quality. The foundation of TOPAZ and many landscape analysis tools is the D8 method for routing flow (Fairfield and Leymarie, 1991). This method evaluates each DEM raster cell by examining the elevation value of itself and the eight surrounding cells. Flow is assigned to the lowest neighbor cell (the steepest slope descent). The drainage pattern is then used to determine the upstream drainage area for that cell. For landscape analysis models to determine the gross drainage area and to delineate the drainage network, the input DEM must be free of cells that have no neighbors at a lower elevation

(Wang and Liu, 2006). A sink, or DEM cell that has no neighbors with a lower elevation, presents a problem for all of the algorithms. The literature presents several different approaches to removing sinks in the DEM (Martz and Garbrecht, 1998); each of these methods treat the sinks as spurious, however, and pre-process the DEM to remove sinks. In landscapes, such as the PPR depressions or sinks occur naturally and are the dominant features of the Prairie landscape.

1.8 Summary

RADAR can image landscape conditions day or night, through cloud cover, and in near-real time (Campbell, 2011). The microwave interactions with the surface water have been explained to illustrate how RADAR images are interpreted. RADAR has long been recognized for its ability to identify open surface water, owing to the specular nature of the surface water and subsequent minimal backscatter. This ability has led to the operational use of RADAR data for surface water and flood-mapping applications (Sokol et al., 2004; Brisco et al., 2009). Also, in RADAR processing, particular attention has to be paid to geometric corrections and speckle reduction for improving interpretation. The RADARSAT-2 thresholding method is regarded as the best compromise between information reliability and low computation time. However, the existence of many techniques implies that there is no particular best approach for mapping and monitoring surface water features. This study assumed that the integrated approach using various data sources could overcome the limitations in each single data source and produce more accurate maps (Gala and Melesse, 2012). Further work is required to integrate data in the form of geographical information system (GIS) layers. Such integration would improve the automatic classification of RADAR images. A benefit of automatic classification is that it reduces dependency on skilled technician support, especially in operational processing where remote sensing images are regularly used to support managers and decision-makers. Despite a significant

improvement of these automatic classification systems shown in the literature, techniques are needed that quickly, effectively and operationally extract surface water.

1.9 Research Hypothesis

To improve the previous operational procedures for surface water monitoring information, Bolanos et al. (2016) used a RADARSAT-2 thresholding-based procedure, complemented with a texture-based indicator to map surface water areas. Results show that some polygons selected as water areas from the RADARSAT-2 images were not detected as open surface water bodies in the optical images due to RADARSAT-2's high sensitivity to soil moisture content (Bolanos et al., 2016). The results also show that the authors' algorithm fails to map open water bodies smaller than 1 ha when applied to the RADARSAT-2 Wide Fine mode. Bolanos et al. (2016) evaluated the accuracy of the RADARSAT-2 (F0W3) in classifying surface water in various study areas with a high number of potholes less than 1ha. To determine the accuracy of the method, the authors used randomly stratified points from RS-2 (F0W3) and optical image pairs to compute the traditional method of error matrices. However, the accuracy assessment based on a confusion matrix and random points did not adequately evaluate the success of surface water mapping for different beam modes (i.e., the overall accuracy of F0W3 = 56%). Thus, for numerical weather prediction, an accurate indication that can measure an entire area of surface water is required to enhance the classification of surface water across the PPR.

It is hypothesized in this study that confining RADARSAT-2 thresholding water features maps to areas of physically-possible water ponding or surface depressions can increase the accuracy and reliability of mapping surface water. Due to the noticeable number of small surface water bodies in study areas, it is also hypothesized that the overall accuracy of threshold

classification can be improved by masking out the area of extended surface water using high-resolution topographic data such as Lidar-based DEM.

Chapter 2

Materials and methods

2.1. General Research strategy

The research was conducted over two study basins representing different types of landscapes: the St. Denis and Smith Creek basins in the Prairie Pothole Region (PPR). In general, the analysis of each basin was conducted in the following five stages:

1) RADARSAT-2 single Polarization (HH) data were used to map surface water, employing a simple threshold method;
2) RADARSAT-2 thresholding results were compared to high-resolution cloud-free SPOT images acquired concurrently with RADARSAT-2 images;
3) A map of surface depressions was generated using TOPAZ and a LiDAR-based DEM;
4) RADARSAT-2 thresholding results were masked with the TOPAZ depression map to remove spurious water areas that lie outside topographic depressions; and
5) The TOPAZ masking results were compared with high-resolution SPOT data to assess the effectiveness of the masking approach.

2.2 Study sites

This research was conducted in two study areas in the Canadian PPR. The first study area was the Smith Creek research basin (101 50'39.34W, 51 01'08.24N) located within the Assiniboine River basin about 60 km southeast of Yorkton, SK (Figure 2.1). The basin's land use is dominated by agriculture and pasture cropland (cereals and canola), occupying ~ 48% of the watershed. This basin covers approximately 445km2 and is characterized by Prairie pothole topography, with numerous isolated depressions and little or no surface inflow/outflow. The topography is relatively flat with slopes of 2-5 % and elevations of 490 – 548 m above sea level. Most ponds (potholes) in the basin can be classified as isolated basin marshes (Pomeroy et al., 2010). A large portion of the drainage basin is without an apparent natural outlet and does not contribute runoff to streamflow. The potholes in the basin are mostly shallow topographic depressions that have dramatic water level fluctuations. They have been extensively drained and lose water primarily to evapotranspiration (Minke et al., 2010; Dumanski et al., 2015). Over 10,000 ponds larger than 100m^2 have been identified in this basin (Fang et al., 2010). The annual average precipitation is ~450 mm, with 75% falling as rain. The mean winter temperature is -15ºC, and the mean summer temperature is 16ºC (http://www.climate.weatheroffice.ec.gc.ca/index.html).

The second study site is St. Denis National Wildlife Area, which covers about 361 hectares and is located approximately 40km east of Saskatoon (106° 5′ 36″ W, 52° 12′ 34″ N) (Figure 2.2). This basin has rolling hummocky terrain and knob and kettle topography, with slopes varying from 10 to 15%. The basin includes about 100 potholes and wetlands (Miller et al. 1985). The monthly mean temperature is -19 °C in January and 18 °C in July. The annual average precipitation is 350 mm, with 76% occurring as rain (Environment Canada, 2012). The area is underlaid with stratified silty glacio-lacustrine sediments that are further underlaid with the glacial till of the Battleford and

Floral formations (Hayashi et al., 1998). Hydrological interactions between the aquifer and the near surface are known to be negligible due to the slow vertical movement of water through the till aquitard (Van der Kamp and Hayashi, 2009). The land cover and landscape of the St. Denis basin differ from that of the Smith creek basin, with the former having less agricultural drainage and greater topographic relief (Figure 2.2). The elevation of the St. Denis basin varies between 546m to 565m above sea level. The effective area contributing to the outlet has been shown to be dynamic and dependent on antecedent wetness (Brannen et al., 2015), with the majority of potholes located in small depressions, with a few very large, deep depressions.

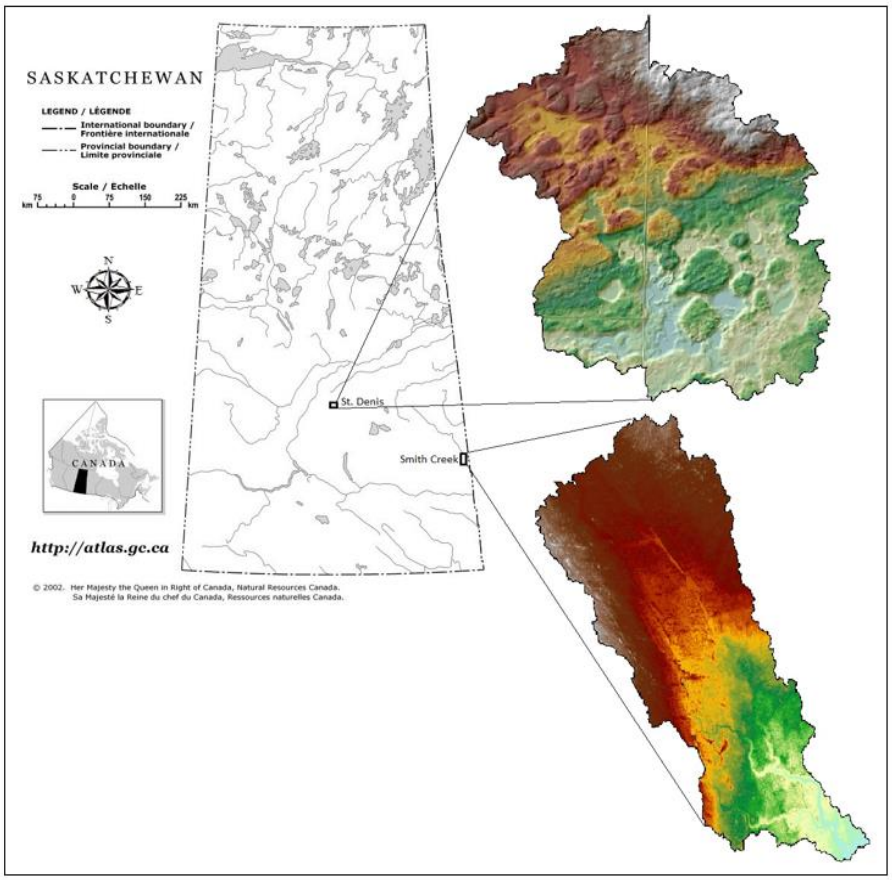

Figure 2.1. The image is depicting the locations of the St. Denis and Smith Creek research basins in the Canadian Prairie Region (http://atlas.gc.ca, NRC 2002).

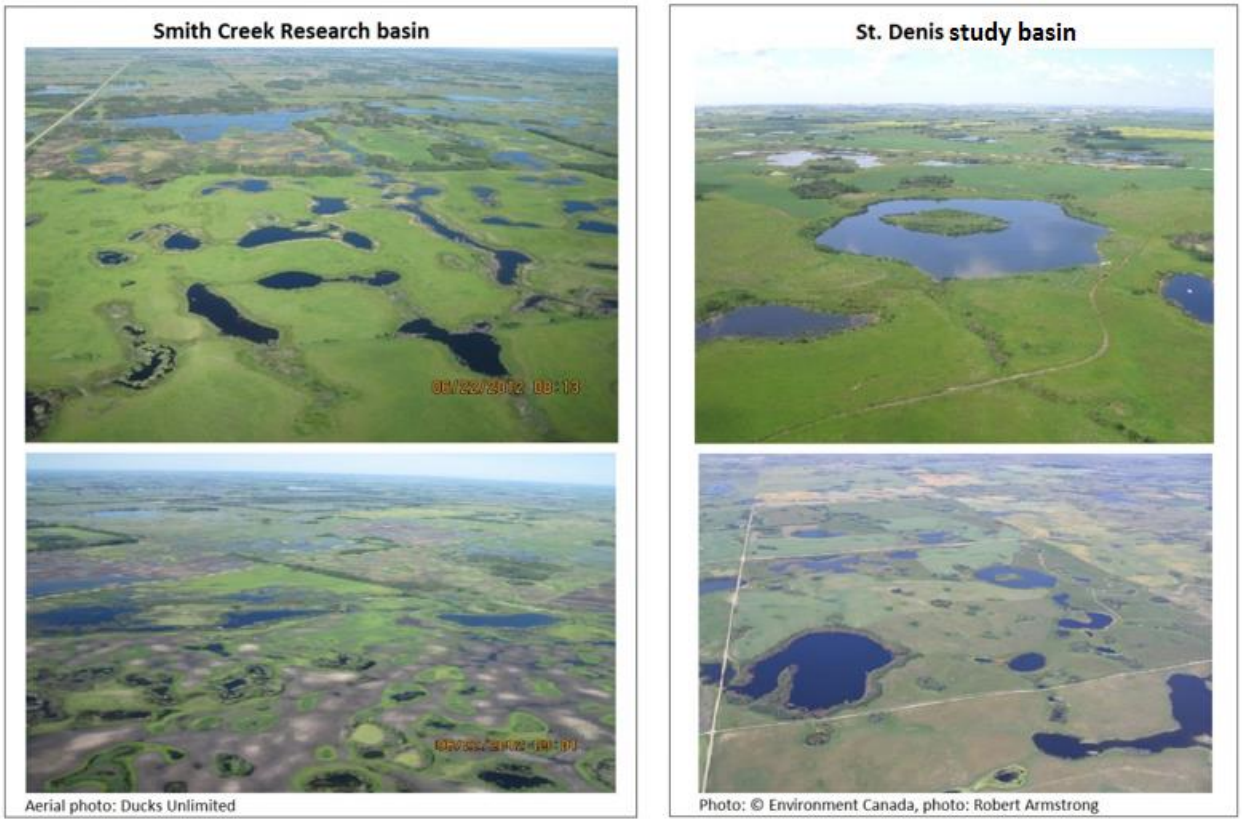

Figure 2.2. Aerial photos of Smith Creek research basin provided by Ducks Unlimited (left) and Aerial photos of St. Denis National Wildlife Area produced by Robert Armstrong, Environment Canada (right).

2.3 RADARSAT-2 data selection

Three different RADARSAT-2 single-beam modes data with large spatial coverage (Fine Wide, Standard, and Wide) were compared to assess their ability to map surface water areas in the St. Denis and Smith Creek basins. Acquisitions were managed using the RADARSAT-2 Acquisition Planning Tool (APT) (Morena et al., 2004) available from MacDonald, Dettwiller, and Associates Ltd. (MDA Ltd.). The APT can be used to determine orbit parameters, such as ground track orientation, polarization, and beam modes. A summary of the RADARSAT-2 data descriptions used in this research is presented in Table 2.1.

Table 2.1. Specifications of RADARSAT-2 data used in this study (MDA, 2016)

RADARSAT-2 Acquisition date	Beam mode & number of looks	Incidence angle (degs)	Nominal range resolution (m)	Polariz-ation	Noise equivalent Sigma zero (dB)	Elipsoide (datum)	Swath size (Km)	Covered site
2014-June-25	(F0W3) 1/Right	38.7-45.3	8.3-7.3	HH-HV	-24±2	NAD-83	150	St. Denis SK, Canada
2008-Aug-19	(W2) 1/Right	30.6-39.5	26.9-21.5	HH-HV	-28±2	NAD-83	150	St. Denis SK, Canada
2008-Oct-07	(S3) 1/Right	30.4-37.0	27.0-22.7	HH-HV	-29±2.5	NAD-83	100	Smith-Creek, SK Canada

The RADARSAT-2 images were geometrically corrected and rectified to monitor the surface water over the study areas. The RADARSAT-2 images were first geocoded in a latitude/longitude coordinate system based on the North American Datum of 1983 (NAD83). RADARSAT-2 images were integrated into a Geographic Information System (GIS) and merged with other types of vector or raster data, such as LiDAR-based DEMs, optical images (SPOT), and road maps in the same geographic coordinate system and datum. The following sections describe more details about the RADARSAT-2 data used in this research.

2.3.1 RADARSAT-2 beam mode

The selection of the beam mode is particularly important when a trade-off has to be made between swath and acquisition mode. The RADARSAT-2 beam modes with large coverage are available in one of two HH-HV or VV-VH polarizations, while the smaller swath extents can provide all four polarizations at the same time. In this study, the major factors in the selection of

beam modes were the large spatial coverage and the availability of cloud-free SPOT images taken simultaneously to validate the surface water areas detected in RADARSAT-2.

2.3.1.1 Wide Fine beam mode (F0W3), St. Denis basin

The RADARSAT-2 Wide Fine (F0W3) beam mode HH polarization was acquired with a Nominal Image Coverage (NIC) of 150km x 150km in June 2014 for the St. Denis research basin. The Wide Fine beam mode with a nominal range resolution of 8.3m in the near range and 7.3m in the far range (incidence angel 38.7º – 45.3º) was designed for applications that require both a finer spatial resolution and a wide image coverage (150km) (MDA, 2016). This beam mode has a nominal ground swath equivalent to that offered by the Wide Swath beam mode and a spatial resolution equivalent to that offered by the Fine Resolution beam mode, at the expense of somewhat higher noise levels (MDA, 2016). Wide Fine Resolution beam mode products can be generated with a dual-co and cross-polarization (HH+HV or VV+VH), with a single linear co-polarization (HH or VV), or with a single linear cross-polarization (HV or VH). The Wide Fine beam mode was selected because of its fine resolution, large spatial coverage, and the availability of a simultaneous cloud-free high-resolution SPOT-6 image that could be used to validate the surface water mapping results.

2.3.1.2 Wide beam mode (W2), St. Denis basin

The RADARSAT-2 Wide beam mode (W2) HH polarization with a Nominal Image Coverage (NIC) of 150km x 150km was acquired in August 2008 over the St. Denis Research basin. The Wide beam mode provides imaging of a ground coverage of 150km x 150km, which is

similar to Wide Fine beam mode coverage (MDA, 2016). The Wide Swath beam mode with a nominal range resolution of 26.9m in the near range and 21.5m in the far range and with an incidence angel of 30.6º – 39.5º can be generated with a single linear cross-polarization (HV or VH), with a single linear co-polarization (HH or VV), or with dual co- and cross-polarizations (HH+HV or VV+VH). To examine the impact of resolution and beam mode, the Wide mode was selected and compared to surface water detection results from the Wide Fine beam mode over the St. Denis basin. The Wide Fine beam mode had an equivalent pixel spacing size and resolution to Standard beam mode and was used to examine the landscape effects over two study basins in PPR. However, the Wide beam mode was only available for the St. Denis research basin.

2.3.1.3 Standard beam mode (S3), Smith Creek basin

The RADARSAT-2 Standard beam mode (S3) HH polarization with a nominal image coverage of 100km x 100km was taken in October 2008 for the Smith Creek research basin. The Standard beam mode can provide a nominal range resolution of 27m in the near range and 22.7m in the far range with wide image coverage (nominal ground coverage of 100 km x 100 km) (Appendix B). Standard beam mode products can be generated with dual co- and cross-polarizations (HH+HV or VV+VH), with a single linear co-polarization (HH or VV), or with a single linear cross-polarization (HV or VH). As the Wide Fine beam mode was the only RADARSAT-2 data available for the St. Denis basin, the Standard beam mode with large image coverage was chosen to investigate the influence of the landscape and resolution on surface water detection for the Smith Creek basin.

2.3.2 RADARSAT-2 polarization selection

RADARSAT-2 provides data of different polarizations. Several studies have examined the effect of polarization on surface water mapping. Previous studies have shown that for mapping surface water HH is the preferred polarization, especially when weather conditions are unknown (Brisco et al., 2009). This is because HH polarization has lower backscatter than HV polarization over rough open water (wind-induced surface water roughness) (Martinis et al., 2009; Gan et al., 2012). In the present study, both HH and HV channels were visually observed to examine which polarization was more suitable for discriminating water in the study sites (Figure 2.3). The HH channel was noticeably more effective for separating open water from land. Thus, the RADARSAT-2 single-polarized (HH) channel was applied to detect surface water data. According to the operational purpose of the study, the Wide Fine, Standard, and Wide beam modes with HH polarization were used to monitor surface water in our study areas.

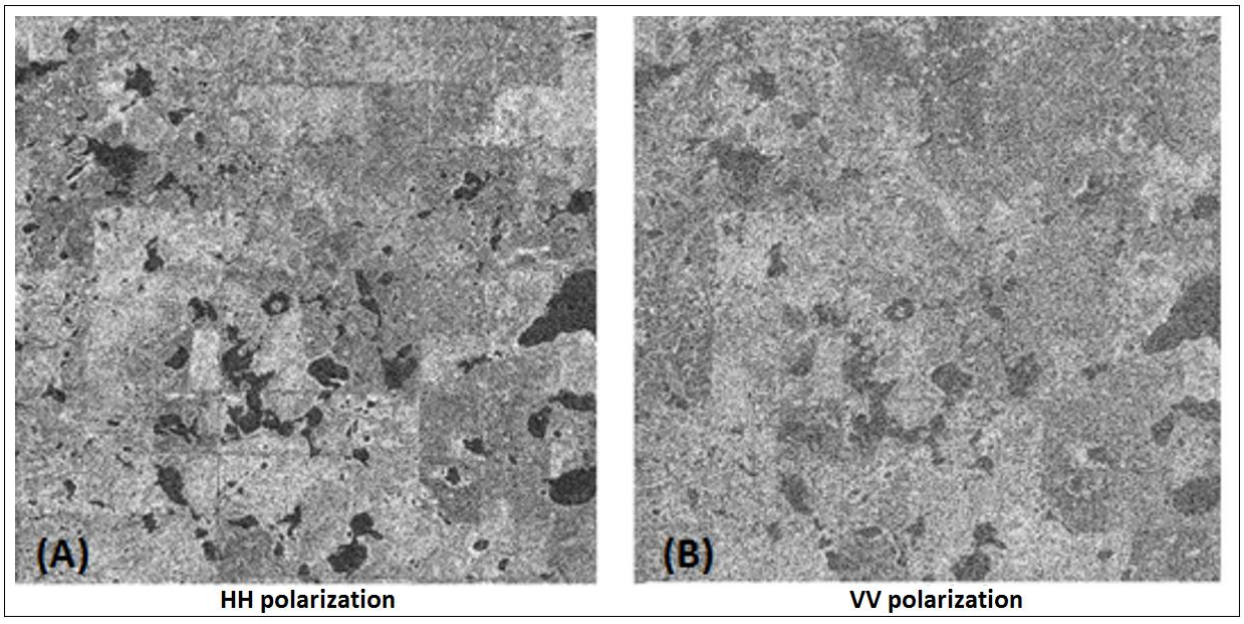

Figure 2.3. RADARSAT-2 Fine Wide (HH, HV) polarization; surface water areas appear as dark tones and land surface areas as bright tones. The HH polarization (A) provides better discrimination between surface water areas and land than HV polarization (B).

2.3.3 RADAR image calibration

To compensate for RADAR image distortion, most geoscience applications and imagery geometry use RADARSAT-2 data calibration. To extract a useful backscatter image from RADAR data, the digital values of a received signal should correspond to the physical qualities of the scene, such as location, brightness, and reflectivity.

2.3.4 RADARSAT-2 image processing software and radiometric enhancement

The goal of radiometric enhancement is to improve the interpretation of the radiometric information in an image using speckle filters. These filters can reduce speckle, detect edges, and visually enhance the image. PCI Geomatics is one of the most commonly used SAR processing and RADAR analysis software (PCI Geomatics Enterprise, Inc® 2016). Data acquired by RADAR sensors are available in diverse data formats, processing levels, resolutions, and beam modes. The PCI Geomatics software can support the RADARSAT-2 data structure and provide a variety of modules and algorithms associated with processing RADAR data. In this research, the first stage of RADARSAT-2 image processing was converting the complex data, known as Single Look Complex (SLC) data, to the next RADAR processing stage, known as detected data (decibel). RADARSAT-2 detected data are easier to interpret because information is provided on backscatter power for any given pixel in the image. Some RADAR processing algorithms also require detected data in the input, such as most RADARSAT-2 speckle filtering algorithms. To generate detected data from SLC data, digital numbers (pixel values) are first transformed to sigma0 (σ^0), which is the RADAR backscatter coefficient and used for any further analysis. The RADAR backscatter coefficient (σ^0) is expressed per unit area in ground range (Geomatica SAR training guide, 2016). Therefore, RADARSAT-2 images were converted from SLC to detected data (dB), which were

associated with the information of any given pixels as RADAR backscatter power; as a result, the pixels' values were changed to decibels to increase the contrast between land and water areas based on RADAR brightness (Geomatica SAR training guide, 2016).

$$\beta\ ^{0}j = (DN^{2}_{j} + A3)/A2_{j} \quad \text{(eq 2.1)}$$

RADAR brightness in decibel is shown by:

$$\text{Decibel (dB)} = 10*\log10\ (\beta 0j) \quad \text{(eq 2.2)}$$

Where β is the most natural and observable RADAR measurement (Raney et al. 1994), DN_j is the digital number that depicts the magnitude of the j^{th} pixel of the range in the detected image data, $A2_j$ is the scaling-gain value for the j^{th} pixel, and A3 is the fixed offset.

2.3.5 RADARSAT-2 Speckle noise reduction

High-frequency noise (speckle) is a dominant feature of RADAR imagery. To reduce speckle while preserving spatial edges (features), a radiometric filter is applied, which can improve the interpretation of the radiometric information in the image. The speckle noise gives a grainy (salt-and-pepper) appearance, which is RADAR scene inherent and should be reduced as much as possible by using speckle filtering. The ideal noise reduction filter reduces the speckle with only a very small loss of information. The FGAMMA filter with a medium window size (5*5) is widely used by the RADAR community to reduce speckle noise (Toutin, 2011; Zhang et al., 2012; Long et al., 2014; White et al., 2014). The FGAMMA filter is a Maximum A Posteriori (MAP) filter based on a Bayesian analysis of the image statistics. Both the RADAR reflectivity and the speckle noise are supposed to follow an FGAMMA distribution. This method reduces the reflectivity and

the noise to an exponential distribution of image pixels. The mean to standard deviation ratio (signal to noise ratio) describes the GAMMA distribution (Gagnon and Jouan, 1997):

$$\left(\frac{\text{mean}}{\text{standard deviation}}\right)^2 = L = constant \quad \text{(eq 2.3)}$$

In this research, the FGAMMA filter was applied to RADARSAT-2 detected (decibel) channels to reduce speckle noise and to maintain spatial details and edges, following the approach widely used in previous studies (Figure 2.4) (White et al. 2014). This approach was selected for speckle removal, as it was effective for all the available RADAR resolutions, incidence angles, and beam modes with relatively low processing time (Martinis et al., 2009; Long et al., 2014).

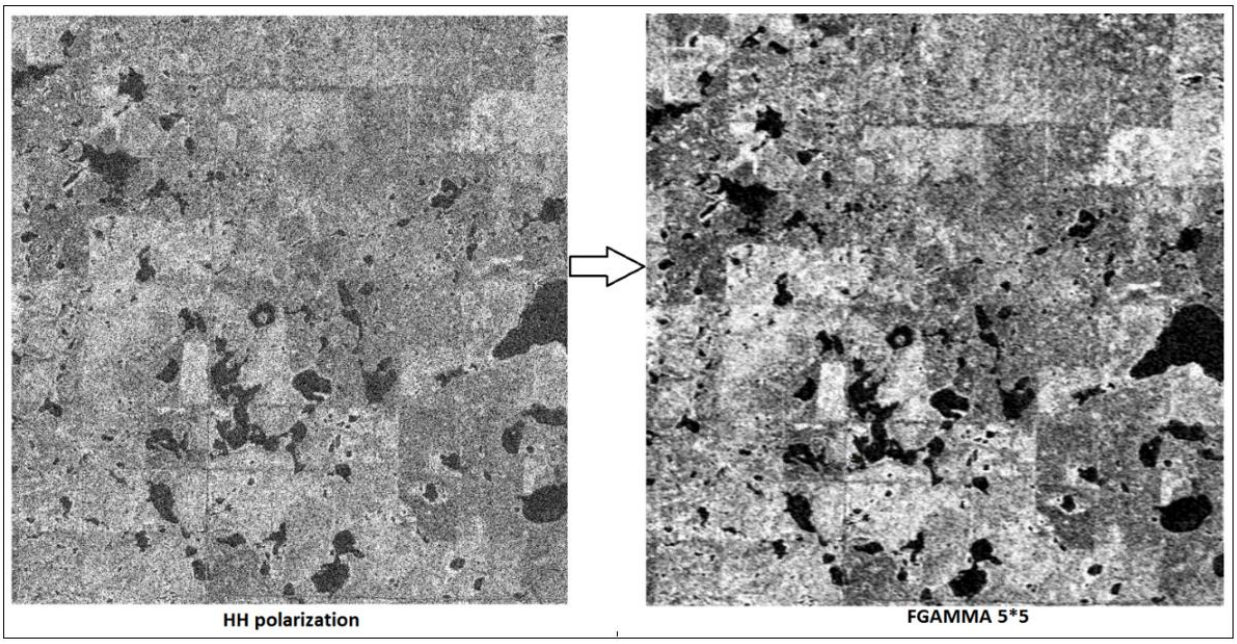

Figure 2.4. An original RADAR image (left) and the image after speckle removal and FGAMMA filtering (right).

2.3.6 RADARSAT-2 geometric enhancement

Natural RADAR images are side-looking imagery (SLI), and it is essential to convert the slant range geometry to ground range geometry to reduce distortion caused by the slant range view (Figure 2.5). The location of each pixel and its resolution is a combination of the time between two signals relative to the sensor speed (Y, azimuth) and the time a signal takes to be reflected back to the sensor (X, range resolution) (MDA, 2016). Typically, it takes more time for a transmitted signal to arrive at the far range of the RADAR swath (the area scanned by the RADAR antenna beam) than the near range. Thus, the slant range resolutions at the far range and near range are different (Lee and Pottier, 2009). Therefore, the natural result of the RADAR-range measurement is slant-range geometry, which needs to be transformed (converted) to ground range geometry specified by square pixels.

The range geometry of the RADAR image was corrected using the "Ortho-Engine" module of PCI-Geomatics. This tool uses projection information such as UTM zones, datum (NAD-83), and mathematical information to geometrically correct the RADARSAT-2 data. The georeferenced images were generated using high-resolution DEM data (discussed in section 2.6) and geo-rectified to ground range geometry. To qualitatively verify the geo-rectification accuracy of RADARSAT-2 images, the national road network layer (provided by the Government of Canada, 2015) was used and visually compared to road intersections in RADARSAT-2 images. It was shown that the national road network properly corresponded to the road network on RADARSAT-2 images (Figure 2.6).

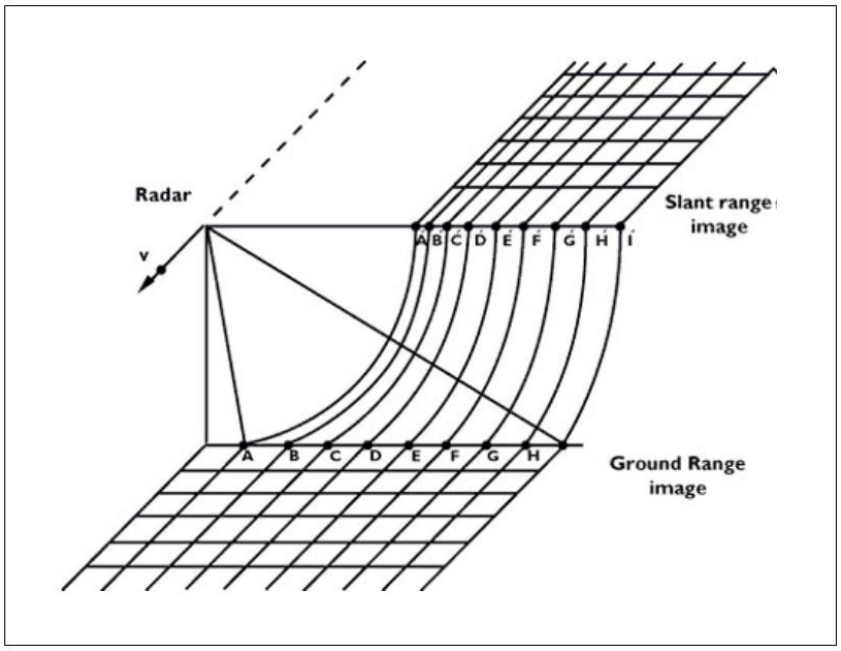

Figure 2.5. Slant range image versus ground range image (www.esa.int).

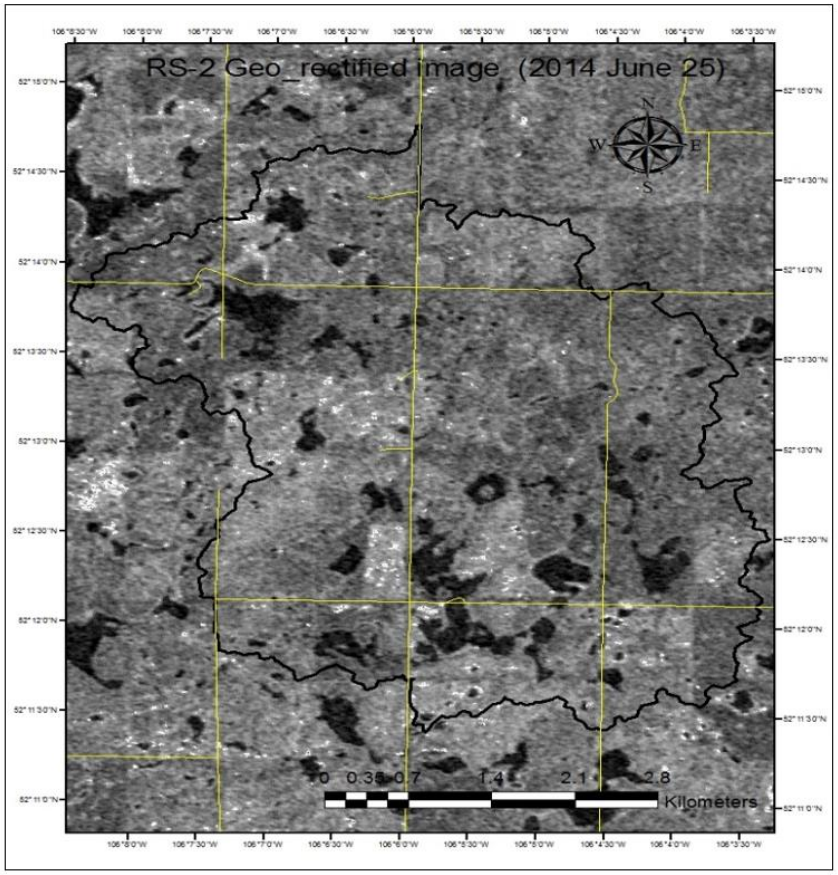

Figure 2.6. Overlaying of Canada National Road Network data layer on geo-rectified RADARSAT-2 data layer.

2.3.7 Land-water boundary contrast enhancement (histogram equalization)

To quantize the brightness values of a RADAR image, the value of each pixel in the image should be calculated. An image has a unique histogram of brightness (reflectivity) information. The tonal contrast (quality) of an image can be assessed from its histogram. A RADARSAT-2 image with poor contrast can be modified to achieve an image with a histogram that has the widest spread of brightness range. Contrast stretching of the image data was used to enhance the radiometric quality of RADARSAT-2 images. For instance, the original histogram for RADARSAT-2 Fine Wide beam mode has brightness values between -35 and 3, and the histogram equalization method expands this range to the maximum possible, from -66 to 25 (Figure 2.7). Histogram equalization was performed in the Arc-GIS environment to enhance water and land boundaries and to increase contrast in the RADAR image. The land-water boundary was enhanced with very little loss of spatial features (Figure 2.8).

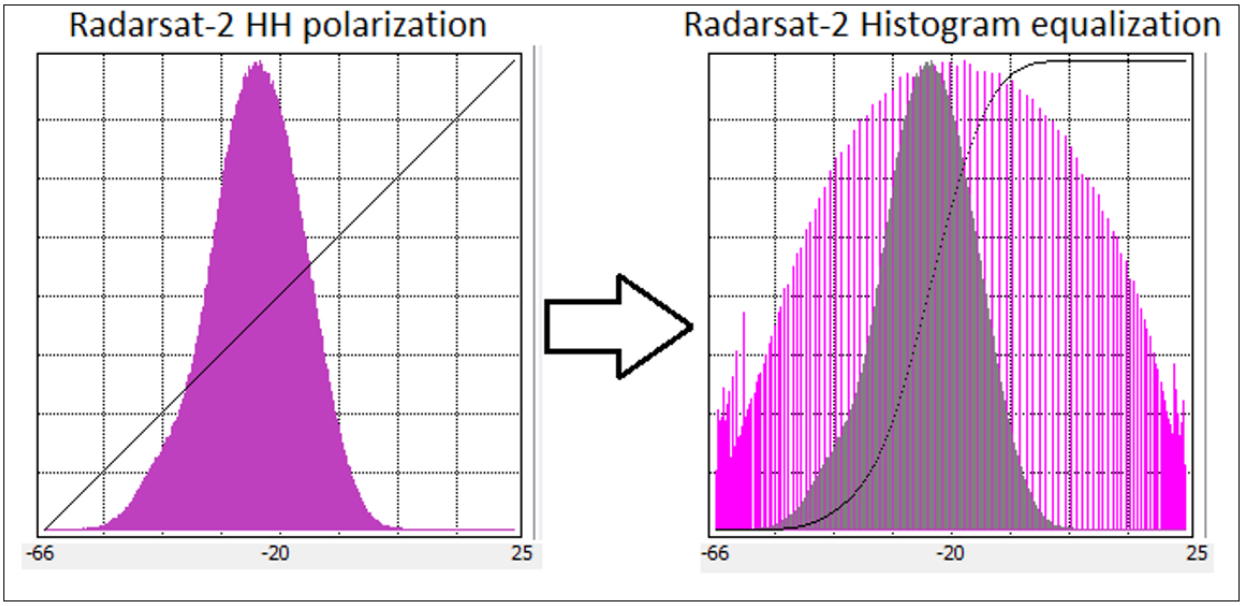

Figure 2.7. A RADARSAT-2 HH backscatter histogram (left) and contrast stretching using RADARSAT-2 histogram equalization (right).

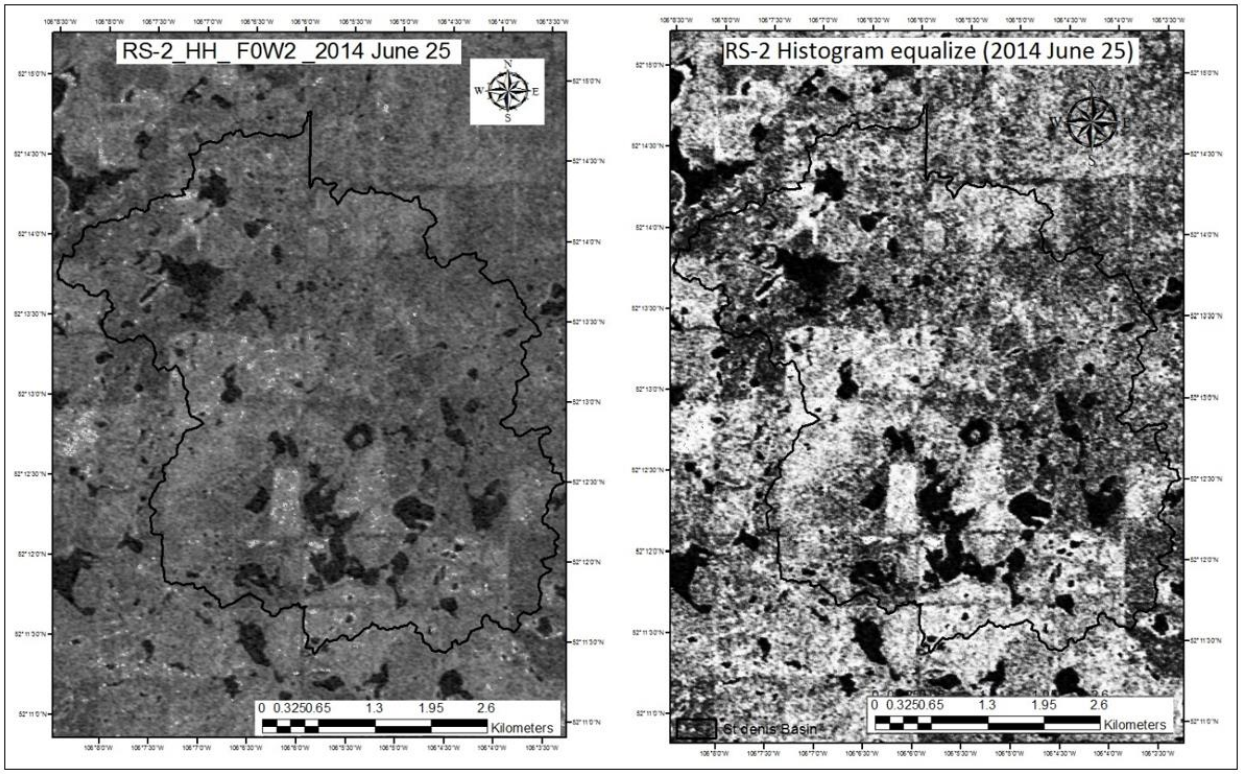

Figure 2.8. An RS-2 (F0W3) image of St. Denis basin before histogram stretching (left) and after histogram equalization (right).

2.4. RADARSAT-2 thresholding approach

The RADAR thresholding approach is one of the most frequently used methods to distinguish water bodies from land in RADAR imagery (Brisco et al., 2009; Martinis et al., 2009; White et al., 2014). The primary purpose of the thresholding classification method is to produce RADAR backscatter signal groupings based on certain similarities. To define the thresholding values of RADARSAT-2 images, one of the most common image classification approaches (iso-clustering) was first used to cluster pixels based on homogeneity, brightness, and backscatter values to obtain an initial map of water and land classes (Richard and Jia, 2006; Li and Wang, 2015). An initial waterbody classification was created by applying iso-clustering to the HH polarization RADARSAT-2 images. The lowest backscatter class value of the iso-cluster images

was specified and classified as the thresholding value, and any value lower than the threshold value was assigned to be surface water (Lee and Pottier, 2009). The lowest backscatter value was then applied as the range of surface water threshold values in the RADARSAT-2 image (Figure 2.9). The threshold values to extract surface water information were modified based on the beam modes of each individual scene. The threshold values for RADARSAT-2 Fine Wide, Standard, and Wide beam mode images were defined as -16.9, -18, and -16, respectively, and then all elements of the RADAR data with a backscatter value lower than those given threshold values were assigned to the water class (Figure 2.10). The RADARSAT-2 images were reclassified as surface water and non-water classes for all three data sets (Wide Fine, Standard, and Wide) as shown in Figures 2.10, 2.11, and 2.12.

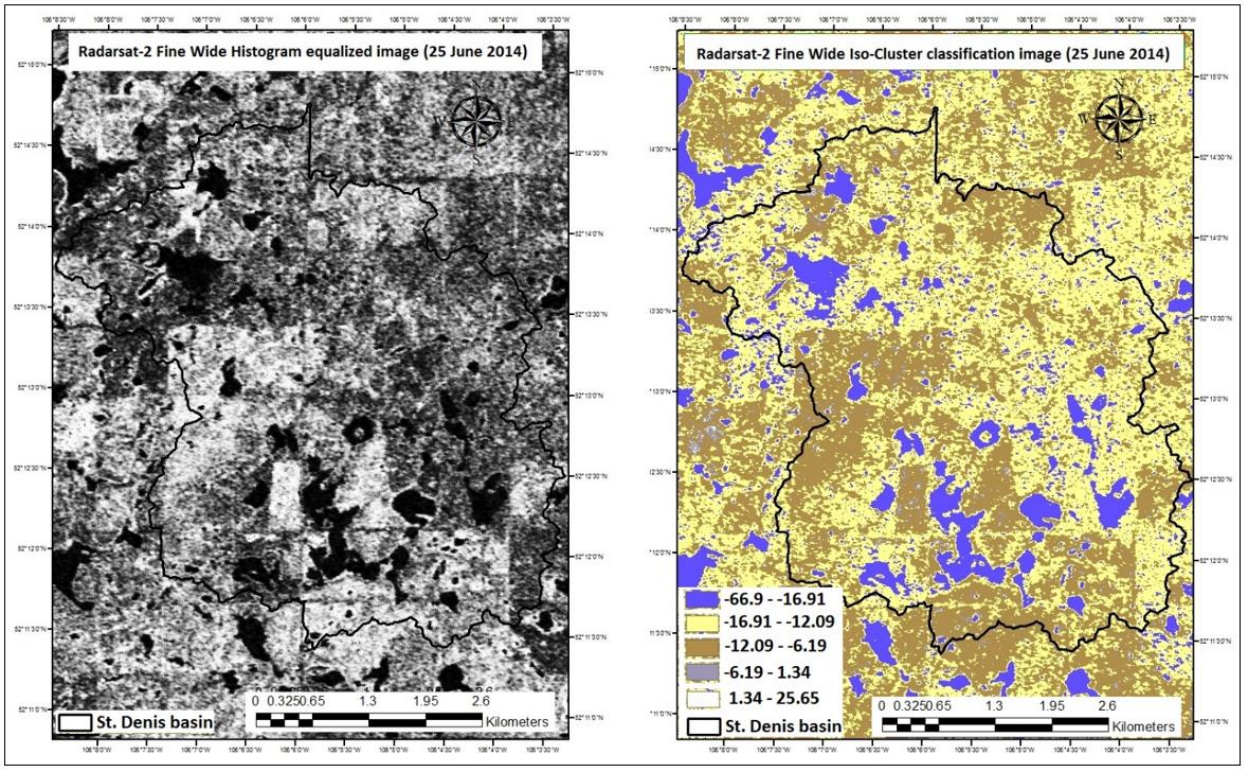

Figure 2.9. The left image shows the iso-cluster unsupervised classification results for the RADARSAT-2 image of St. Denis basin. In the iso-cluster classification image (right), the thresholding range for Fine Wide mode was ~ -17.

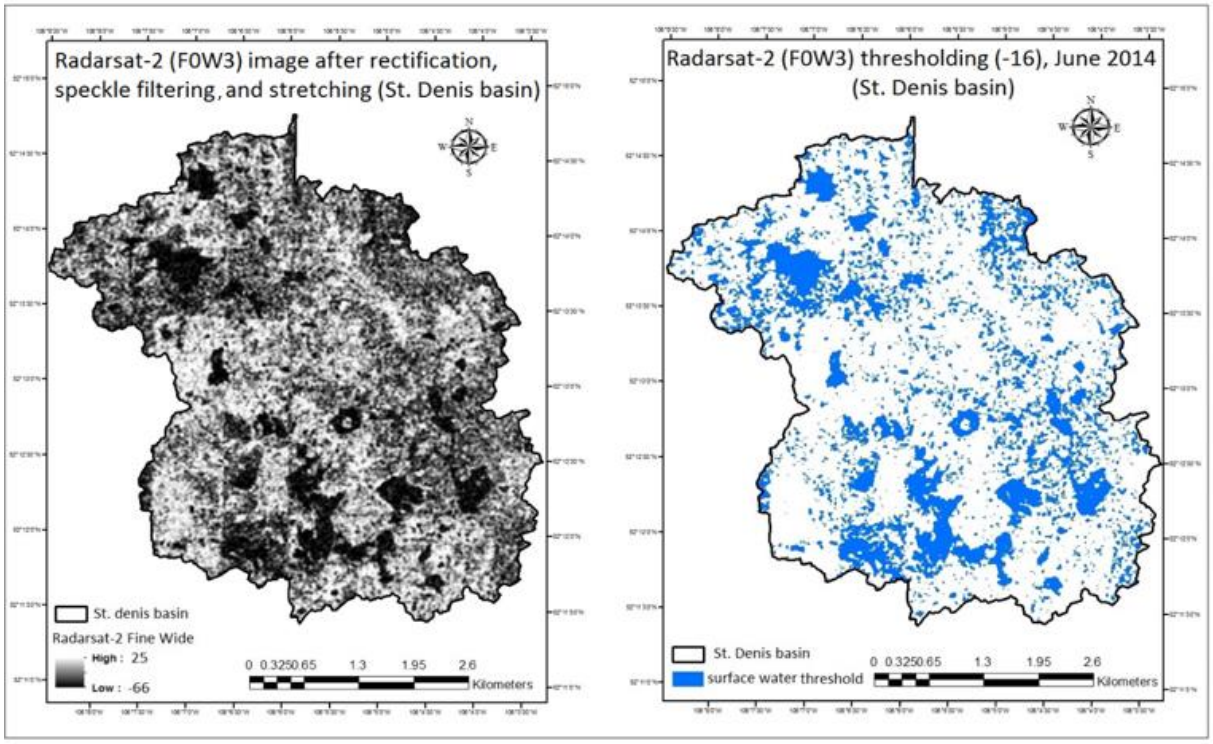

Figure 2.10. A RADARSAT-2 Wide Fine mode image after geo-rectification, speckle filtering, and histogram equalization (left); surface water area classification using the RADARSAT-2 (F0W3) thresholding approach over the St. Denis basin, June 2014 (right).

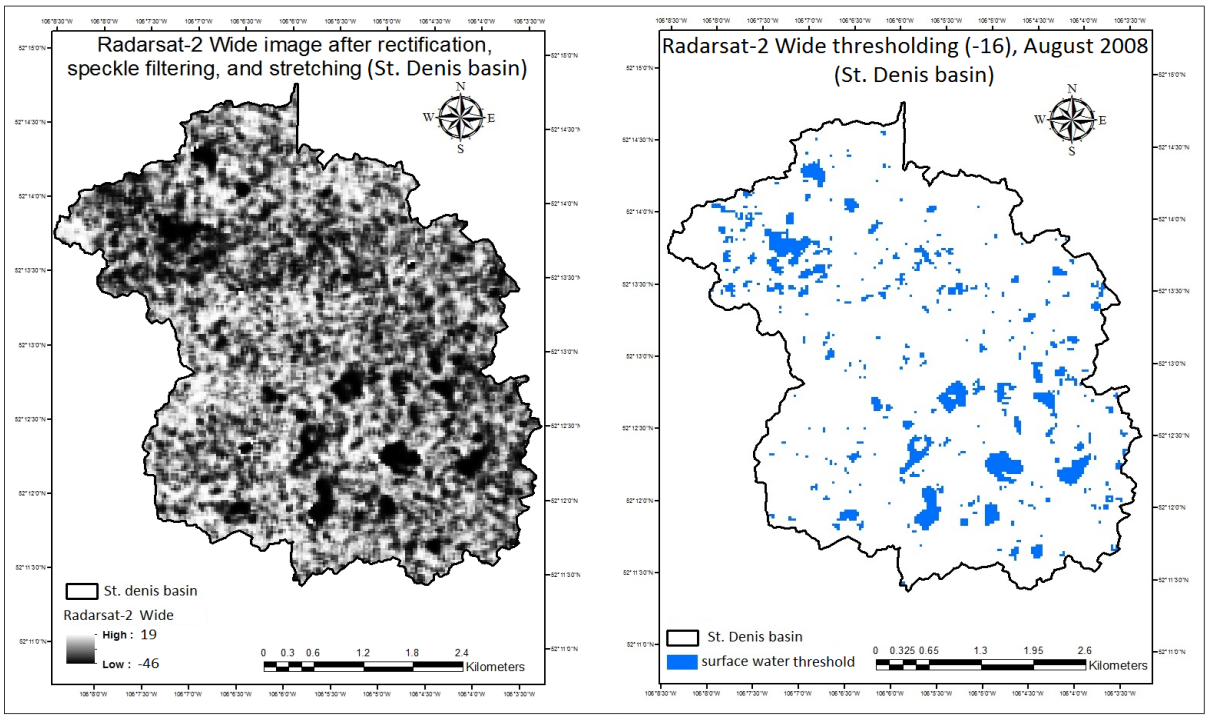

Figure 2.11. A RADARSAT-2 Wide beam mode image after geo-rectification, speckle filtering, and histogram equalization (left); surface water area classification using a RADARSAT-2 thresholding technique, St. Denis basin, August 2008 (right).

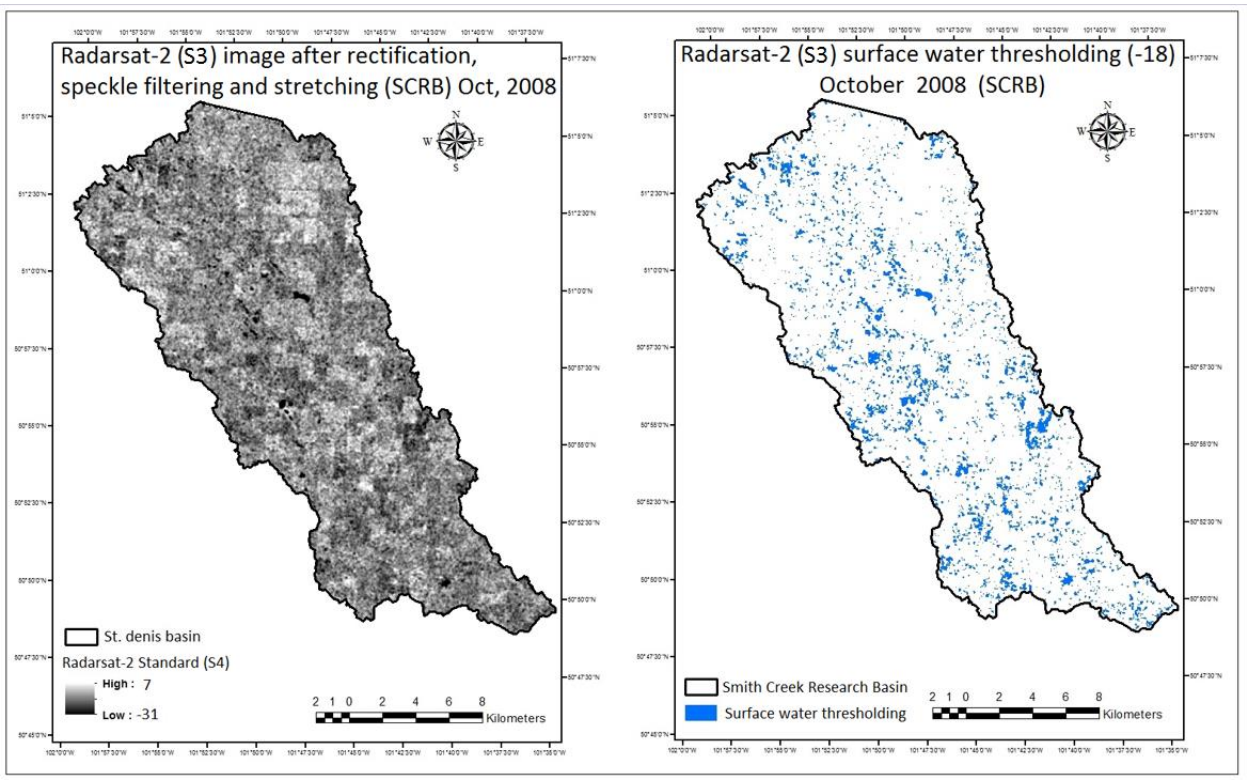

Figure 2.12. A RADARSAT-2 Standard beam mode image after geo-rectification, speckle filtering, and histogram equalization (left); surface water area classification using the RADARSAT-2 thresholding technique, Smith Creek basin, October 2008 (right).

2.5 Le Systeme pour I'Observation de la Terre (SPOT) data

The surface water detection capability of SPOT data is mostly due to the absorption of Electromagnetic (EM) energy by water in the near and mid-infrared portion of the spectrum. Because accessing high resolution cloud-free optical data is difficult, RADARSAT-2 images were selected following the availability of SPOT images over study basins. The high-resolution cloud-free SPOT images were obtained nearly simultaneously with RADARSAT-2 images. SPOT images were resampled to match the pixel spacing of the RADARSAT-2 images. A geometric correction was applied in processing SPOT data because further analysis requires the data to be compared and overlaid onto RADARSAT-2 data. The literature shows that the optical SPOT with

10m resolution multispectral satellite imagery is a very reliable measure for land cover classification, including ponded water areas over PPR (Shook et al., 2013). Because high SPOT multispectral imagery has high classification accuracy, it was used as ground truth data to evaluate the capability of the RADARSAT-2 beam mode to detect surface water in the St. Denis and Smith Creek basins.

As the precise location information from the SPOT data was required, the SPOT images were georeferenced and projected into the Universal Transverse Mercator (UTM) coordinate system through image processing software (Arc GIS 10.3). Images were geo-rectified to a projected 1m resolution LiDAR-based DEM data. SPOT images were georeferenced by creating a mathematical relationship between select features on an image and the same features on a LiDAR-based DEM image. The mathematical relationship was then applied to all remaining pixels, which warped the SPOT images to a UTM projection. The procedure requires the use of distinct objects that exist in both the SPOT images and LiDAR-based DEM data. These objects are commonly referred to as ground control points (GCPs). GCPs were well-distinguished features such as road intersections across the images. A minimum number of eight GCPs was required to calculate the transformation. The “Root Mean Square Error” (RMSE) lower/equal to 1.0 was generated by the image processing software (ArcMap 10.3), as the level of positional accuracy of the mathematical transformation for each SPOT image was individual. Once the images had been geometrically corrected, a land and water classification was generated for each of these SPOT images using a modified normalized difference water index (Xu, 2006) and band-ratio classification approach (Doxaran et al., 2002; Alifu et al., 2015).

In a band-classification approach, one spectral band is proportioned with another spectral band. This method highlights a particular image element, such as surface water area. When choosing bands to highlight a particular aspect of a scene, it is best to consider bands that are poorly correlated. In the current study, a ratio of "blue" or "green" bands (depending on the availability of bands in each sensor) and a band Near-Infrared (NIR) from SPOT image data were used to extract surface water bodies. Three pairs of coincident SPOT and RADARSAT-2 datasets were selected for delineating and measuring surface water areas over St. Denis and Smith Creek basins. Table 2.2 gives a summary of SPOT sensor data used in this research.

1. Over St. Denis research basin, a cloud-free SPOT-6 (6m resolution) image was available on 25 June 2014, just one day after RADARSAT-2 F0W3 mode acquisition on 24 June 2014 (Figure 2.13).

2. Over St. Denis research basin, a cloud-free SPOT-4 (20m resolution) image was available on 19 Aug 2008 concurrent with RADARSAT-2 W2 mode (19 Aug 2008) to validate RADARSAT-2 data.

3. Over Smith Creek research basin, a cloud-free SPOT-5 (10 m resolution) image was available on 1 Oct 2008, six days before the RADARSAT-2 S3 mode (7 Oct 2008) acquisition date (Figure 2.14).

Table 2.2. Summary of SPOT 4, 5, and 6 sensor characteristics (www.intelligence-airbusds.com).

Sensor (Acquisition date)	Spectral Bands Range (nm)	Spatial resolution (m)	Classification method	Study Area
SPOT 6 (2014 June 25)	Pan (panchromatic) B1 (Blue) B2 (Green) B3 (Red) B4 (Near-Infrared)	Panchromatic (2.5 m) Multispectral (6 m)	Band ratio (B1/B4) & MNDWI	St. Denis, SK
SPOT 4 (2008 August 19)	P (panchromatic) B1 (Green); B2(Red) B3 (near-infrared) B4 (SWIR: Short-wave infrared)	Panchromatic (10 m) Multispectral & NIR (20 m)	Band ratio (B1/B3) & MNDWI	St. Denis, SK
SPOT 5 (2008 October 1)	P (panchromatic) B1 (Green); B2(Red) B3 (near-infrared) B4 (SWIR: Short-wave infrared)	panchromatic (5 m) Multispectral & NIR (10 m) SWIR (20 m)	Band ratio (B1/B3) & MNDWI	Smith Creek, SK

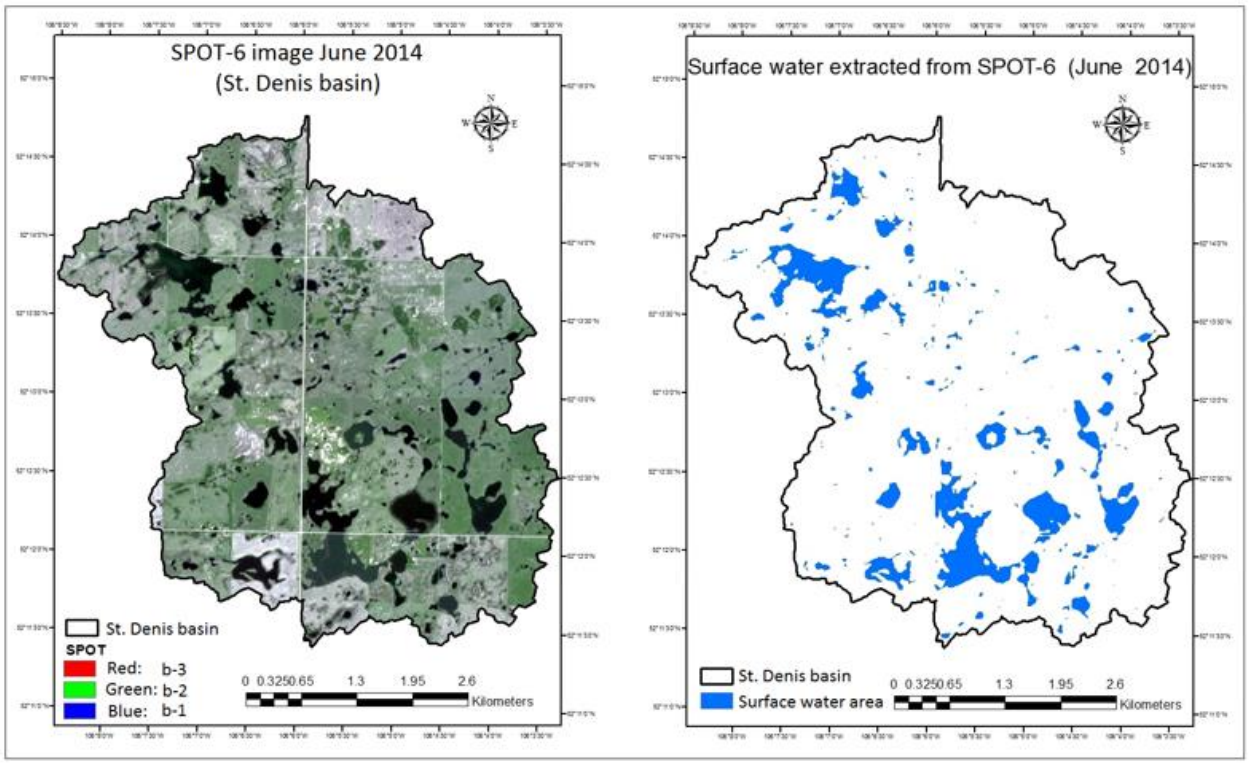

Figure 2.13. High resolution optical multi-spectral image used as reference data (left) for St. Denis basin. The surface water areas extracted from SPOT-6 image and showed in blue color (right) to validate the RADARSAT-2 (F0W3) surface water thresholding and TOPAZ-masked images.

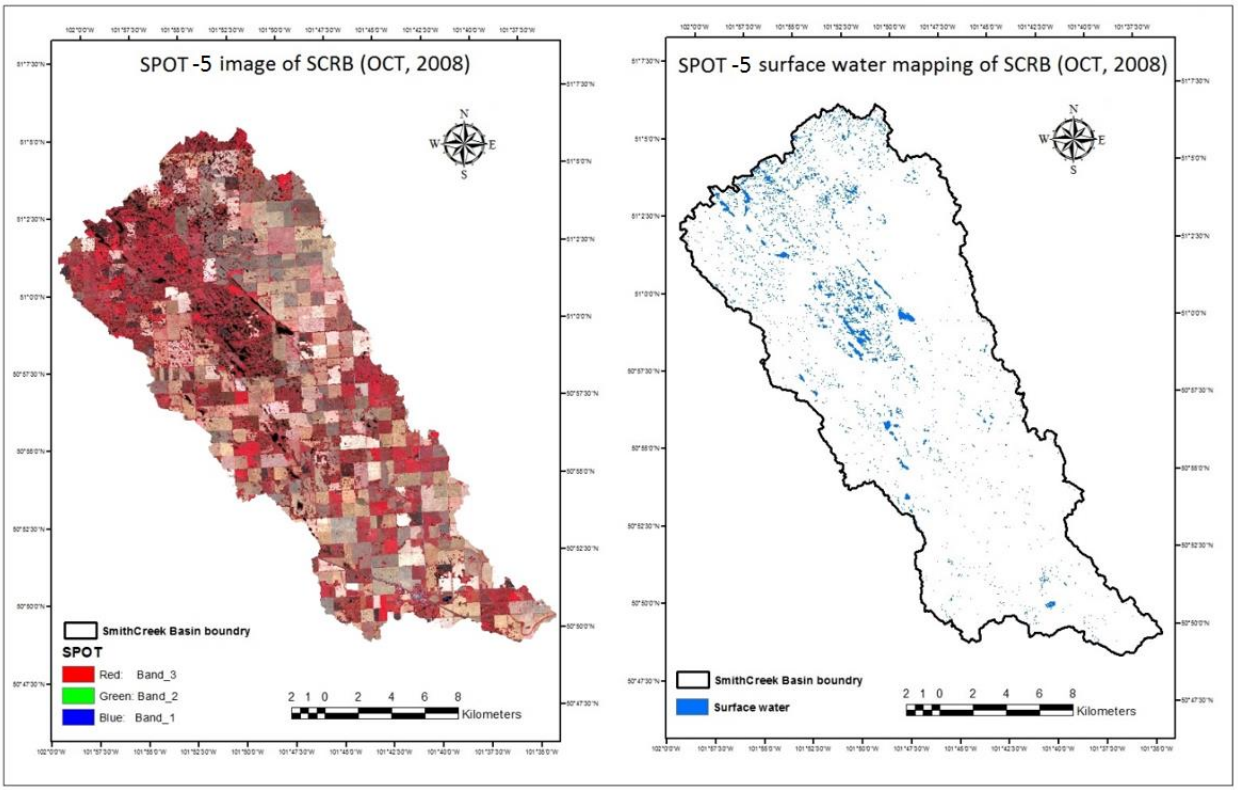

Figure 2.14. High-resolution optical multi-spectral image used as reference data (left) for Smith Creek research basin. The surface water areas extracted from SPOT image and depicted in blue color (right) to validate the RADARSAT-2 (S3) surface water thresholding and TOPAZ-masked images.

2.6 Analysis of TOPAZ (Topographic-PArameteriZation) using LiDAR-based DEM Data

High spatial resolution of LiDAR-based DEM was used to extract the topographic features in the study areas. High-resolution LiDAR-based DEM data was acquired over St. Denis National Wildlife Area by the Canadian Consortium for the LiDAR Environment Applications Research/Applied Geomatics Research Group (AGRG) of the Nova Scotia Community College and the C-CLEAR program through a flight made in August 2005 (Table 2.3). This month was selected to deliver the highest quality DEM, as it is the driest period of the year when most inundated ponds are dry or have the lowest annual water level. Data processing to convert LiDAR data into a DEM (1m) was conducted by NWRI, Environment Canada (Töyrä, 2005). The

generated DEM was provided in Universal Transverse Mercator (UTM), Zone 13, coordinate system with the North American 1983 NAD83 (CSRS) projection datum. Also, LiDAR data was collected over Smith Creek research basin by LiDAR Services International (LSI) for the Manitoba Water Stewardship and Saskatchewan Water Authority in October 2008. The derived 1m resolution DEM for Smith Creek basin was provided in the UTM Zone 14 coordinate system with a horizontal projection datum of NAD83 in meters (Table 2.3).

TOPAZ (Topographic-PArameteriZation) is an analytical software package similar to others like ArcGIS and is widely used to automatically identify topographic characteristics and to extract basin features (Martz and Garbrecht, 1992). TOPAZ was designed initially for assisting topographical evaluation and watershed parametrization for hydrological modeling and analysis (Garbrecht and Martz, 2000). TOPAZ uses a DEM to identify topographic features, drainage networks, and watershed parameters. Depressions are common features in DEMs and can cause problems for downslope flow routing. TOPAZ assumes these features are spurious and modifies them by digitally filling all depressions to the local spill elevation (Garbrecht and Martz, 1997). A LiDAR-based digital elevation model (DEM) of each study basin was used as input to TOPAZ to generate a filled-depression DEM. The original DEM was subtracted from the filled-depression DEM to delineate the maximum extent of depression areas. TOPAZ provided the depression map in GIS format (Figures 2.15 and Figure 2.16). Detailed descriptions of the TOPAZ model and the output files are available in Garbrecht and Martz (1999).

Table 2.3. An overview of LiDAR-based DEM data, including acquisition date and coordinate systems used in study areas.

DEM data	Acquisition date	Study area	Coordinate system	Generated and provided by
LiDAR-based DEM	August 2005	St. Denis, SK	NAD-83 (UTM13)	Canadian Consortium for LiDAR Environment Applications Research/Applied Geomatics Research Group of Nova Scotia Community College (C-CLEAR/AGRG)
LiDAR-based DEM	October 2008	Smith Creek, SK	NAD-83 (UTM14)	LiDAR Services International (LSI), a Calgary-based LiDAR mapping company

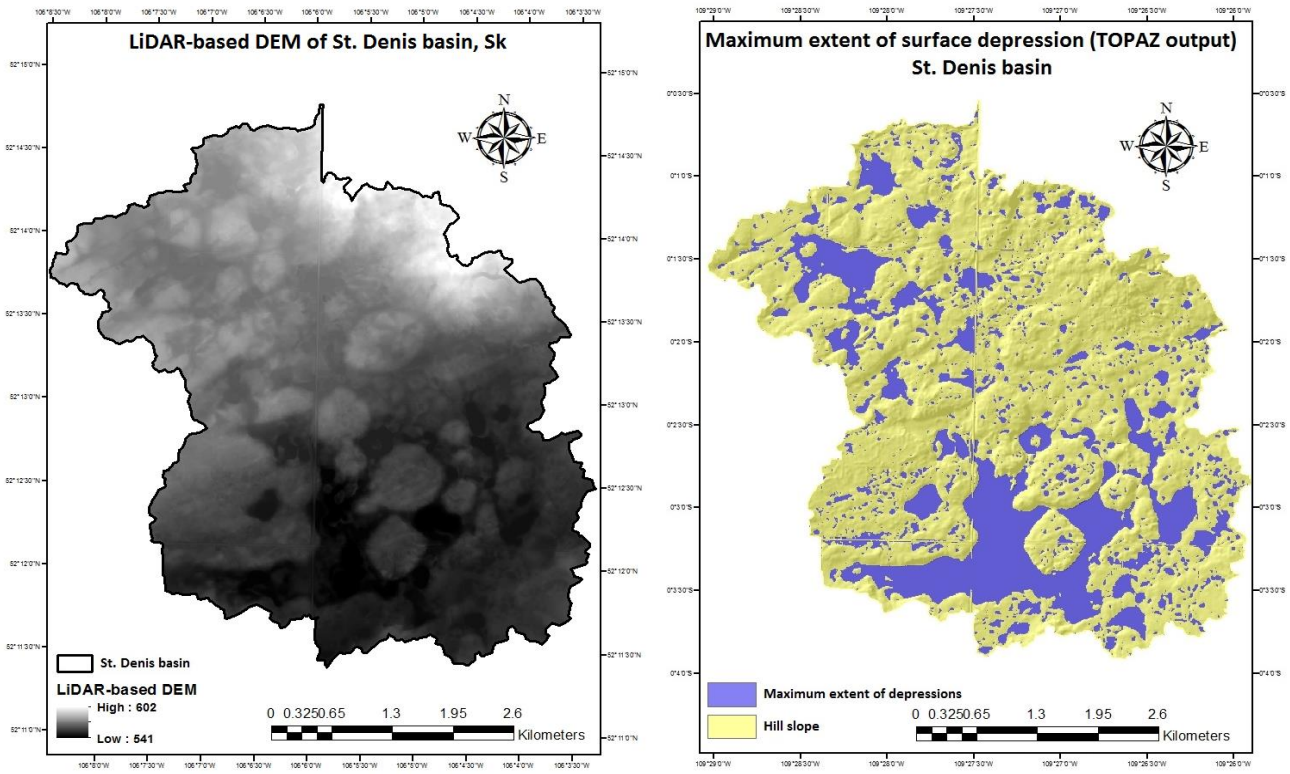

Figure 2.15. Lidar-based DEM of St. Denis National Wildlife Area (left), and the maximum extent of surface depressions extracted from TOPAZ (right).

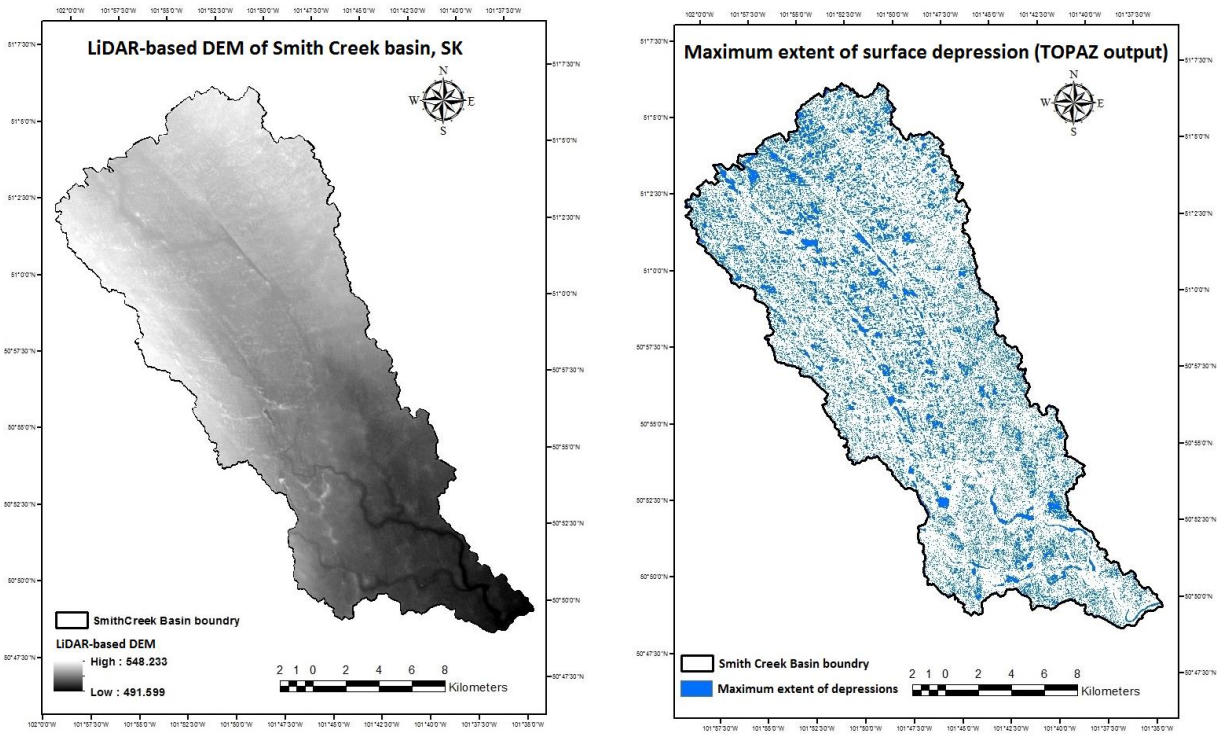

Figure 2.16. LiDAR-based DEM of Smith Creek basin (left), and the maximum extent of surface depressions (blue color) extracted from TOPAZ (right).

2.7 TOPAZ masking approach

The semi-automatic RADAR thresholding approach and a landscape analysis tool such as TOPAZ, which applies a LiDAR-based DEM, have been used in this study to delineate waterbodies from land in RADARSAT-2 intensity imagery. RADARSAT-2 threshold images were compared to the reference data (SPOT), and spurious patches of misclassified surface water area were found in thresholding images (Figure 2.17). The high soil moisture and smooth terrain might be two main causes for spurious detection of surface water areas in the thresholding images. To refine surface water classification in thresholding images, TOPAZ was used to mask and to remove RADARSAT-2-derived water features situated outside the maximum extent of depression areas generated by TOPAZ. The TOPAZ depression map was applied as a mask to reduce errors in the RADARSAT-2 thresholding images. This masked image provided the maximum possible

ponding area defined by TOPAZ from a high resolution Lidar-based DEM for both the St. Denis and Smith Creek research areas. Image masking involved overlaying the TOPAZ depression map and the RADARSAT-2 surface water thresholding map. A map Algebra expression was executed in the "Spatial Analyst" module in ArcGIS 10.3. The raster calculator tool allowed overlaying and extraction of the common areas of depression in TOPAZ and water areas detected in the RADARSAT-2 thresholding image to produce a new image layer called "RADARSAT-2 and "TOPAZ-masked" image (Figures 2.17, 2.18, and 2.19). Figure 2.20 illustrates the proposed methodology flow chart of surface water body mapping.

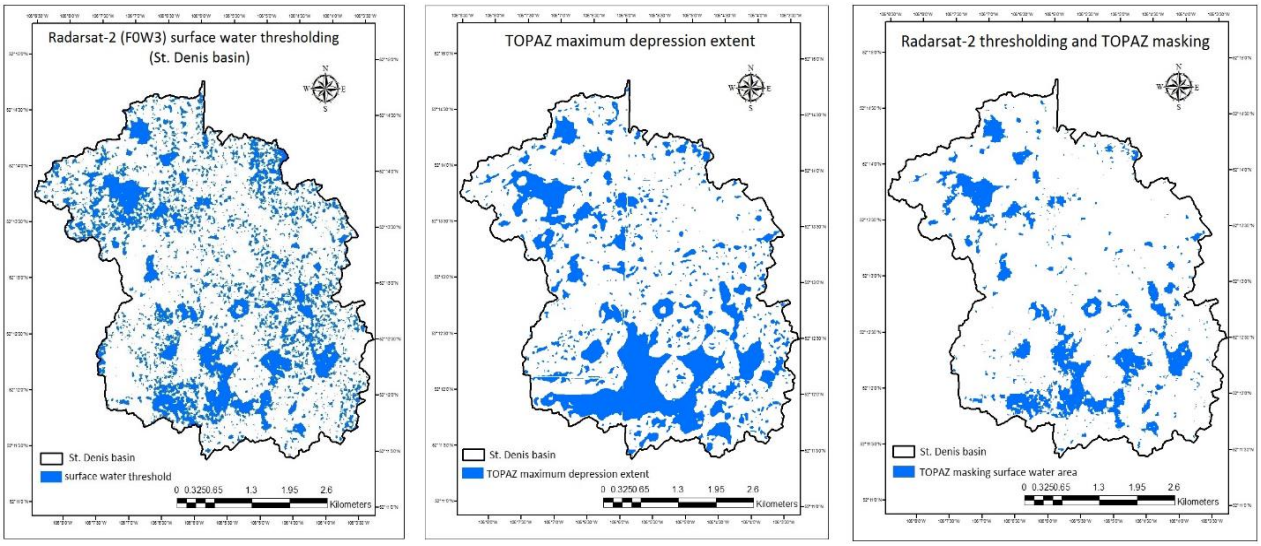

Figure 2.17. RADARSAT-2 Wide Fine beam mode surface water areas thresholding (left), the maximum depression extent derived using TOPAZ (middle), and RADARSAT-2 (F0W3) thresholding and TOPAZ-masked result (right), St. Denis basin (June, 2014).

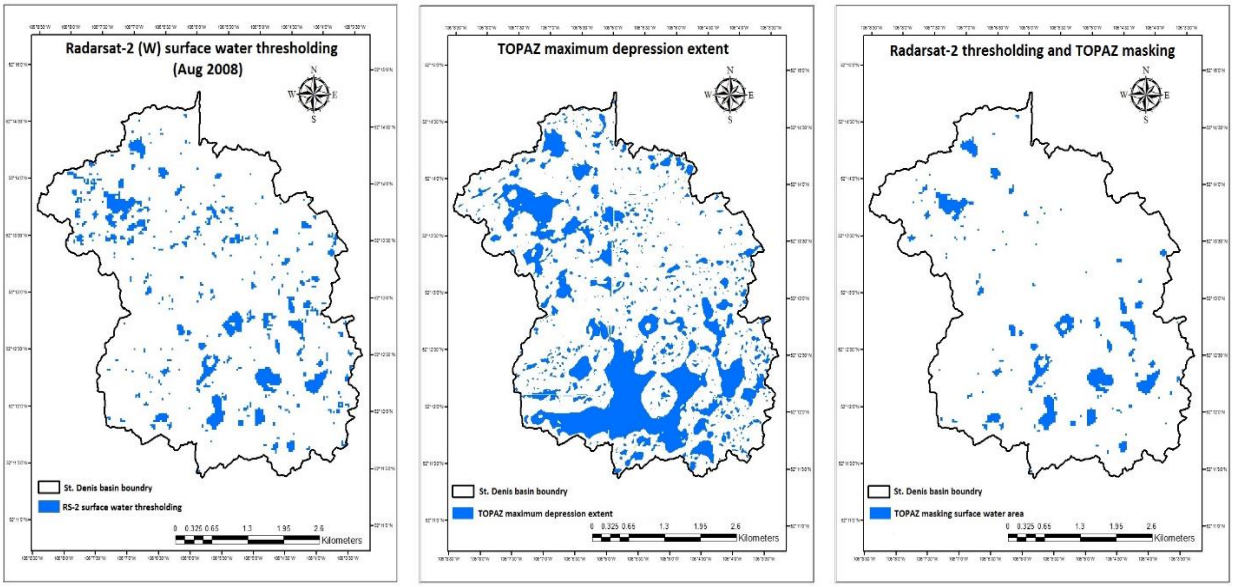

Figure 2.18. RADARSAT-2 Wide beam mode surface water areas thresholding (left), the maximum depression extent derived using TOPAZ (middle), and RADARSAT-2 (Wide) thresholding and TOPAZ-masked result (right), St. Denis basin (August, 2008).

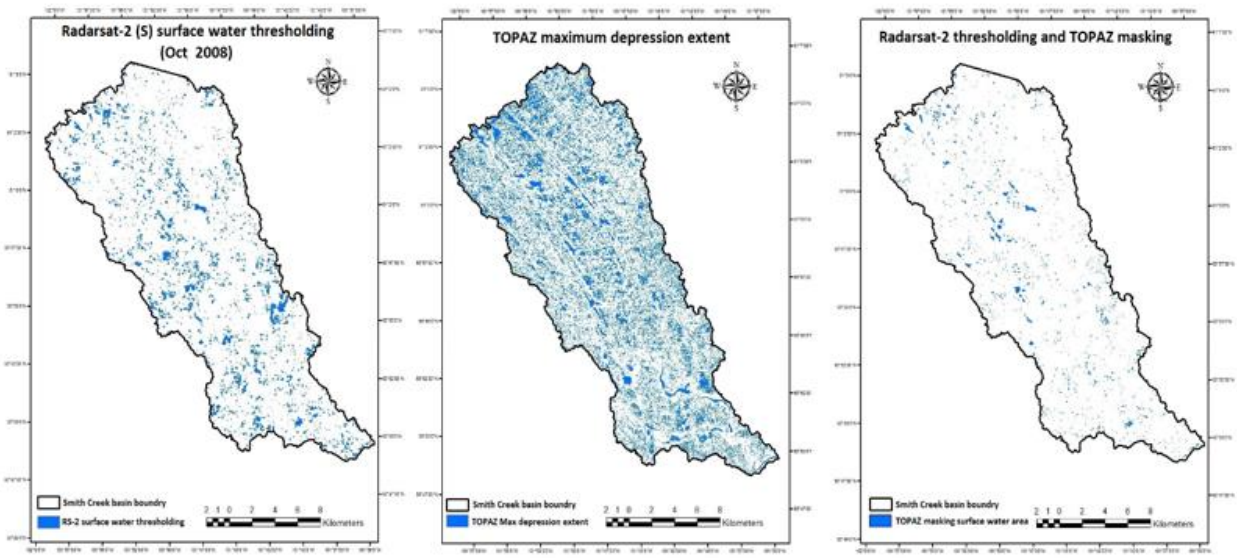

Figure 2.19. RADARSAT-2 Standard beam mode surface water areas thresholding (left), the maximum depression extent derived using TOPAZ (middle), and RADARSAT-2 (S3) thresholding and TOPAZ-masked result (right), Smith Creek basin (October, 2008).

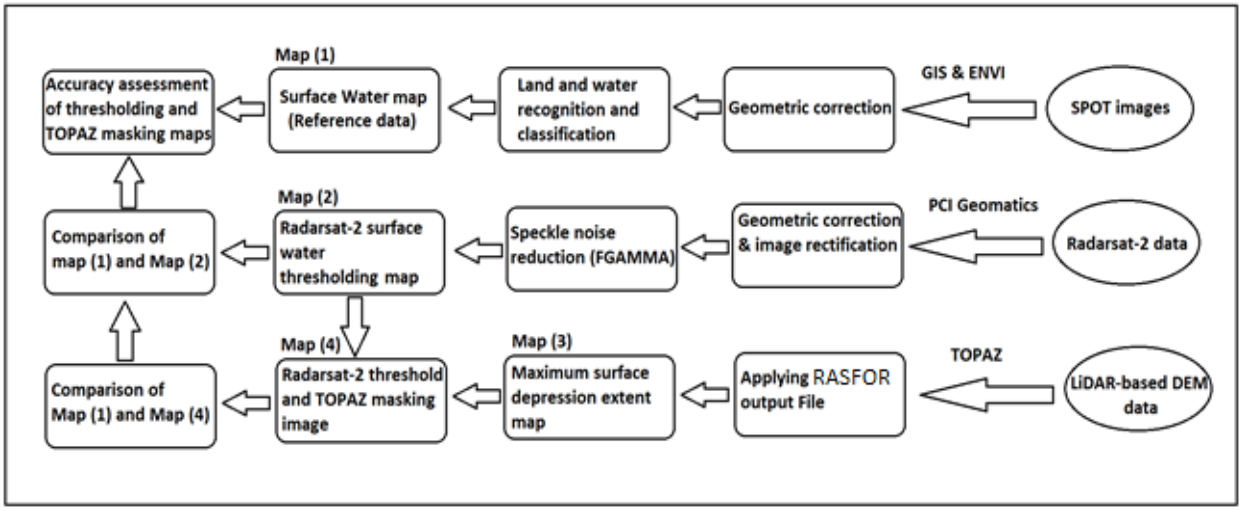

Figure 2.20. Methodology flow chart of water body mapping and accuracy assessment; RADARSAT-2 beam modes data processes in PCI Geomatics and thresholding method were applied; then LiDAR-based DEM was used as an input file into TOPAZ to obtain the masked image (maximum possible extent of the depressions); temporally concurrent high resolution SPOT images were then applied to determine the classification accuracy of the thresholding and TOPAZ masking method.

Chapter 3

Results and discussion

3.1 Validating of RADARSAT-2 thresholding and TOPAZ masking images using SPOT data

To validate the accuracy of surface water mapping, both the initial RADARSAT-2 thresholding images and the TOPAZ-masked images were compared with coincidently acquired SPOT images. Over both the St. Denis and Smith Creek basins, the RADARSAT-2 images and SPOT data were acquired more-or-less simultaneously. To identify and measure surface water map errors, an assessment of quantitative accuracy was completed. To assess the accuracy of surface water information derived from the initial RADARSAT-2 thresholding images and the TOPAZ-masked images, the detected surface water area was quantified in the GIS environment (spatial analyst operator) and then compared to high-resolution optical SPOT data for each beam mode. To better understand the different surface water maps generated by RADARSAT-2 thresholding, SPOT, and TOPAZ masking, a frequency distribution histogram of images (maps) was developed and analyzed. This allowed consideration of how mapping results varied with pond size.

3.2. Comparison of RADARSAT-2 thresholding images to SPOT data

3.2.1 RADARSAT-2 (F0W3) thresholding image versus SPOT-6 data (St. Denis basin)

The accuracy of the surface water derived from a RADARSAT-2 (F0W3) thresholding image (effective resolution 8m) was evaluated by comparing the surface water area detected in a RADARSAT-2 (F0W3) thresholding image with that detected nearly simultaneously in a SPOT-6 image taken on 25 June 2014. Previous research suggests that Wide Fine thresholding images are highly sensitive to high soil moisture and smooth terrain effects (Bolanos et al., 2016). Figure

3.1 indicates that, as expected, the RADARSAT-2 thresholding image overestimated the surface water area. The results show that when the Fine Wide (F0W3) mode was used, the RADARSAT-2 thresholding method classified 577ha of the basin as surface water area. However, according to SPOT-6 data, 231ha of the basin were covered by open surface water. It can thus be concluded that in the Wide Fine surface water thresholding image, 346ha were misclassified. For accurate assessment, the SPOT image resolution was resampled from 6m to the size of the RADARSAT-2 image resolution (8m) to match the pixel size in both images The spatial analyst operator in the GIS environment was applied to compute the common surface water area in both the RADARSAT-2 (F0W3) thresholding and SPOT-4 images.

The surface water area was measured and quantitatively compared in all maps. The classification accuracy of the surface water was then calculated by dividing the total common surface water area in the RADARSAT-2 (F0W3) thresholding image and SPOT-6 data by the total surface water area in the RADARSAT-2 (F0W3) thresholding image (208/577=36%). According to the SPOT-6 image, the classification accuracy of the RADARSAT-2 (F0W3) thresholding image was 36% of the total surface water areas detected in the SPOT-6 image.

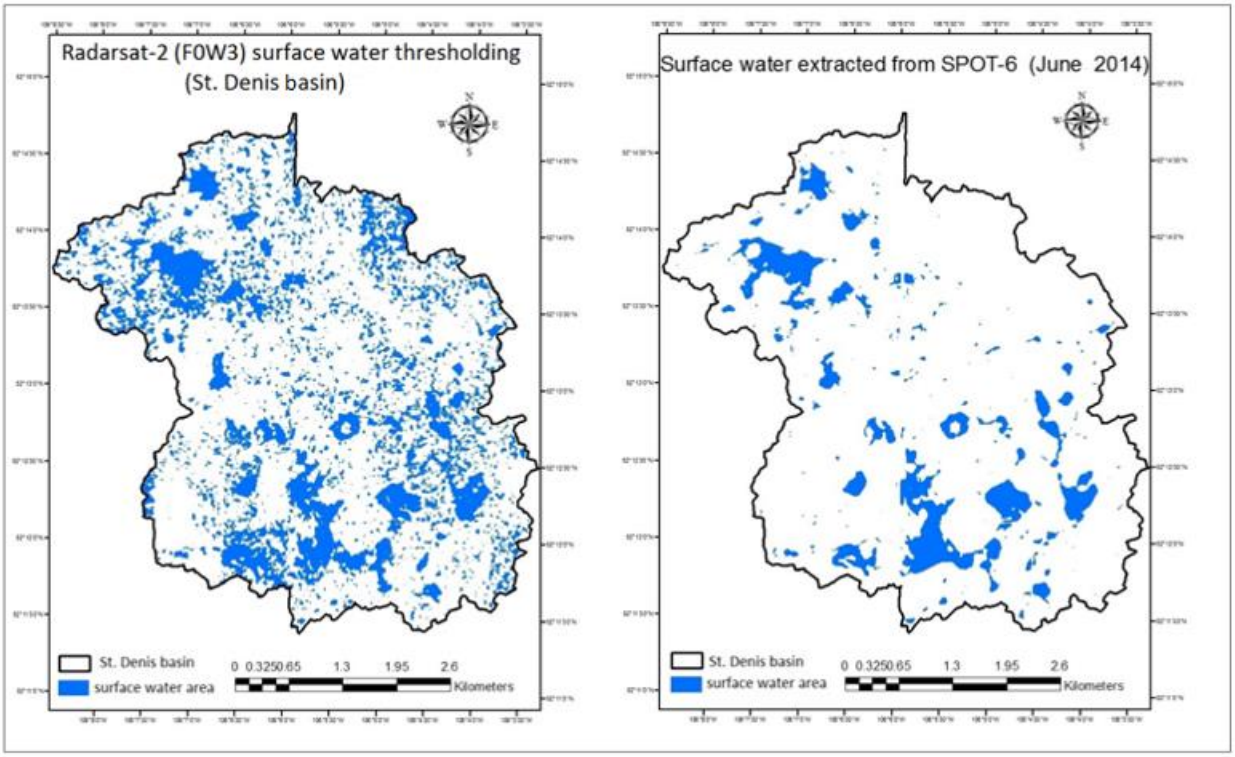

Figure 3.1. Comparison of an RS-2 (F0W3) surface water thresholding image (left) and extracted surface water from a SPOT-6 image (acquired coincidently) depicts the spurious detection of surface water in a F0W3 thresholding image over the St. Denis basin (June 2014).

3.2.2 RADARSAT-2 (W2) thresholding image versus SPOT-4 data (St. Denis research basin)

The RADARSAT-2 Wide beam mode with an effective resolution of 30m was chosen and processed to examine its ability to detect surface water area over the St. Denis research basin (Figure 3.2). The RADARSAT-2 Wide beam mode image was evaluated against detected surface water from a temporally concurrent SPOT-4 data (20m) taken in August 2008. The outcome from the RADARSAT-2 (W2) thresholding image showed that 187ha of the basin were classified as surface water area. However, according to the SPOT-4 data, 181ha of the basin were covered by open surface water. Thus, the total pixels selected as surface water area in the thresholding image may not necessarily be the same pixels detected as surface water area in the SPOT data. To match the pixel size in both images, the SPOT-4 image resolution was resampled from 20m to the size

of RADARSAT-2 Wide resolution (30m). A spatial analyst operator in the GIS environment was applied to compute the common surface water area in the RADARSAT-2 Wide thresholding image and in the SPOT-4 data. Between the RADARSAT-2 (W) thresholding image and SPOT-4 data, the area of 89ha was measured and calculated as a common surface water area. The classification accuracy of the surface water was determined by dividing the total surface water area common to both the RADARSAT-2 (W) thresholding image and SPOT-4 data by the entire surface water area in the RADARSAT-2 (W) thresholding image (89/187 = 47%). The surface water classification accuracy in the Wide mode thresholding image was 47% (Table 3.2), when it was compared to a high-resolution SPOT-4 data. The accuracy of the RADARSAT-2 Wide thresholding images are higher at coarser resolutions because many small ponds are not detected when soil moisture is low in dry seasons.

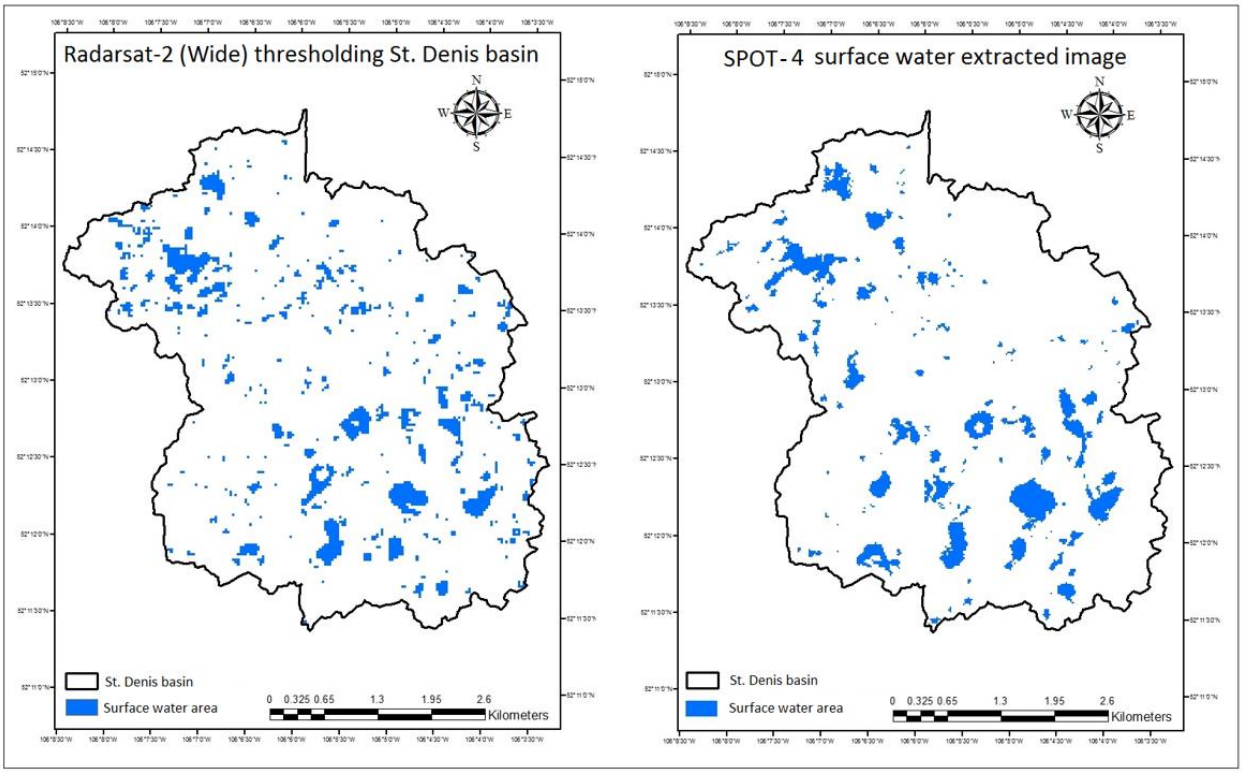

Figure 3.2. Comparison of an RS-2 Wide (30m) surface water thresholding image (left) and detected surface water from a SPOT-4 image (right) depicts the spurious surface water pixels on a RADARSAT-2 (W2) thresholding image over St. Denis basin (August 2008).

3.2.3 RADARSAT-2 (S3) thresholding image versus SPOT-5 data (Smith Creek research basin)

To evaluate the classification accuracy of the surface water area in a RADARSAT-2 (S3) image (30m), a RADARSAT-2 (S3) thresholding image was compared to a SPOT-5 data (Figure 3.3). RADARSAT-2 (S3) data were acquired in October 2008, nearly concurrently with the acquisition of SPOT-5 data (10m) over the Smith Creek basin. The results from the thresholding method of RADARSAT-2 (S3) show that 1192ha of the basin were classified as surface water area in the thresholding image. According to SPOT-5 data, 1427ha of the basin were detected as open surface water. The classification accuracy of the RADARSAT-2 (S3) thresholding image is shown as 21% of the total detected surface water areas from the SPOT-5 image. Thus, the results from the RADARSAT-2 Standard mode thresholding approach in mapping surface water areas demonstrate lower accuracy than the F0W3 Wide mode image.

3.2.4 RADARSAT-2 beam mode resolution and landscape effects

An image from the RADARSAT-2 S3 mode has the same spatial resolution size (30m) as a Wide mode image. However, the Wide mode surface water thresholding results from the St. Denis basin (47%) demonstrated better results than the Standard mode (21%). In addition to only resolution effects, surface water classification accuracy can be influenced by several other factors, including the time of year the RS-2 image is acquired, landscape, soil moisture content, and size of potholes.

1. RADARSAT-2 acquisition time: The time of year at which RADARSAT-2 (S3) images are taken can influence the results. For example, if RADARSAT-2 images are taken in the Prairie Pothole region (PPR) in summer or fall, soil moisture content is typically lower than at other times of year.

2. Soil moisture content: When soil moisture in basins being photographed is low (such as in the summer or in times of drought), the detection of surface water can be underestimated. The S3 image from the current study was taken in October 2008. Thus, this needed to be considered in the results.
3. Landscape: Features of the terrain can influence results. The beveled-till plain landscape in Smith Creek basin and its slope of 2-5% (low relief terrain) can substantially influence the RADARSAT-2 (S3) thresholding results, regardless of spatial resolution. Such differences likely caused a difference of 26% in classification results compared to Wide mode (W2) thresholding results (Figure 3.4).
4. Pothole size: The dimensions of potholes can also affect results. Smith Creek basin is dominated by an abundance of small isolated surface ponds. For instance, for area intervals less than 1ha, out of 2396 ponds detected as surface water bodies in the SPOT-5 image, 923 ponds were not detected in the RADARSAT-2 (S3) thresholding image.

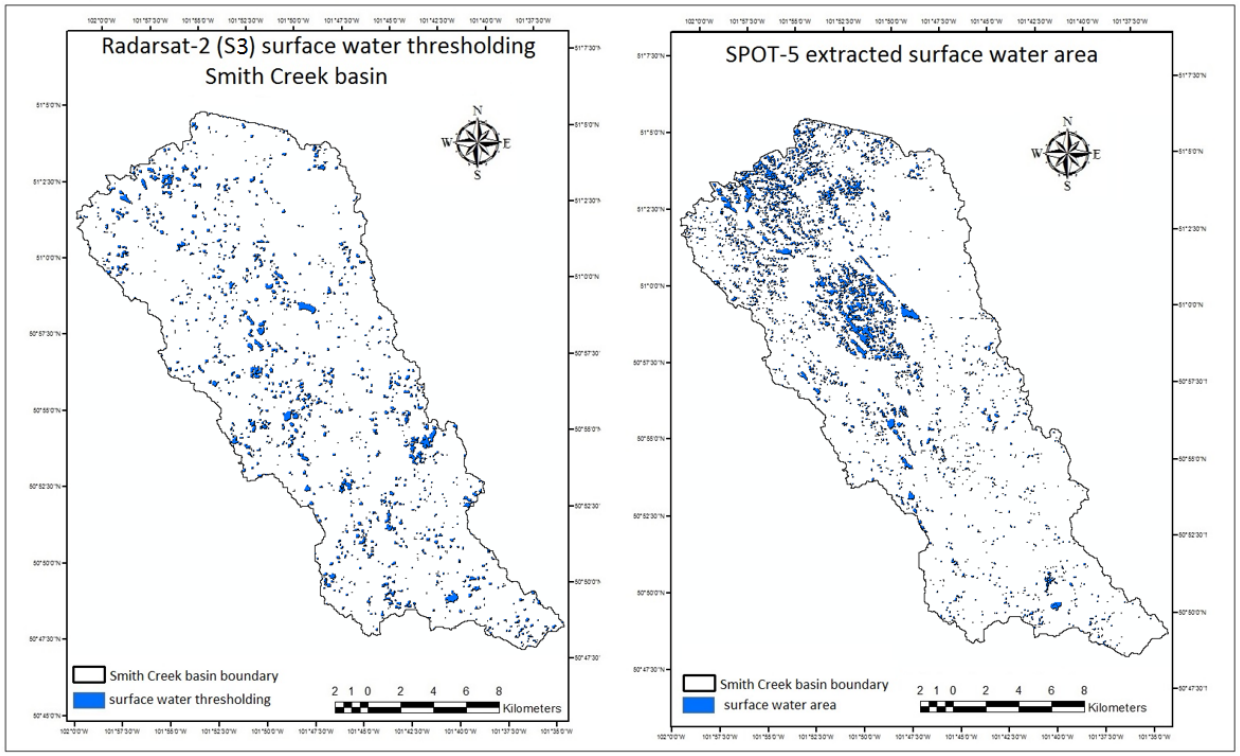

Figure 3.3. Comparison of an RS-2 Standard (S3) surface water thresholding image (left) and detected surface water from a SPOT-5 image (nearly temporally coincident), depicting the spurious surface water pixels on a RADARSAT-2 (S3) thresholding image over Smith Creek basin.

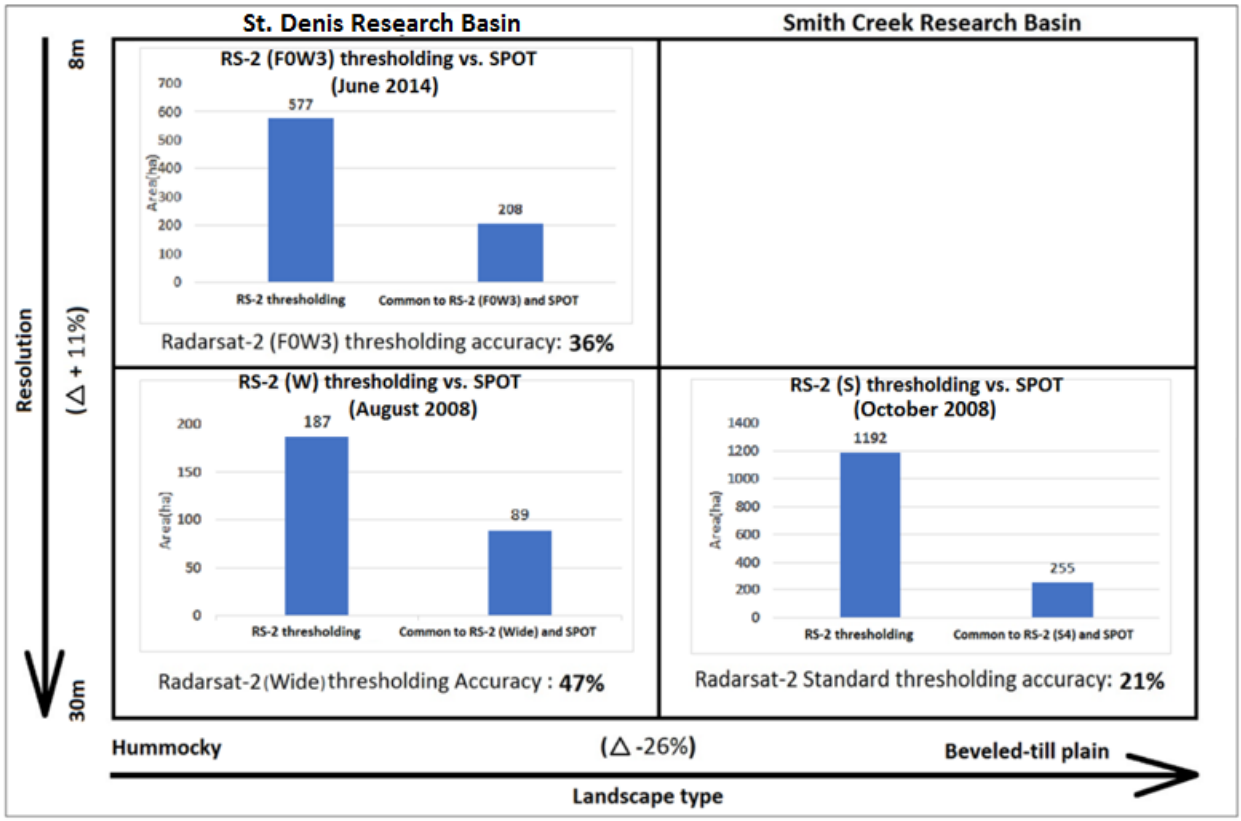

Figure 3.4. Comparison of a detected surface water area from RADARSAT-2 beam modes thresholding and SPOT images in two study basins shows higher accuracy obtained in W2 thresholding than in S3 thresholding, with the same nominal spatial resolution. The same comparison with F0W3 and W2 also shows better accuracy with a W2 beam mode thresholding image.

3.3. Comparison of TOPAZ-masked images and SPOT data

3.3.1 RADARSAT-2 (F0W3) TOPAZ-masked image versus SPOT-6 image (St. Denis basin)

The surface water area from a RADARSAT-2 (F0W3) TOPAZ-masked image was compared with those areas derived from a SPOT-6 image taken on June 2014 (Figure 3.5). From a surface water area of 577ha detected in a Fine Wide thresholding image, 280ha were extracted as surface water from the TOPAZ-masked image (Table 3.1). Using a TOPAZ-masking technique, the area of 297ha was removed from the RADARSAT-2 (F0W3) thresholding image. The common surface water area in the RADARSAT-2 (F0W3) TOPAZ-masked image and the SPOT-6 image

was computed and extracted. An area of 229ha was measured as common surface water area in both images. The surface water classification accuracy was determined by dividing the total common surface water area in the RADARSAT-2 (F0W3) TOPAZ-masked image and the SPOT-6 images by the total surface water area in the RADARSAT-2 (F0W3) TOPAZ-masked image (229/281=81%). TOPAZ masking on F0W3 beam mode thresholding showed an effective result and, thus, it can be concluded that removing misclassified pixels can likely improve the classification accuracy of surface water. The classification accuracy of TOPAZ masking on F0W3 mode thresholding was much higher (81%) than that of the thresholding result (36%). The surface water classification accuracy of the RADARSAT-2 F0W3 image was increased substantially by applying a TOPAZ-derived depression mask image in the St. Denis research basin (Table 3.1).

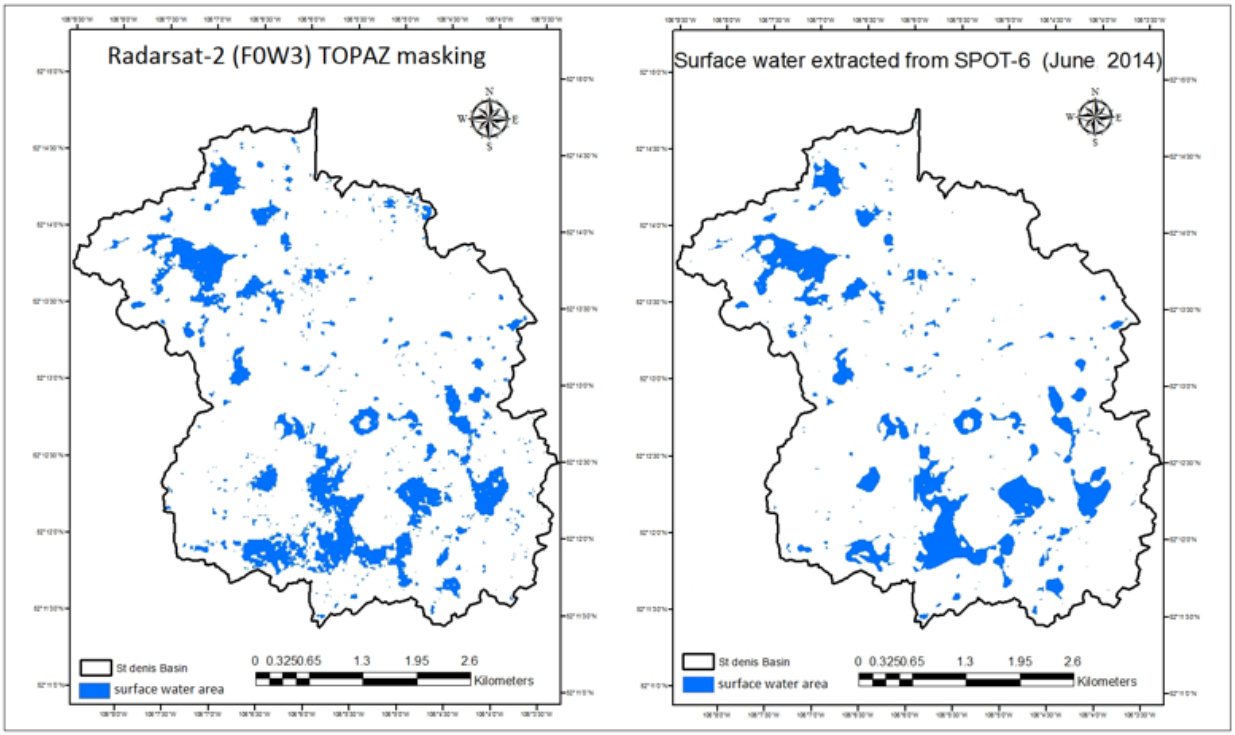

Figure 3.5. Comparison of a RADARSAT-2 (F0W3) surface water TOPAZ masking image (left) and detected surface water from a SPOT-6 image (acquired nearly coincident) and showing that spurious noise is reduced in the thresholding image.

Table 3.1. Surface water and land discrimination according to surface area (ha) in each individual data set in St. Denis basin. The accuracy of thresholding and the TOPAZ masking approach is calculated based on the SPOT image as reference data.

RADARSAT-2 Wide Fine (St. Denis study basin)		
	Area (ha)	
	Water	Land
RS2-Threshold (-17) 8m*8m	577	1643
SPOT 6m*6m	231	1989
RS2-Threshold VS. SPOT 8m*8m	208	2012
RS2-Threshold TOPAZ Masking 8m*8m	281	1935
RS2 TOPAZ masking VS. SPOT	229	1985
RS-2 Thresholding Accuracy = 36% **RS-2 Thresholding-TOPAZ masking Accuracy = 81%**		

3.3.2 RADARSAT-2 (W2) TOPAZ-masked image versus SPOT-4 data (St. Denis basin)

A RADARSAT-2 (W2) TOPAZ-masking image was compared to a surface water map derived from a SPOT-4 image (Figure 3.6). According to the SPOT data, 180ha of the basin were covered by open surface water, whereas the TOPAZ-masking approach produced only 114ha (Table 3.2). Using the TOPAZ-masking technique, an area of 73ha was removed from the RADARSAT-2 thresholding image. The common surface water area in the RADARSAT-2 (W2) TOPAZ-masked image and the SPOT-4 image were then extracted, and an area of 86ha was measured as surface water area common to both images. The surface water classification accuracy was computed by dividing the total common surface water area in the RADARSAT-2 (W2) TOPAZ-masked image and the SPOT-4 data by the total surface water area in the RADARSAT-2 (W2) TOPAZ-masked image (86/114=75%). In the TOPAZ-masked image, the classification accuracy increased from 47% in the thresholding image to 75% after applying the TOPAZ-masking method. In comparison with the RADARSAT-2 (W2) thresholding results, TOPAZ

masking was effective in removing spurious pixels not in depressions mapped by TOPAZ. In the W2 mode image, the TOPAZ masking approach was able to improve the surface water classification accuracy by 28%. The classified surface water area for the TOPAZ-masked image was depicted to facilitate the comparison of Fine Wide and Wide mode image results (Figure 3.8). After applying TOPAZ masking over the RADARSAT-2 (W2) thresholding image, surface water classification accuracy increased to 75%. Thus, it can be concluded that TOPAZ masking was able to increase the accuracy of classification in both Wide Fine and Wide mode regardless of the image resolution. However, the TOPAZ-masking classification accuracy of surface water in Fine Wide mode was 6% higher than that of the Wide mode image (Figure 3.8).

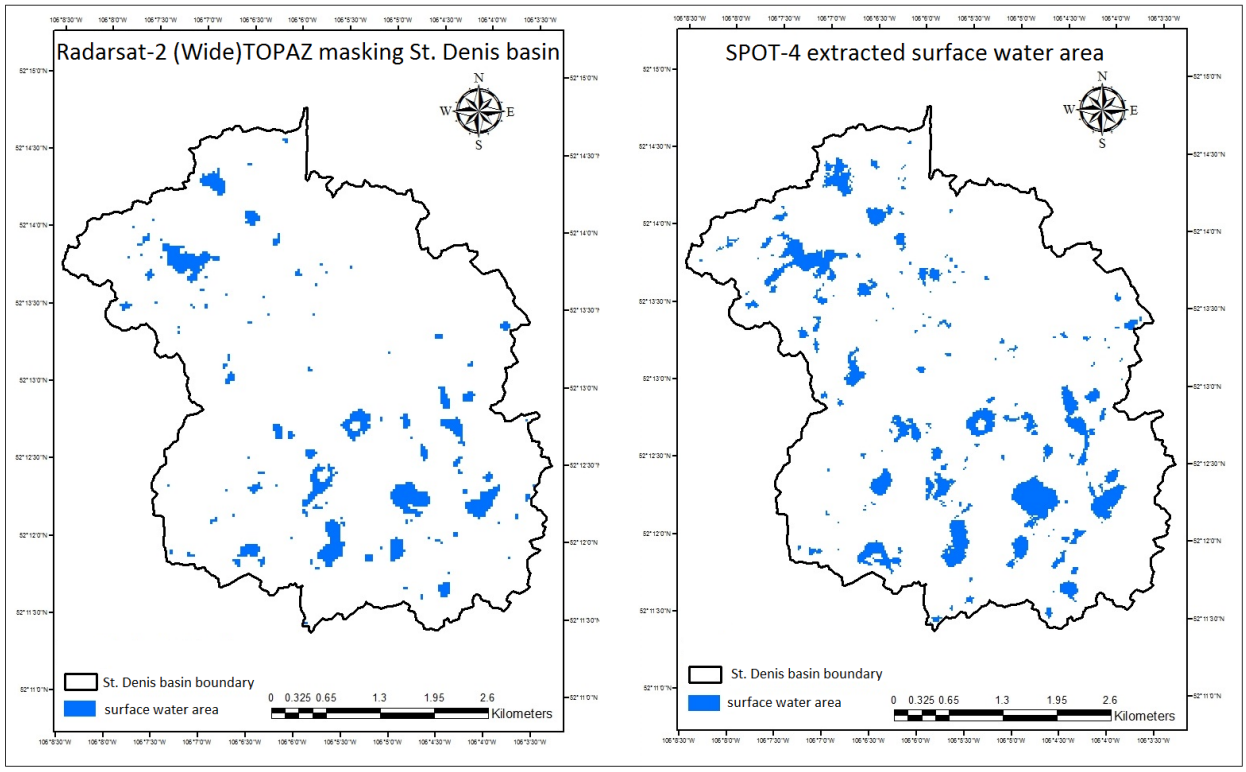

Figure 3.6. A comparison of an RS-2 (W2) surface water TOPAZ-masking image (left) with detected surface water from a SPOT-4 image (acquired nearly coincident) illustrates the reducing emergent noise on the thresholding image

Table 3.2. Surface water and land discrimination according to surface area (ha) for each individual data set in St. Denis basin. The accuracy of the W2 mode thresholding and TOPAZ-masking approach were calculated based on a SPOT image as reference data.

RADARSAT-2 Wide 2 mode (St. Denis study basin)		
	Area (ha)	
	Water	Land
RS2-Threshold (-16) 30m*30m	187	2035
SPOT-4 20m*20m	180	2040
RS2-Threshold VS. SPOT	89	2130
RS2-Threshold TOPAZ Masking	114	2106
Threshold-TOPAZ masking VS. SPOT	86	2136
RS-2 thresholding Accuracy = 47% **RS-2 thresholding-TOPAZ masking Accuracy = 75%**		

3.3.3 RADARSAT-2 (S3) TOPAZ-masked image versus SPOT-5 data (SCRB)

A RADARSAT-2 (S3) TOPAZ-masked image was compared against surface water area extracted from a SPOT-5 image taken in October 2008 over Smith Creek study basin (Figure 3.7). From 1192ha of detected surface water in the RADARSAT-2 (S3) thresholding image, 467ha was selected as surface water by the TOPAZ-masked image (Table 3.3). The area of 725ha was removed by the TOPAZ-masking technique from the RADARSAT-2 (S3) thresholding image. The common surface water area in the RADARSAT-2 (S3) TOPAZ-masked image and the SPOT-5 image was calculated. The area of 226ha was measured as surface water area common to both images. The surface water classification accuracy was determined by dividing the total common surface water area in the RADARSAT-2 (S3) TOPAZ-masked and SPOT-6 images by the entire surface water area in the RADARSAT-2 (S3) TOPAZ-masked image (226/467=48%).

TOPAZ masking on S3 beam mode thresholding showed that removing pixels not in depressions mapped by TOPAZ could improve the surface water classification accuracy. After

TOPAZ masking was applied at the Smith Creek research basin, the accuracy of the surface water classification in RADARSAT-2 (S3) increased from 21% (thresholding image) to 48% (Table 3.3). The surface water classification accuracy in the RADARSAT-2 S3 image was increased by applying a TOPAZ-derived depression mask image in the Smith Creek basin. However, although TOPAZ masking was able to increase the accuracy of classification in S3 mode, this level of accuracy (48%) may not be reliable for operational surface water monitoring and mapping.

3.3.4 RADARSAT-2 TOPAZ-masked resolution and landscape effects

TOPAZ masking increased the accuracy of classification in both S3 (Smith Creek basin) and W2 mode (St. Denis basin) thresholding images. The same image resolution (30m) with the same polarization (HH) of W2 and S3 mode led to different surface water classification accuracy (Figure 3.8). The results show that the difference of 27% accuracy was achieved when the W2 mode image was masked by TOPAZ in improved surface water mapping. However, the landscape factor should also be considered in this accuracy difference. As mentioned, the St. Denis basin has a hummocky landscape and large ponds, while the Smith Creek basin has a beveled-till plain and smaller ponds. These landscape differences might influence the mapping accuracy of surface water as much as resolution effects. Thus, the effect of landscape on surface water classification accuracy should be considered in RADARSAT-2 beam mode studies. In this study, a surface water mapping technique was tested on study areas in PPR with low-terrain landscapes, and similar results may not be obtained if the approach were applied to high-terrain landscape. Table 3.4 shows the total surface water area measured in all RADARSAT-2 thresholding, TOPAZ masking, and SPOT images in this study.

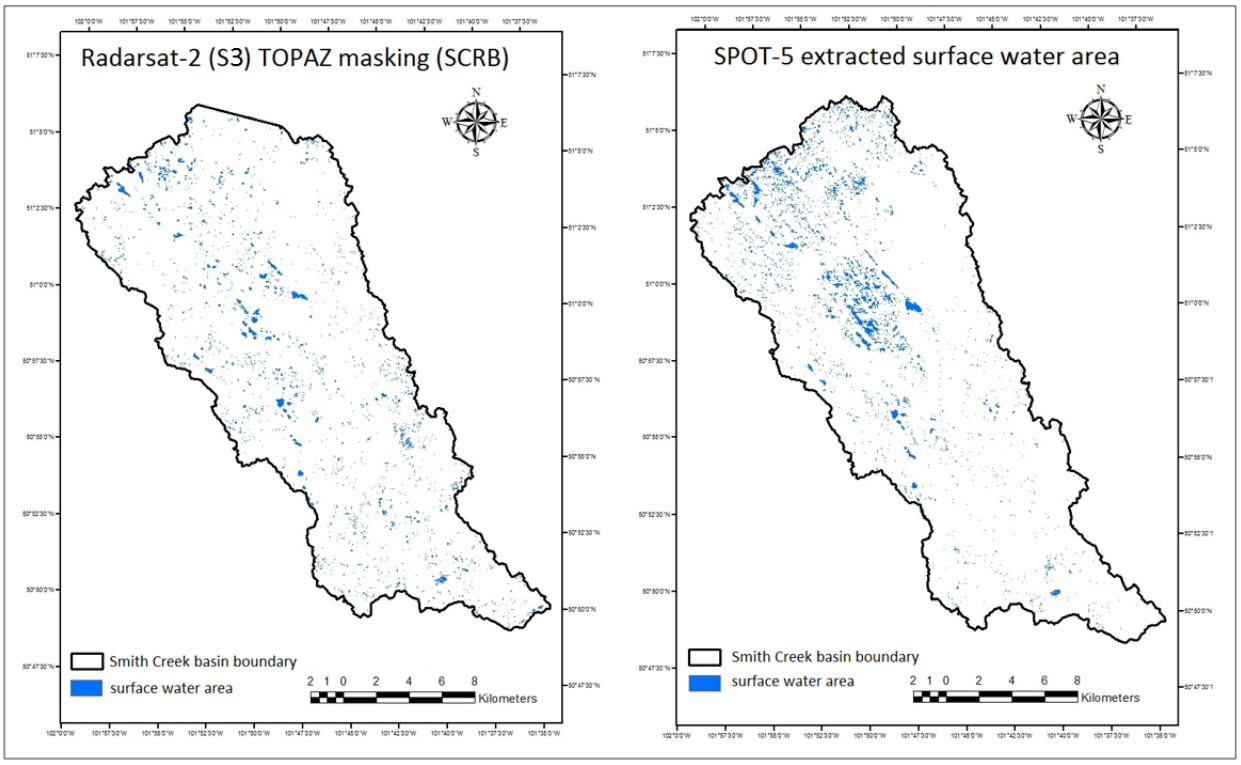

Figure 3.7. Comparison of an RS-2 (S3) surface water TOPAZ-masking image (left) and detected surface water from a SPOT-5 image (acquired coincidently) illustrates the reduced spurious noise on the thresholding image.

Table 3.3. Surface water and land discrimination according to total surface area (ha) for each individual dataset in Smith Creek basin. The accuracy of S3 mode thresholding and the TOPAZ-masking approach was calculated based on using a SPOT image as reference data.

RADARSAT-2 Standard-3 mode (Smith Creek research basin)		
	Area (ha)	
	Water	Land
RS2-Threshold (-17)	1192	37475
SPOT 10m*10m	1427	37232
RS2-Threshold VS. SPOT	255	38408
RS2-Threshold TOPAZ Masking	467	38170
Threshold-TOPAZ masking VS SPOT	226	38412
RS-2 Thresholding Accuracy = 21% **RS-2 Thresholding-TOPAZ masking Accuracy = 48%**		

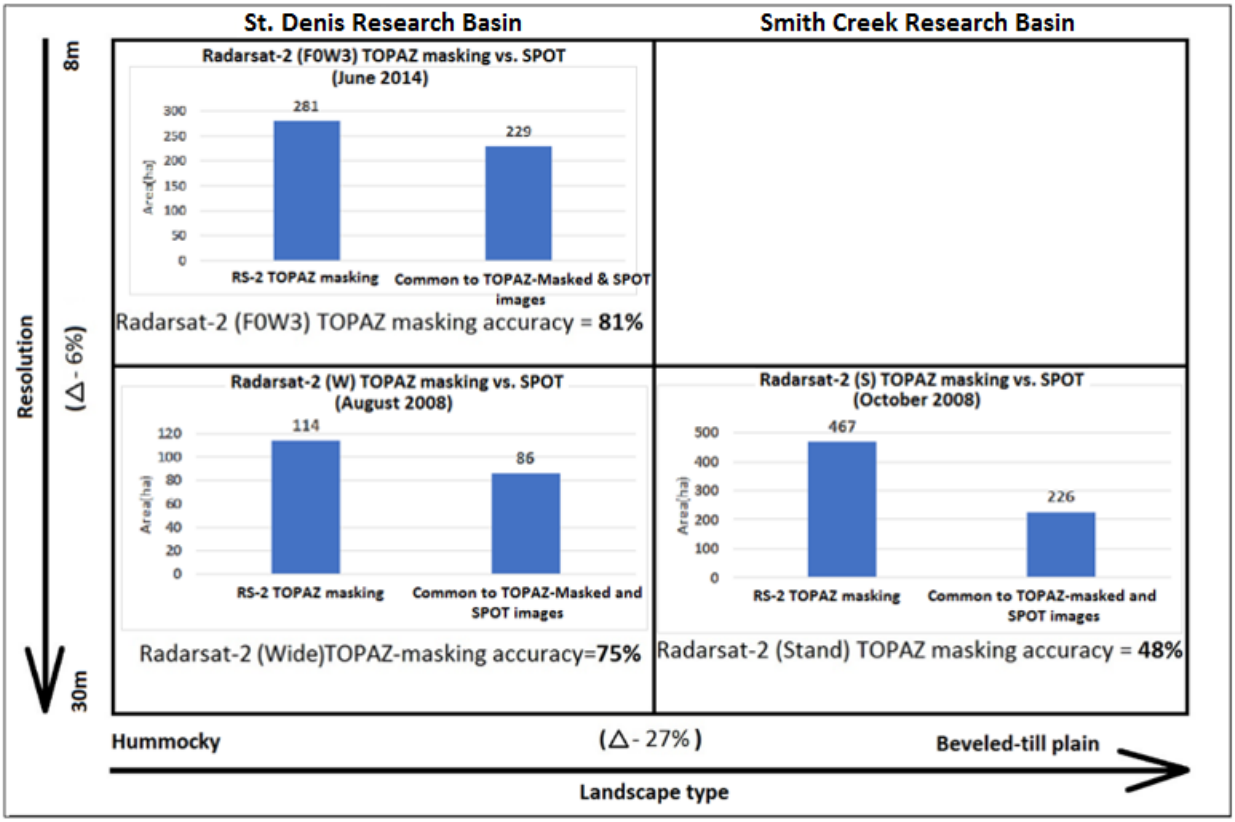

Figure 3.8. Comparison of detected surface water area from RADARSAT-2 beam modes, TOPAZ masking and SPOT images in two study basins demonstrates that TOPAZ masking can decrease the large number of misclassified pixels in RADARSAT-2 thresholding images. The accuracy of TOPAZ masking decreased from Wide F0W3 to W2 mode (6%). The accuracy of TOPAZ masking was decreased in S3 mode in comparison to W2 mode (27%).

Table 3.4. The surface water areas in RADARSAT-2 beam mode(s) HH polarization thresholding and corresponding TOPAZ-masked and SPOT surface water layers.

Research basin, RS-2 beam mode & Time of acquisition	**RS-2 Thresholding surface water (ha)**	**RS2-TOPAZ-masked surface water areas (ha)**	**SPOT surface water areas (ha)**
St. Denis study basin, (F0W3), June 2014	577	281	231
St. Denis study basin, (W2), August 2008	187	114	180
Smith Creek study basin, (S3), October 2008	1192	468	1427

3.4 Surface water frequency distribution analysis over St. Denis and Smith Creek basins

The spatial pattern of potholes and the topography are variable throughout PPR. To facilitate the comparison of RADARSAT-2 surface water thresholding images, TOPAZ-masked images and SPOT data, frequency distribution histograms were computed to show the number of detected surface water bodies (ponds) for nine separate area intervals over St. Denis and Smith Creek basins. To develop a frequency distribution histogram based on the number of surface waterbodies in a GIS software, the extracted surface water areas from RADARSAT-2 thresholding, SPOT, and TOPAZ-masked images were converted to polygons. The smallest area intervals for all three data sets in each study basin were considered as 0.1-0.5ha, and the largest area interval assigned was as large as >50ha. The number of small ponds was comparatively higher when the RADARSAT-2 (F0W3 and W2) thresholding method was used to map surface water area but dropped substantially when TOPAZ masking was applied. The frequency distribution histograms were calculated for three datasets and are described in the following section.

3.4.1 RADARSAT-2 (F0W3) Surface water frequency distribution analysis (St. Denis basin)

In the RADARSAT-2 (F0W3) thresholding image, the resolution was robust enough to detect small ponds. However, because RADARSAT-2 (F0W3) is highly sensitive to soil moisture content (soil wetness), small patches of wet areas that are not surface water (ponded areas) inside depressions causes this thresholding method to overestimate the number of detected small ponds as surface water (Figure 3.9). From the total number of 359 detected ponds in the thresholding image in the current study, the TOPAZ-masking approach eliminated 206 of the wet areas from the thresholding method. In the TOPAZ-masked image, the number of surface waterbodies in

larger area intervals mostly corresponds to the number of detected surface water bodies in the SPOT image.

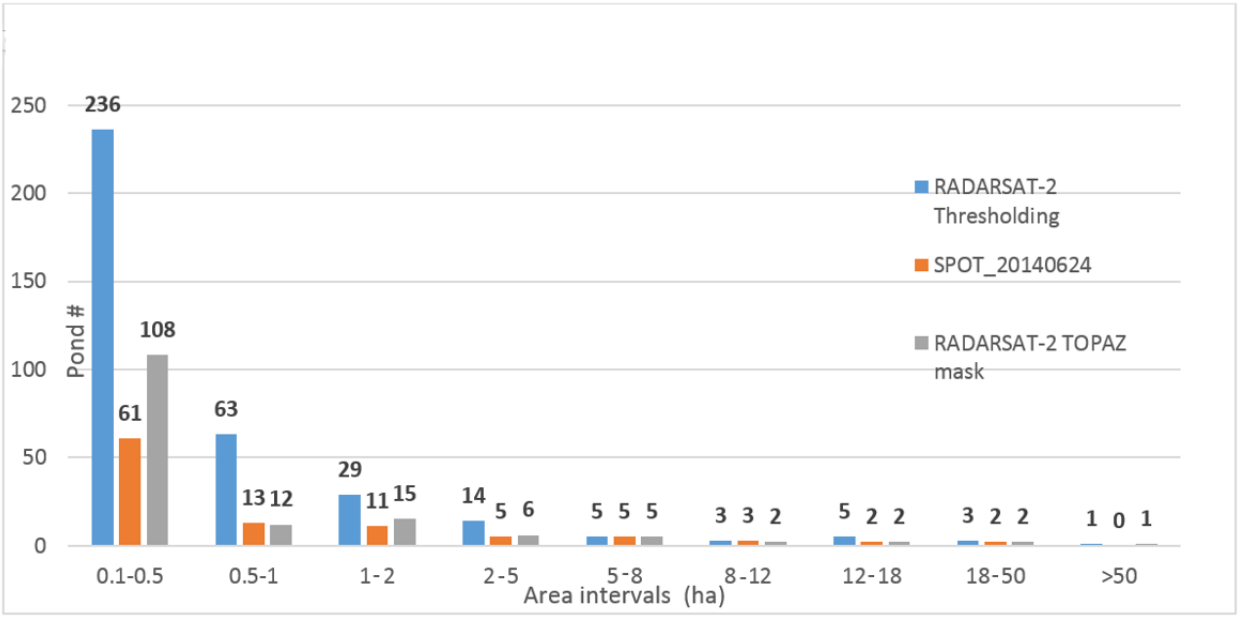

Figure 3.9. Frequency distribution histogram of surface water ponds detected by RADARSAT-2 F0W3 thresholding, TOPAZ masking and the SPOT image in different area intervals, St. Denis basin.

The frequency distribution histogram of surface water area was used to show how a TOPAZ-masking image can improve the classification of surface water area in a thresholding (F0W3) image for every designated area interval. A further comparison of RADARSAT-2 (F0W3) surface water thresholding results relative to SPOT before and after TOPAZ masking was made using a frequency distribution histogram of total surface water area for each area interval (Figure 3.10). The frequency distribution histogram of surface water area shows that all area intervals typically follow the same distribution histogram pattern as the number of detected ponds in each of those intervals (Figure 3.10). Likely because of problems with surface water class assignments, in all area intervals except for area interval 8-12ha, the surface water area in the Fine Wide thresholding image overestimated the detection of surface water area when compared to the SPOT-

6 image. From the total of 577ha of surface water area detected in the (F0W3) thresholding image, TOPAZ masking eliminated 297ha of misclassified areas from the RADARSAT-2 (F0W3) thresholding image.

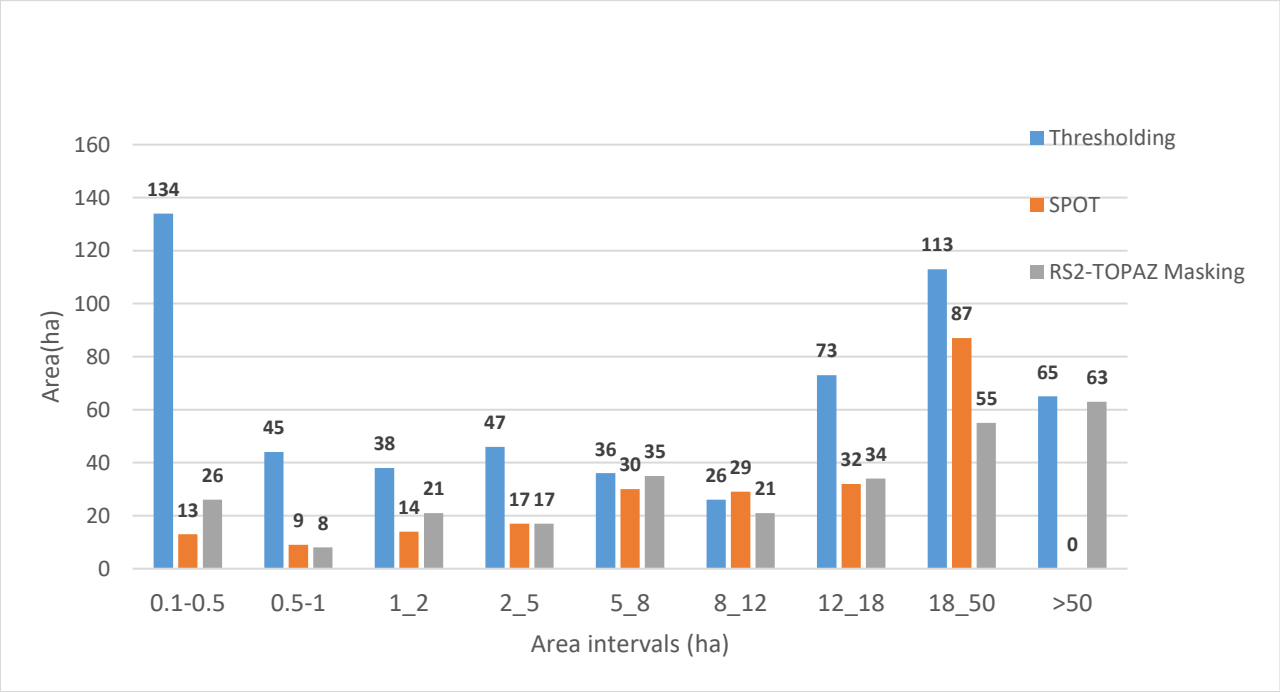

Figure 3.10. Surface water area detected in RS-2 Fine Wide, SPOT and TOPAZ masking in different area intervals; the TOPAZ masking eliminated non-water classified areas from the thresholding image.

3.4.2 RADARSAT-2 (W2) surface water frequency distribution analysis

Quantifying surface water area based on polygons of a defined range (area intervals) can help explain the ability of different RADARSAT-2 modes to map water. From the total number of 285 detected ponds in the W2 mode thresholding image, 180 non-water patches were eliminated from the RADARSAT-2 W2 thresholding image by the TOPAZ-masking approach. The number of detected surface water bodies in area intervals smaller than 1ha were substantially higher than

those detected from the SPOT image (Figure 3.11). Because of a decline in total surface water area in the W2 image (August 2008) in comparison to the F0W3 (June 2014) image, ponds in the area intervals larger than 18ha were neither detected in RADARSAT-2 Wide mode thresholding nor in SPOT-4 data. Because it influences the detection of ponds in the RADARSAT-2 data, the hydrological status (soil wetness) of the basin should be considered at the time of RADARSAT-2 acquisition. In the current study, the W2 mode was acquired in a hydrologically dry year (in August 2008), and the F0W3 mode was taken in a comparatively wetter year (in June 2014). Owing to a coarser resolution and a loss of total surface water area in the W2 mode, the time of acquisition likely accounted for the total reduction in the number of ponds captured in the images over St. Denis basin in August 2008 (Figure 3.11).

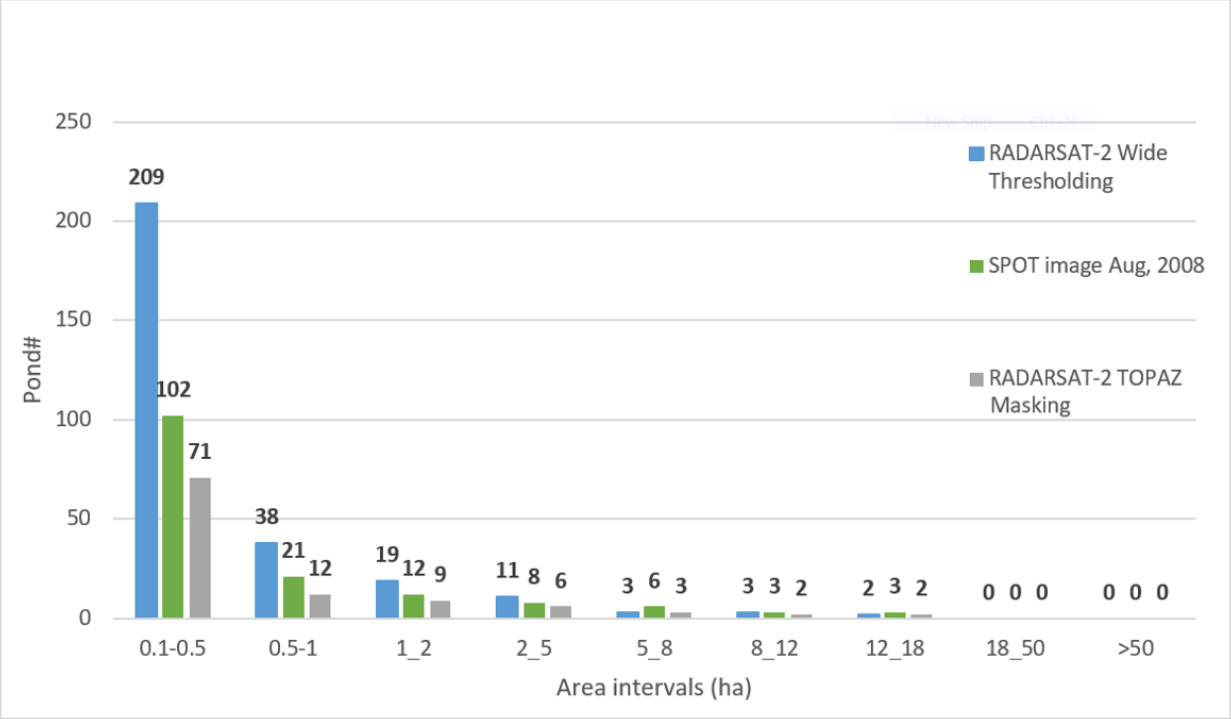

Figure 3.11. Frequency distribution histogram of surface water ponds detected by RADARSAT-2 Wide mode thresholding, TOPAZ masking, and SPOT image in different area intervals, St. Denis basin.

As mentioned, a frequency distribution histogram was computed to suggest how a TOPAZ-masked image can impact the extraction of surface water areas in a W2 thresholding image. To enable the comparison of RADARSAT-2 (W2) thresholding, TOPAZ masking, and SPOT data, a frequency distribution histogram of surface water areas for each area interval was calculated and depicted for the St. Denis study basin (Figure 3.12). From the total of 187ha surface water area detected in the W2 thresholding image, TOPAZ masking eliminated 73ha as spurious surface water area from the RADARSAT-2 (W2) thresholding image. In the area intervals larger than 5ha, the RADARSAT-2 W2 thresholding failed to properly detect surface water area in comparison with SPOT-4 data. The image resolution can affect the number of ponds and the area of surface water in each area interval. For instance, two or more adjacent water polygons detected as separate features in the high-resolution image (SPOT) can be merged together and extracted as one polygon in the RADARSAT-2 image. Although the TOPAZ-masking approach can refine this classification allocation problem for all area intervals, it can only mask those areas initially detected by the RADARSAT-2 thresholding image. In general, the graph illustrates that all area intervals follow the same frequency distribution pattern as the histogram depicting the number of detected ponds (Figure 3.12).

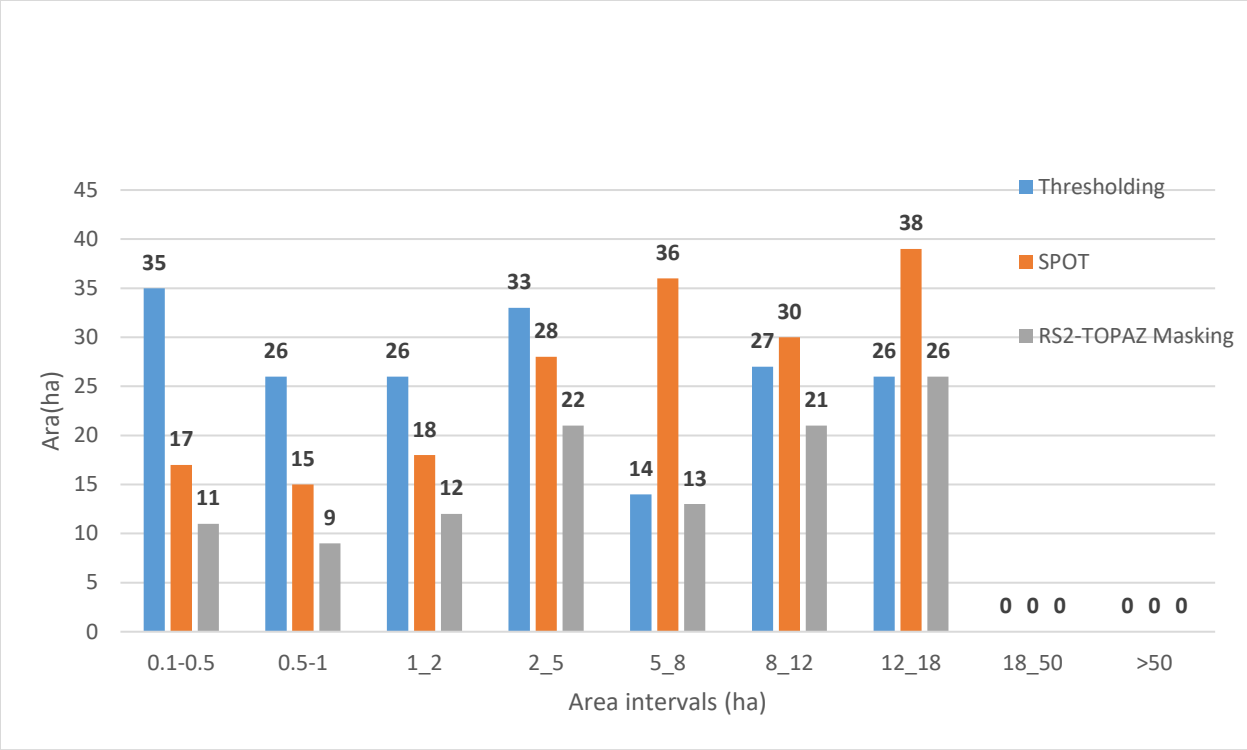

Figure 3.12. Frequency distribution histogram of surface water area mapped in RS-2 Wide mode, SPOT, and TOPAZ masking in different area intervals; the TOPAZ masking reduced the misclassified surface water area in the thresholding image.

3.4.3 RADARSAT-2 (S3) surface water frequency distribution analysis

The low-terrain landscape, low-spatial resolution of Standard mode (30m), and the acquisition time of RADARSAT-2 data in October 2008 (a relatively dry month) over Smith Creek basin resulted in missing a large number of surface water bodies in the thresholding method for the area interval less than 1ha. The amount of detected surface water in the thresholding image was dramatically smaller than the number of ponds discriminated by the SPOT-5 image. In the first area interval (0.1-0.5ha), 58% of detected surface water bodies were missed in the RADARSAT-2 S3 thresholding image when it was compared to the SPOT-5 image, and consequently, the result of the TOPAZ-masked image were affected (Figure 3.13). The RADARSAT-2 (S3) resolution (30m) could be a crucial factor in missing surface water areas in the first area interval.

Because the depression separation was not distinct, the RADARSAT-2 S3 image was not able to discriminate small water polygons as separate objects in the Smith Creek basin. However, in the RADARSAT-2 (S3) image, small ponds may join together and form one bigger polygon, which may be allocated to other surface water area intervals. From the total number of 3474 detected surface water bodies in the S3 mode thresholding image, 2149 ponds were eliminated from the RADARSAT-2 (S3) thresholding image by TOPAZ masking. The RADARSAT-2 beam mode resolution can affect the frequency distribution histogram in coarser RADARSAT-2 resolution beam modes and decrease the accuracy of classification.

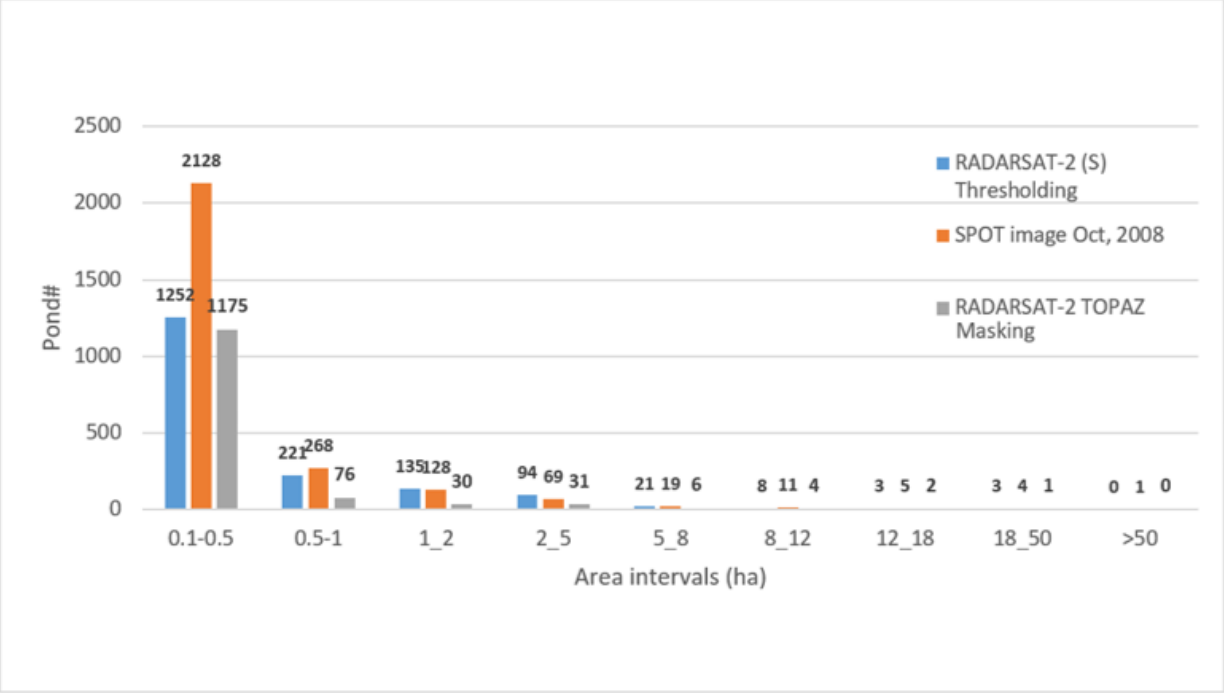

Figure 3.13. Frequency distribution histogram of surface water ponds detected by RADARSAT-2 S3 mode thresholding, TOPAZ masking, and a SPOT image in different area intervals, Smith Creek basin.

To help compare RADARSAT-2 surface water (S3) thresholding, the TOPAZ-masked image and SPOT-5 data, a frequency distribution histogram of detected surface water areas was computed for each area interval (Figure 3.14). The frequency distribution histogram of surface water area shows the influence of the TOPAZ-masking image on the RADARSAT-2 (S3) thresholding image in surface water area intervals. From the total of 1192ha of surface water area detected in the thresholding image, TOPAZ masking removed 724ha of surface water area from the RADARSAT-2 (S3) thresholding image. For the surface water area interval larger than 50ha, RADARSAT-2 (S3) thresholding failed to map surface water areas, in comparison with SPOT-5 data.

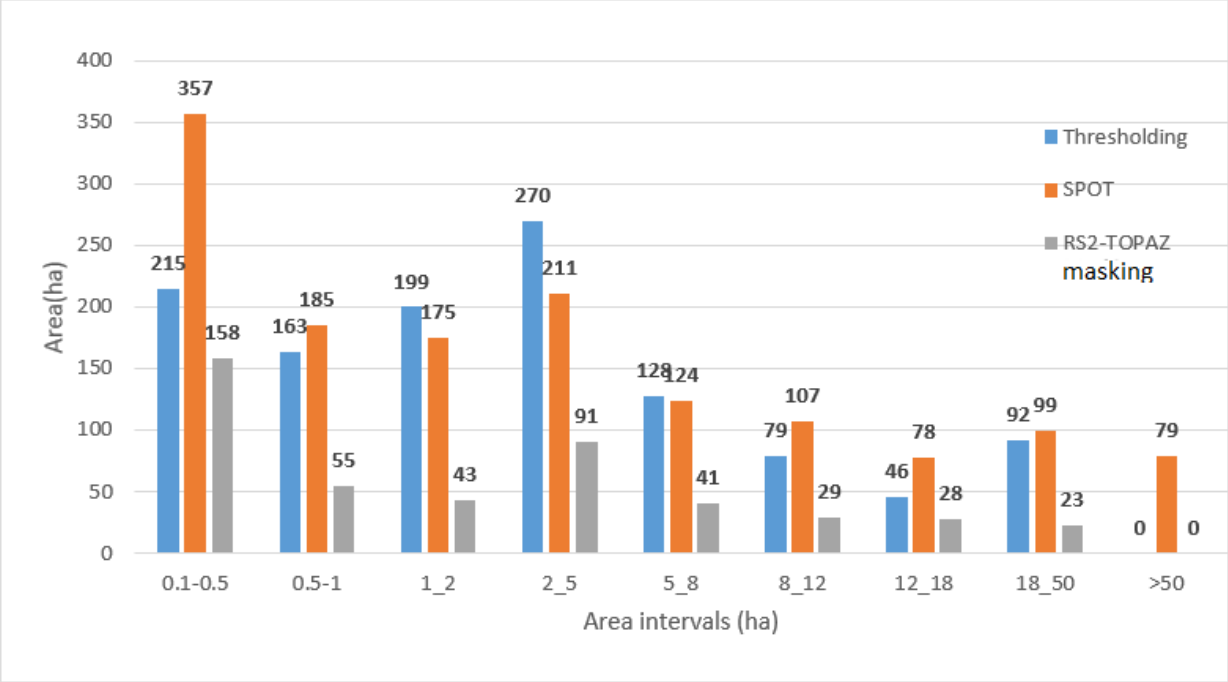

Figure 3.14. Frequency distribution histogram of surface water area detected in RS-2 Standard mode (S3), SPOT, and TOPAZ masking in different area intervals; TOPAZ masking eliminates false classified surface water areas from the thresholding image.

The selection of a suitable beam mode is unique to each project, and the user must consider the study objectives and the tradeoffs of resolution versus swath coverage. In this study, RADARSAT-2 F0W3, W2, and S3 modes were used for surface water mapping activities over PPR. To illustrate the effect of resolution on surface water mapping, all beam modes were examined for the St. Denis and Smith Creek basins. However, to compare landscapes effects, the W2 beam mode (St. Denis) and S3 beam mode (SCRB) with the same spatial resolution offered the best selection of available datasets. The results show that RADARSAT-2 thresholding and the TOPAZ-masking method can detect surface water in all beam modes. However, mapping small surface water areas in the RADARSAT-2 (S3) mode failed in area intervals less than 1ha.

Previous studies have suggested that traditional methods to assess accuracy based on random points and an error matrix cannot adequately evaluate the success of surface water mapping for different beam modes (Bolanos et al., 2016). In Bolanos et al., (2016), a number of randomly stratified points were assigned on a RADARSAT-2 image (50% of them on water pixels and 50% on non-water pixels), and an error matrix was calculated using RADARSAT-2 and SPOT image pairs to assess the classification accuracy. Results showed that, using the random point method, small water bodies in RADARSAT-2 images were hardly distinguishable, whereas large surface water bodies were more recognizable and received more random points. Therefore, to quantify an entire surface water area for operational purposes, better indications of accuracy are required. In the current study, the intersection of the RADARSAT-2 surface water thresholding map and SPOT surface water map approach were used to extract the area common to all image pairs. Then, to calculate the mapping accuracy of surface water, the common areas were compared to each SPOT image. The research hypothesis was confirmed as confining the surface water area to surface depressions (TOPAZ-masked image) would enhance the overall accuracy of all beam

modes. The surface water over PPR is highly variable, especially during the spring and summer seasons. Because evaporation rates are high in the summer, small surface water bodies tend to rapidly disappear. These rapid changes to the surface water in PPR meant that it was not feasible to do fieldwork coincidently with the Remote sensing data acquisition time. Therefore, a number of available high-resolution SPOT images were used as reference data to validate RADARSAT-2 surface water thresholding images and TOPAZ-masking classification results.

3.5 The effects of RADARSAT-2 sensor parameters and surface specific properties

3.5.1 RADARSAT-2 system parameter effects

This study describes the evaluation results of RADARSAT-2 products from different beam modes used to delineate open surface water in St. Denis and Smith Creek research basins. RADARSAT-2 imaging characteristics include nominal swath widths, sensor parameters, and a specific set of available beams at specific incident angles. In this study, the effects of RADARSAT-2 sensor parameters and ground surface characteristic were investigated to determine their ability to accurately delineate surface water. As discussed earlier, the accuracy of surface water classification can be influenced by a number of essential factors, including the seasonal timing of image acquisition, the numbers of the RADARSAT-2 looks, soil moisture, landscape roughness, vegetation cover, and the structure/composition of the ground features (White et la., 2015; Martinis, 2010). The contrast between waterbodies and their surrounding land is also highly affected by the roughness of water surfaces and RADAR parameters, including beam mode resolution, incidence angle, instrument noise level and polarization choice (Martinis, 2010). A selection of three RADARSAT-2 beam mode HH polarization images and a Single Look Complex (SLC) with large spatial coverage and an incident angle range of 30-45º, were used to

examine their ability to detect surface water in St. the Denis and Smith Creek basins, SK. Some of the most significant RADARSAT-2 beam mode parameters and the effects of landscape specific properties on mapping surface waterbodies are discussed below.

3.5.2 RADARSAT-2 Polarization and incidence angle effect

The backscatter of surface water bodies behaves differently depending on parameters such as incidence angle and polarization. The incidence angle describes the angle between the incident RADAR signal beam and the axis perpendicular to the local geodetic ground surface. The term local incidence angle is used to describe the angle between the RADAR beam and the surface at the point of incidence. Since the local incidence angle depends on the incidence angle as well as on the orientation and slope of the illuminated area, it is both a system and an object-specific parameter. The incidence angle has been demonstrated to have significant impacts on RADAR backscatters from different ground surfaces (Ulaby, 1978). The incidence and local incidence angle are only equal for flat terrain and differ substantially from each other in hilly or mountainous regions. The grey contrast between surface water and land in a SAR image decreases with a decreasing incidence angle (Martinis, 2010; Li and Wang, 2015), which suggests that a higher incidence angle in SAR data is preferable for accurately extracting surface water areas. O'Grady et al. (2013) concluded that, given the varying noise levels of the scene, the backscatter varies based on the incidence angle. This requirement considerably reduces the proportion of SAR data suitable for surface water detection (Solbo et al., 2003). Previous studies have also shown that in relatively low-topography landscapes with typically less than a 10% slope gradient, the backscatter coefficient variations from the local incidence angle are negligible (Gala and Melesse, 2012).

Thus, because the terrain in our study areas is flat, the possible effects of topographic relief and changes in the local incidence angle could be minimal.

Flooded vegetation areas can produce high backscatter on the incidence angle imagery due to the signal double-bounce effect. Since smaller incidence angles can penetrate vegetation, they can better detect flooded vegetation (Töyrä et al., 2001). Increases in the incidence angle have been uniformly found to decrease RADAR backscatter from vegetation (Floyd et al., 2008). Thus, a selection of steep incidence angles to detect flooded vegetation and large incidence angles to delineate the open water-land interface is recommended and agrees with earlier work by Töyrä et al., 2001 and Töyrä and Pietroniro (2005). The Fine Wide mode (F0W3) can offer a slightly larger incidence angle among other commonly used beam modes, and this larger angle might lead to better discrimination of water and land. However, because of the low-relief terrain landscape in PPR, especially in the Smith Creek basin, the incidence angle effect could be minimal and can possibly be ignored.

3.5.3 The Noise-Equivalent Sigma-Zero (NESZ) and the Block Adaptive Quantization effect

Actual noise levels of a RADARSAT-2 image depend on many key factors affecting radiometric corrections during processing. Noise-Equivalent Sigma-Zero (NESZ) is a measure of the sensitivity of the RADAR to areas of low backscatter. Any features with backscatter lower than this level may be difficult to recognize in the image. Wide beam modes with Fine resolution (such as F0W3) are achieved by increasing NESZ, which, to maintain a constant resolution, regulates the minimum signal that a RADAR can measure. The NESZ level varies across the swath for any beam and is lower (i.e., better) near the middle. A drawback of using Fine W2 mode (F0W3) for water mapping from the RADAR is that the beam mode used for water mapping is

severely affected by the noise of the scene (MDA, 2016). Appendix C provides the estimated variations of NESZ for each swath position of each beam mode.

During RADARSAT-2 data acquisition, the signals are digitized using eight-bit analog to-digital converters followed by Block Adaptive Quantization (BAQ) coding. BAQ is a data compression technique based on the principles of minimum mean-squared error quantization. The BAQ coding reduces onboard data storage and downlink rates and is capable of using from one- to four-bit representation for the complex SAR data sample (Brisco et al., 2015). During ground processing, the encoded samples are then decoded back to eight-bit representation with some information loss (MDA, 2016). Most of the RADARSAT-2 beam modes use three-bit BAQ, but the wider swaths of some modes use two-bit BAQ to accommodate larger data sets. In particular, the F0W3, W2, and S3 modes use this three-bit BAQ for data downloads.

In the current study, the RADARSAT-2 system parameters were evaluated in different beam modes to delineate surface water over PPR (Table 3.5). HH polarization was the only polarization used for all three beam modes and is preferred for several reasons: it distinguishes surface water from non-water areas; it provides a lower backscatter to wind-induced surface roughness on open water; and it successfully discriminates land and water in the mapping of open surface water areas (Martinis et al., 2009; Gan et al., 2012; Brisco et al., 2008). The NESZ of the three beam modes were obtained and compared. It was shown that NESZ in F0W3 mode is slightly larger than that in the other beam modes, which can increase the noise of the RADARSAT-2 scene. The SAR compression technique (BAQ) was used at the same level (three-bit BAQ) for all three beam modes in the study. Based on the evaluation of the specifications of various beam modes, the nominal resolution effect could be the primary factor directly influencing the accuracy of surface water mapping. Regarding RADARSAT-2 sensor's ability to detect surface water bodies,

there were very little differences between RADARSAT-2 beam mode parameters, including processing level (SLC), product type, polarization, BAQ level, and the number of looks (1x1). Thus, except for the resolution of the beam modes, the sensor modes provided reasonably similar characteristics. It can be therefore concluded that, based on the evaluation of various beam mode specifications, the nominal resolution effect is the essential factor directly influencing the accuracy of surface water mapping.

Table 3.5. RADARSAT-2 sensor parameters for various beam modes (MDA, 2016).

SAR system	Beam mode	Polari-zation	Incidence angle (Degs)	NESZ (dB)	BAQ level (bits)	Product type (number of looks)	Nominal resolution (m)	Spatial coverage (Km), site
RS-2	F0W3	HH	39-45	-24	3	SLC (1x1)	8	150 St. Denis
RS-2	W2	HH	30-39	-28	3	SLC (1x1)	27	150 St. Denis
RS-2	S3	HH	30-37	-29	3	SLC (1x1)	27	100 Smith Creek

3.5.4 The Effects of landscape-specific properties

As indicated, apart from RADAR system parameters and beam mode selections, other factors, such as landscape type, size of potholes, and image acquisition time can also affect the surface water mapping accuracy in the RADARSAT-2 images.

3.5.4.1 Landscape effect

Landscape effects can consist of a number of natural or man-made features of basins, such as surface topography, slope angle, dominant land use/cover, drainage network and dominant depressions size. The landscape type used in this research applies a general concept of the topographic and physiographic characteristics of a land surface and is not consistent with the

classifications of a soil scientist or a geomorphologist. Different beam modes with the same nominal spatial resolution (W2 and S3) were used in different landscape types to evaluate the landscape effect on delineating open surface water areas. The W2 and S3 beam modes were comparable and used to detect surface water over St. Denis and Smith Creek basins, respectively. Initial thresholding results show better accuracy of surface water classification when W2 beam mode was used over St. Denis basin (accuracy=47%).

The topography of the Smith Creek research basin is relatively flat with a slope of 2-5%. The landscape is dominated by many small, shallow isolated depressions with dramatic water level fluctuations and no apparent natural outlet in the basin. The main land use is agriculture, and the basin is widely artificially drained by the local farmers. When the S3 beam mode was used to detect the surface water areas across the Smith Creek basin, the numerous small, shallow depressions were missing. The St. Denis basin represents a different type of PPR landscape. The rolling knob terrain with a slope of 10-15% illustrates a higher topographic relief than that of Smith Creek basin. About one-third of the St. Denis basin was converted to natural grassland in the mid-1980s, and agriculture has little influence on the land cover. The basin is dominated by several small and large isolated surface depressions (Minke et al., 2009). Obtaining satisfactory results was more difficult in Smith Creek basin's flat terrain with its small, shallow depressions than it was in the more rolling terrain and well-defined depressions of the St. Denis basin.

3.5.4.2 The effect of pothole size

To compare surface water detection in two different landscapes, our study delineated surface water based on area intervals and pothole size. Because it has so many small, shallow depressions, Smith Creek research basin can hold a high percentage of surface water in smaller area intervals

(<1-2ha). In the RADARSAT-2 Standard beam mode (S3), most of these small, ephemeral ponds and shallow depressions were missing, suggesting that this method had low accuracy in mapping surface water over Smith Creek basin. However, when compared to SPOT optical imagery of a nearly equivalent spatial resolution, the S3 method succeeded in mapping small water bodies from the Fine Wide beam mode (F0W3).

3.5.4.3 Time of image acquisition effect (wet versus dry conditions)

As indicated earlier, RADARSAT-2 acquisition time is another critical factor to be considered in any surface water mapping studies. The S3 beam mode was acquired in October 2008, a fairly dry year, and was the only available data used for delineating surface water over Smith Creek study basin. During a dry year or in a higher temperature, a large number of small ponds are susceptible to disappearing because the minimal water that supplied them in the spring evaporates in the summer. The W2 beam mode image was acquired in August 2008, which was the same year the S3 image was acquired. The F0W3 image was acquired in June 2014, a comparably wet year during which numerous small water bodies were mapped over St. Denis basin. The lack of many small surface water areas in W2 mode data suggests that RADARSAT-2 sensors would have easily detected the large open water bodies (homogenous pixels) if the W2 image acquisition time had been used.

3.5.4.4 The shape effects of potholes

The dominant shape of depressions and their spatial distribution in Smith Creek basin is quite different from those of St. Denis basin. The shape is a basic concept of features, but because surface depressions have more complex shapes than circles, triangles, and rectangles, it is difficult to quantify and measure them. In general, it has not yet been shown that the shape of surface depressions can affect the mapping accuracy of surface water bodies. The most commonly measured characteristic of shape is compactness, a measure of how far a shape deviates from a circle (the most compact possible shape). Pounds (1963) suggested that a measurement of compactness would be the ratio of the length of the perimeter of a shape to its area. Measuring the length of the boundary (perimeter) is quite difficult due to irregular surface water ponds. It was visually observed that RADARSAT-2 can detect most of the surface water bodies with a high compactness (which tend to be circular) in study areas.

Chapter 4

Conclusion

Surface water storage in the Prairie Pothole Region (PPR) is linked to significant issues, such as climate change, water quality, hydrological cycles, wildlife habitat, regional and global environments. Surface water bodies are essential to maintaining a balanced hydrological system and environment health, and their monitoring is vital for a variety of reasons, including a better understanding of hydrological and climate modeling (Belair et al., 2015). By helping to identify, delineate, and characterize surface water, remote sensing images can support conservation and management of PPR ecosystems. RADARSTAT-2 is an earth-observation satellite imagery implemented in 2007 for the Canadian Space Station. This satellite is capable of mapping surface water in a variety of weather and surface roughness conditions at regular and frequent time intervals. However, despite being an efficient and inexpensive method, threshold-based surface water mapping from RADARSTAT-2 imagery misclassifies large amounts of land pixels as water, and previous studies have suggested that high soil moisture content could be the primary source of this inaccuracy. This research seeks to address these problems and contribute to a new framework for monitoring surface water area for hydrologic analysis and climate modeling. In this study, a threshold-based method for operational use of RADARSAT-2 data for surface water mapping and monitoring has been investigated in two specified areas of interest over the Canadian PPR. A post-thresholding TOPAZ masking method was applied to remove misclassified areas. In this procedure, high-resolution LiDAR-based DEM data and TOPAZ were manipulated to delineate the maximum extent of surface depressions to use as a mask for the RADARSAT-2 thresholding image. The maximum depression extent, produced by the TOPAZ, was applied to remove all the false polygons generated by the thresholding method on the RADARSAT-2 image.

The new RADARSAT-2 TOPAZ masking method introduced in this study has contributed to efforts to improve the accuracy of surface water mapping for PPR studies and applications.

When surface water information needs to be extracted to use in weather and climate prediction models, RADARSAT-2 processing time is a key factor due to rapid temporal changes in the extent of surface water. RADARSAT-2 thresholding together with the TOPAZ-masking method provides a fast execution and requires minimal computational effort. These advantages mean that this process can be easily implemented to derive key data on water bodies from a RADARSAT-2 image in near-real time. The proposed approach was applied on Wide Fine (F0W3), Wide (W2) and Standard (S3) data to examine both RADARSAT-2 beam mode resolution and landscape effects for surface water mapping over the St. Denis and Smith Creek basins in Saskatchewan, Canada. The acquisition time of different images, as well as the effects of RADARSAT-2 sensor characteristics, were also evaluated for both study sites.

The results showed that similar RADARSAT-2 image resolution produced different classification accuracy results. Thus, different factors such as RADARSAT-2 sensor parameters and surface specific characteristics were investigated to better understand the effect of these factors on surface water mapping results. The RADARSAT-2 F0W3 beam mode produced a higher classification accuracy for the water pixels than the W2 and S3 modes. For overall surface water delineation, the TOPAZ-masked images showed higher surface water classification accuracy and lower classification errors than the commonly used thresholding method. A more satisfactory result was generated when RADARSAT-2 Fine Wide beam mode with HH polarization was applied. The RADARSAT-2 Fine Wide mode (F0W3) shows that it can be efficiently implemented as an operational scheme for mapping waterbodies in near-real-time.

4.1 Main Findings

The main achievement of this study was the development of quantification accuracy for open surface water monitoring using RADARSAT-2 data within the PPR. To evaluate the accuracy of the method, the results of the RADARSAT-2 thresholding and TOPAZ masking images were compared to coincidently taken high-resolution SPOT data.

The main findings of the research were as follow:

1) The RADARSAT-2 F0W3 mode (8m) and TOPAZ masking method provided 81% of the total water area in the St. Denis basin extracted from the SPOT image. The procedure succeeded in detecting small surface water area intervals of less than 1ha in the research basin.

2) The RADARSAT-2 W2 modes (30m) and TOPAZ masking approach captured 75% of the total surface water areas in St. Denis basin extracted from the SPOT image.

3) The RADARSAT-2 Standard mode (30m) and TOPAZ masking method detected 48% of the total surface water areas in Smith Creek basin extracted from the SPOT image. A large number of small isolated ponds were not detected in very low relief terrain in Smith Creek basin.

4) The frequency distribution histogram of potholes showed that when compared to a time-concurrent SPOT image, the number of ponds in small intervals (0.1-2ha) was overestimated in St. Denis basin and underestimated in Smith Creek basin.

5) The TOPAZ-masking approach demonstrated that it can be used as a robust procedure to enhance the accuracy of surface water classification in RADARSAT-2 thresholding images.

6) The combination of the RADARSAT-2 F0W3 with HH polarization and TOPAZ masking data gave the best surface water mapping results among other examined beam modes in this research. Thus, the F0W3 mode may provide the best trade-off in area coverage versus data quality for operational surface water monitoring applications.

7) The different levels of accuracy obtained from different beam modes and different landscapes indicate that the RADARSAT-2 surface water mapping results can be affected by various factors, such as image acquisition time, SAR sensor parameters, and surface specific properties in the PPR.

The results showed that the beam mode resolution and the landscape effects were two essential factors in the delineation of surface waterbodies when the other RADARSAT-2 sensor parameters remained the same.

The combination of Fine Wide (F0W3) mode imagery and the TOPAZ-masked approach seems to provide the best surface water classification results, as, compared to surface water maps extracted from multi-spectral high-resolution SPOT images in St. Denis basin, it estimated 81% of the total surface water area. However, the same results might not be achieved in terrains different from our study basins or in a different climatological year.

The expected benefits of the thesis are as follows:

1. Improved and more rapid water body assessment, which can easily be integrated into local and national planning processes;

2. Assistance in the further development of weather-prediction models and freshwater applications in supporting water resource management

3. Contributions to the understanding of the theories and techniques of the hydrology and the hydrodynamic and hydrologic controls of the PPR.

4. A novel, yet simple, fast and practical technique for mapping and monitoring surface hydrology in the PPR landscape.

4.2 Limitations and further research

The recent advances in the technology of RADAR systems needs to be accompanied by studies that demonstrate applications in exploiting RADAR's capabilities and directing future RADAR development, particularly in the field of surface water mapping. This study could not test the RADARSAT-2 F0W3 mode image for Smith Creek study basin as the F0W3 image was not available for that region. Because the RADARSAT-2 F0W3 mode image achieved high surface water accuracy in St. Denis basin (81%), it is recommended the same technology be applied and tested on some low-relief landscapes, such as the Smith Creek basin in the post-snowmelt period.

The combination of RADAR, optical, and high-resolution topographic data, such as LiDAR-based DEM, is necessary to improve assessment of PPR functionalities, particularly for hydrologic processes. The RADARSAT-2 TOPAZ masking technique shows a promise in for operational mapping of surface water in PPR. However, due to water and land edge pixels, the post-threshold TOPAZ masking does not remove all errors. Thus, some false targets still exist and need to be removed. Manual editing can easily be handled by the end user in a GIS software using ground truth data, and knowledge of the area of interest can be used to improve the classification results, as well as to remove the remaining false targets. To facilitate and improve monitoring in an operational mode, the human work now involved with determining the thresholding value can be taken over by an automated mathematical algorithm.

To enumerate weather and predict the climate, flooded vegetation areas are as significant as open surface water areas. Single polarization RADARSAT-2 was not as efficient in mapping flooded vegetation because the RADAR backscatter could not be decomposed with only one intensity channel (HH). However, when polarimetric decompositions are applied, using fully polarimetric SAR, features like flooded vegetation can be identified and classified. Further work

is required to accurately map flooded vegetation areas that might be simply categorized as non-water areas in the thresholding method. The upcoming RADAR Constellation Mission (RCM) will offer compact polarimetry, meaning that polarimetric data will be more easily obtained in wider areas with higher resolution than it was the RADARSAT-2 (Vachon et al., 2012). RCM will also have a better temporal resolution (four days) compared to RADARSAT-2.

Despite the advantages of using RADARSAT-2 images for mapping surface water resources, there were some limitations. It was challenging to find comparable beam modes for different areas at different times. Because of the dynamic nature of the constantly changing environment of PPR and the acquisition times of different beam modes, the results of the RADARSAT-2 resolution mode effect are confounded by various climate and hydrological conditions. Therefore, the application of the same RADARSAT-2 resolution mode in similar climatological years could better demonstrate the effect of the resolution of the beam modes resolution and help improve surface water classification results. Thus, a consistent sensor mode needs to be available for obtaining images across the PPR for operational surface water mapping purposes.

The TOPAZ software has been shown to be reliable, robust, and fast. However, the accuracy of masking depressions with TOPAZ is highly dependent on the quality of topographic data (DEM). Various approaches can be used for masking based on the surface depression filling. To determine the maximum possible surface depression, this study used detailed, high-resolution LiDAR-based DEM data as input for TOPAZ. Thus, if the topographic data is high quality, masking results can be sufficiently reliable to develop RADARSAT-2 surface water classification results. It is important to note that the ideal conditions for LiDAR data collection are leaf-off and dry antecedent conditions for surface depression analyses. As LiDAR-based DEM data may not

be widely available throughout the PPR, future research could focus on the development of a novel remote sensing technique to accurately extract the extent of surface water from high-resolution cloud-free optical image data. To apply a high-resolution, optical cloud-free image as a mask image, the data must be acquired in the wettest hydrologic period. This condition is required to demonstrate the maximum extent of surface water in depressional surface storage.

The St. Denis study basin recorded the best surface water classification result using the F0W3 mode with HH polarization. To frequently monitor the status of surface water bodies and capture the dynamic seasonal and annual changes, the F0W3 beam model with one common masking scheme is thus recommended for application across the PPR. According to the study results, the following research is recommended for future studies:

1. Using a consistent imaging mode across the PPR to obtain comparable results with the Fine Wide beam mode (F0W3) and HH Polarization to map surface water areas and;
2. Using compact (fully) polarimetric images with wide swath coverage to detect flooded vegetation areas;
3. Comparing RADARSAT-2 data from two climatologically similar years with a consistent imaging mode to better isolate the effect of resolution on detecting surface water.

Chapter 5

References

Ahtonen, P., Euro, M., Hallikainen, M., Solbø, S., Johansen, B. and Solheim, I., 2004. SAR and optical based algorithms for estimation of water bodies. Technical report, Flood Man Project.

Ahtonen, P. and Hallikainen, M., 2005, July. Automatic detection of water bodies from spaceborne SAR images. In IGARSS (Vol. 5, pp. 25-29).

Akinremi, O.O., McGinn, S.M. and Cutforth, H.W., 2001. Seasonal and spatial patterns of rainfall trends on the Canadian prairies. Journal of Climate, 14(9), pp.2177-2182.

Al-Bayati, M. and El-Zaart, A., 2013, November. Automatic thresholding techniques for SAR images. In Proceedings of the International Conference of Soft Computing, Dubai, United Arab Emirates (pp. 18-19).

Alifu, H., Tateishi, R. and Johnson, B., 2015. A new band ratio technique for mapping debris-covered glaciers using Landsat imagery and a digital elevation model. International Journal of Remote Sensing, 36(8), pp.2063-2075.

Armstrong, R. L., and E. Brun, Eds., 2008: Snow and Climate: Physical Processes, Surface Energy Exchange and Modeling. Cambridge University Press, 222 pp.

Baker, C., Lawrence, R., Montagne, C. and Patten, D., 2006. Mapping wetlands and riparian areas using Landsat ETM+ imagery and decision-tree-based models. Wetlands, 26(2), pp.465-474.

Bartsch, A., Trofaier, A.M., Hayman, G., Sabel, D., Schlaffer, S., Clark, D.B. and Blyth, E., 2012. Detection of open water dynamics with ENVISAT ASAR in support of land surface modelling at high latitudes. Biogeosciences, 9(2), pp.703-714.

BAGHDADI, N., BERNIER, M., GAUTHIER, R. and NEESON, I., 2001, Evaluation of C-band SAR data for wetlands mapping. International Journal of Remote Sensing, 22, pp. 71–88.

Billa, L. and Pradhan, B., 2011. Semi-automated procedures for shoreline extraction using single RADARSAT-1 SAR image. Estuarine, Coastal and Shelf Science, 95(4), pp.395-400.

Brinson, M.M. 1993. “Gradients in the Functioning of Wetlands along Environmental Gradients.” Wetlands 13:65-74.

Bonsal, b.r.; x. zhang and w.d. hogg. 1999. Canadian Prairie growing season precipitation variability and associated atmospheric circulation. Clim. Res. 11: 191–208.

Bonsal, B.R., Aider, R., Gachon, P. and Lapp, S., 2013. An assessment of Canadian prairie drought: past, present, and future. Climate Dynamics, 41(2), pp.501-516.

Brisco, B., Kapfer, M., Hirose, T., Tedford, B. and Liu, J., 2011. Evaluation of C-band polarization diversity and polarimetry for wetland mapping. Canadian Journal of Remote Sensing, 37(1), pp.82-92.

Brisco, B., Touzi, R., van der Sanden, J.J., Charbonneau, F., Pultz, T.J. and D'Iorio, M., 2008. Water resource applications with RADARSAT-2–a preview. International Journal of Digital Earth, 1(1), pp.130-147.

Brisco, B., Short, N., Sanden, J.V.D., Landry, R. and Raymond, D., 2009. A semi-automated tool for surface water mapping with RADARSAT-1. Canadian Journal of Remote Sensing, 35(4), pp.336-344.

Brisco, B., Li, K., Tedford, B., Charbonneau, F., Yun, S. and Murnaghan, K., 2013. Compact polarimetry assessment for rice and wetland mapping. International journal of remote sensing, 34(6), pp.1949-1964.

Brivio, P.A., Colombo, R., Maggi, M. and Tomasoni, R., 2002. Integration of remote sensing data and GIS for accurate mapping of flooded areas. International Journal of Remote Sensing, 23(3), pp.429-441.

Bolanos, S., Stiff, D., Brisco, B. and Pietroniro, A., 2016. Operational surface water detection and monitoring using Radarsat 2. Remote Sensing, 8(4), p.285.

Brannen, R., Spence, C. and Ireson, A., 2015. Influence of shallow groundwater–surface water interactions on the hydrological connectivity and water budget of a wetland complex. Hydrological Processes, 29(18), pp.3862-3877.

Blaschke, T., Burnett, C. and Pekkarinen, A., 2004. Image segmentation methods for object-based analysis and classification. In Remote sensing image analysis: Including the spatial domain (pp. 211-236). Springer Netherlands.

Burn, D.H., 2008. Climatic influences on streamflow timing in the headwaters of the Mackenzie River Basin. Journal of Hydrology, 352(1-2), pp.225-238.

Canadian Centre for Remote Sensing (CCRS). 2008, Radar Polarimetry, Natural Resources Canada, Accessed May 2012: http://www.nrcan.gc.ca/earth-sciences/geographyboundary/remote-sensing/fundamentals/1025.

Canadian Centre for Remote Sensing (CCRS). N.d, Radar Polarimetry, Advanced Radar Polarimetry Tutorial, Accessed May 2012: http://www.nrcan.gc.ca/earthsciences/geography-boundary/remote-sensing/radar/1893.

Campos, J. C., N. Sillero, and J. C. Brito. 2012. “Normalized Difference Water Indexes Have Dissimilar Performances in Detecting Seasonal and Permanent Water in the Sahara-Sahel Transition Zone.” Journal of Hydrology 464-465: 438–446. doi:10.1016/j.jhydrol.2012.07.042.

Campbell, J.B. and Wynne, R.H., 2011. Introduction to remote sensing. Guilford Press.

Chan, Y.K. and Koo, V.C., 2008. An introduction to synthetic aperture radar (SAR). Progress In Electromagnetics Research, 2, pp.27-60.

Chen, L.C. and Shyu, C.C., 1998. Automated extraction of shorelines from optical and SAR images. In Proceeding of the 19th. Asian Conference on Remote Sensing, Manila, Philipine, Available on: http://www. Gis development. net/aars/acrs.

Conley, F. M. and G. van der Kamp. 2001. Monitoring the hydrology of Canadian prairie wetlands to detect the effects of climate change and land use changes. Environmental Monitoring and Assessment 67:195–215

Coppin, P., Jonckheere, I., Nackaerts, K., Muys, B. and Lambin, E., 2004. Review ArticleDigital change detection methods in ecosystem monitoring: a review. International journal of remote sensing, 25(9), pp.1565-1596.

CONGALTON, R. G., and PLOURDE, L., 2002, Quality assurance and accuracy assessment of information derived from remotely sensed data. In Manual of Geospatial Science and Technology, edited by J. Bossler (London: Taylor & Francis), pp. 349–361.

Clark, R.B., Creed, I.F., Sass, G.Z., 2009. Mapping hydrologically sensitive areas on the Boreal Plain: a multi temporal analysis of ERS synthetic aperture radar data. International Journal of Remote Sensing 30 (10), 2619–2635.

Di Baldassarre, G., Schumann, G., Brandimarte, L. and Bates, P., 2011. Timely low resolution SAR imagery to support floodplain modelling: a case study review. Surveys in geophysics, 32(3), pp.255-269.

Doxaran, D., Froidefond, J.M., Lavender, S.J., Castaing, P., 2002. Spectral signature of highly turbid waters application with SPOT data to quantify suspended particulate matter concentrations. Remote Sensing of Environment 81 (1), 149–161

Du, Z., Bin, L., Ling, F., Li, W., Tian, W., Wang, H., Gui, Y., Sun, B. and Zhang, X., 2012. Estimating surface water area changes using time-series Landsat data in the Qingjiang River Basin, China. Journal of Applied Remote Sensing, 6(1), p.063609.

Dumanski, S., Pomeroy, J.W. and Westbrook, C.J., 2015. Hydrological regime changes in a Canadian Prairie basin. Hydrological Processes, 29(18), pp.3893-3904.

Essery, R., Li, L., & Pomeroy, J. (1999). A distributed model of blowing snow over complex terrain. Hydrological Processes, 13, 2423−2438.

Fairfield, J., P. Leymarie, Drainage networks from grid digital elevation models, Water Resour. Res., 275, 709–717, 1991.

Fang, X., Minke, A., Pomeroy, J., Brown, T., Westbrook, C., Guo, X. and Guangul, S., 2007. A review of Canadian Prairie hydrology: Principles, modelling and response to land use and drainage change. Center for Hydrology, University of Saskatchewan.

Fang X, Pomeroy JW. 2007. Snowmelt runoff sensitivity analysis to drought on the Canadian prairies. Hydrological Processes 21(19): 2594–2609. DOI: 10.1002/hyp.6796.

Fang and Pomeroy, 2008 X. Fang, J.W. Pomeroy Drought impacts on Canadian prairie wetland snow hydrology Hydrological Processes, 22 (15) (2008), pp. 2858-2873

Fan, J.L. and Lei, B., 2012. A modified valley-emphasis method for automatic thresholding. Pattern Recognition Letters, 33(6), pp.703-708.

Feyisa, G.L., Meilby, H., Fensholt, R. and Proud, S.R., 2014. Automated Water Extraction Index: A new technique for surface water mapping using Landsat imagery. Remote Sensing of Environment, 140, pp.23-35.

Finnigan, C., 2013. Developing a grassland biomass monitoring tool using a time series of dual polarimetric SAR and optical data (Doctoral dissertation).

Frost, V.S., Stiles, J.A., Josephine, A., Shanmugan, K. S., and Holtzman, J.C., 1982. A Model for Radar Images and Its Application to Adaptive Digital Filtering of Multiplicative Noise. IEEE Transactions on Pattern Analysis and Machine Intelligence, Vol. PAMI-4, No. 2, March 1982.

Gagnon, L. and Jouan, A., 1997, October. Speckle filtering of SAR images: a comparative study between complex-wavelet-based and standard filters. In Wavelet Applications in Signal and Image Processing V (Vol. 3169, pp. 80-92). International Society for Optics and Photonics.

Gan, T. Y., Zunic, F., Kuo, C-C., and Strobl, T. 2012. "Flood mapping of Danube River at Romania using single and multi-date ERS2- SAR images." International Journal of Applied Earth Observation Geoinformation, 18, pp. 69–81.

Gala, T.S. and Melesse, A.M., 2012. Monitoring prairie wet area with an integrated LANDSAT ETM+, RADARSAT-1 SAR and ancillary data from LIDAR. Catena, 95, pp.12-23.

Gala, T.S., Aldred, D.A., Carlyle, S. and Creed, I.F., 2011. Topographically based spatially averaging of SAR data improves performance of soil moisture models. Remote sensing of environment, 115(12), pp.3507-3516.

Gan, T. Y., Zunic, F., Kuo, C-C., and Strobl, T. 2012. "Flood mapping of Danube River at Romania using single and multi-date ERS2- SAR images." International Journal of Applied Earth Observation Geoinformation, 18, pp. 69–81.

GARBRECHT, J. and MARTZ, L.W., 1997, The assignment of drainage direction over flat surface in raster digital elevation models. Journal of Hydrology, 193, pp. 204–213.

Garbrecht, J. and Martz, L.W., 1995. An automated digital landscape analysis tool for topographic evaluation, drainage identification, watershed segmentation, and subcatchment parameterization.

GARBRECHT, J. and MARTZ, L.W., 2000, Digital elevation model issues in water resources modeling. In Hydrologic and Hydraulic Modeling Support with Geographic Information Systems, D. Maidment and D. Djokic (Eds), pp. 1–27 (Redland, CA: ESRI Press).

Granger, R.J. and Gray, D.M., 1989. Evaporation from natural nonsaturated surfaces. Journal of Hydrology, 111(1-4), pp.21-29.

Gleason, R.A., Laubhan, M.K., Tangen, B.A. and Kermes, K.E., 2008. Ecosystem services derived from wetland conservation practices in the United States Prairie Pothole Region with an emphasis on the US Department of Agriculture Conservation Reserve and Wetlands Reserve Programs.

Hahmann, T. and Wessel, B., 2010, June. Surface water body detection in high-resolution TerraSAR-X data using active contour models. In Synthetic Aperture Radar (EUSAR), 2010 8th European Conference on (pp. 1-4). VDE.

Hahmann, T., Twele, A., Martinis, S. and Buchroithner, M., 2010. Strategies for the automatic extraction of water bodies from Terra SAR-X/TanDEM-X data. In Geographic Information and Cartography for Risk and Crisis Management (pp. 129-141). Springer Berlin Heidelberg.

Hayashi, M., van der Kamp, G. and Rudolph, D.L., 1998. Water and solute transfer between a prairie wetland and adjacent uplands, 1. Water balance. Journal of Hydrology, 207(1-2), pp.42-55.

Hayashi, M., Van der Kamp, G. and Rudolph, D.L., 1998b. Mass transfer processes between a prairie pothole and adjacent uplands, 2: chloride cycle. J. Hydrol, 207, pp.56-67.

Hayashi M, van der Kamp G and Schmidt R 2003 Focused infiltration of snowmelt water in partially frozen soil under small depressions Journal of Hydrology 270 214–29

Henderson, F.M. and Lewis, A.J., 1998. Principles and applications of imaging radar. Manual of remote sensing: Volume 2.

Henry, J.B., Chastanet, P., Fellah, K. and Desnos, Y.L., 2006. Envisat multi-polarized ASAR data for flood mapping. International Journal of Remote Sensing, 27(10), pp.1921-1929.

Hess, L. L., Melack, J. M., Filoso, S., and Wang, Y. 1995. “Delineation of inundated area and vegetation along the Amazon floodplain with the SIR-C synthetic aperture radar.” IEEE Transactions on Geoscience and Remote Sensing, 33, pp. 896–904.

Hess, L.L., Melack, J.M., Novo, E.M., Barbosa, C.C. and Gastil, M., 2003. Dual-season mapping of wetland inundation and vegetation for the central Amazon basin. Remote sensing of environment, 87(4), pp.404-428.

Hess, L.L., Melack, J.M. and Simonett, D.S., 1990. Radar detection of flooding beneath the forest canopy: a review. International Journal of Remote Sensing, 11(7), pp.1313-1325.

Hess, L.L., Melack, J.M., Affonso, A.G., Barbosa, C., Gastil-Buhl, M. and Novo, E.M., 2015. Wetlands of the lowland Amazon basin: Extent, vegetative cover, and dual-season inundated area as mapped with JERS-1 synthetic aperture radar. Wetlands, 35(4), pp.745-756

Heremans, R., Willekens, A., Borghys, D., Verbeeck, B., Valckenborgh, J., Acheroy, M. and Perneel, C., 2003, November. Automatic detection of flooded areas on ENVISAT/ASAR images using an object-oriented classification technique and an active contour algorithm. In Recent Advances in Space Technologies, 2003. RAST'03. International Conference on. Proceedings of (pp. 311-316). IEEE.

Henry, J.B., Chastanet, P., Fellah, K. and Desnos, Y.L., 2006. Envisat multi-polarized ASAR data for flood mapping. International Journal of Remote Sensing, 27(10), pp.1921-1929.

Hong, S.H., Wdowinski, S., Kim, S.W. and Won, J.S., 2010. Multi-temporal monitoring of wetland water levels in the Florida Everglades using interferometric synthetic aperture radar (InSAR). Remote Sensing of Environment, 114(11), pp.2436-2447.

Huang, S., J. Li, and M. Xu. 2012. "Water Surface Variations Monitoring and Flood Hazard Analysis in Dongting Lake Area Using Long-Term Terra/MODIS Data Time Series." Natural Hazards 62 (1): 93–100. doi:10.1007/s11069-011-9921-6.

Xu, H., 2006. Modification of normalized difference water index (NDWI) to enhance open water features in remotely sensed imagery. International journal of remote sensing, 27(14), pp.3025-3033

Horritt, M.S., Mason, D.C., Cobby, D.M., Davenport, I.J. and Bates, P.D., 2003. Waterline mapping in flooded vegetation from airborne SAR imagery. Remote Sensing of Environment, 85(3), pp.271-281

Höfle, B., Vetter, M., Pfeifer, N., Mandlburger, G. and Stötter, J., 2009. Water surface mapping from airborne laser scanning using signal intensity and elevation data. Earth Surface Processes and Landforms, 34(12), pp.1635-1649

Hubbard, D. E. and R. L. Linder. 1986. Spring runoff retention in prairie pothole wetlands. Journal of Soil and Water Conservation 41:122–125.

Huel, D 2000 Managing Saskatchewan Wetlands ~ landowner's guide Saskatchewan Wetland Conservation Corporation, Regina.

Jain, S.K., Singh, R.D., Jain, M.K. and Lohani, A.K., 2005. Delineation of flood-prone areas using remote sensing techniques. Water Resources Management, 19(4), pp.333-347.

Jain, S.K., Saraf, A.K., Goswami, A. and Ahmad, T., 2006. Flood inundation mapping using NOAA AVHRR data. Water Resources Management, 20(6), pp.949-959.
Ji, L., Zhang, L. and Wylie, B., 2009. Analysis of dynamic thresholds for the normalized difference water index. Photogrammetric Engineering & Remote Sensing, 75(11), pp.1307-1317.

Johnson, W.C., Boettcher, S.E., Poini, K.A., Gutenspergen, G., 2005. Influence of weather extremes on the water levels of glaciated prairie wetlands. Wetlands 24, 385–398.

Lira, J., 2006. Segmentation and morphology of open water bodies from multispectral images. International Journal of Remote Sensing, 27(18), pp.4015-4038.

Ryu, J.H., Won, J.S. and Min, K.D., 2002. Waterline extraction from Landsat TM data in a tidal flat: a case study in Gomso Bay, Korea. Remote Sensing of Environment, 83(3), pp.442-456.

Inglada, J. and Mercier, G., 2007. A new statistical similarity measure for change detection in multi-temporal SAR images and its extension to multiscale change analysis. IEEE transactions on geoscience and remote sensing, 45(5), pp.1432-1445.

Jenson, S.K. and Domingue, J.O., 1988. Extracting topographic structure from digital elevation data for geographic information system analysis. Photogrammetric engineering and remote sensing, 54(11), pp.1593-1600.

Klemas, V. and Pieterse, A., 2015. Using remote sensing to map and monitor water resources in arid and semiarid regions. In Advances in Watershed Science and Assessment (pp. 33-60). Springer International Publishing.

Kerle, N., Janssen, L.L. and Huurneman, G.C., 2004. Principles of remote sensing. ITC, Educational textbook series, 2, p.250.

Kuenzer, C., Guo, H., Huth, J., Leinenkugel, P., Li, X. and Dech, S., 2013. Flood mapping and flood dynamics of the Mekong Delta: ENVISAT-ASAR-WSM based time series analyses. Remote Sensing, 5(2), pp.687-715.

LaBaugh, J.W., Winter, T.C. and Rosenberry, D.O., 1998. Hydrologic functions of prairie wetlands. Great Plains Research, pp.17-37.

Lee, J.S. and Pottier, E., 2009. Polarimetric radar imaging: from basics to applications. CRC press.

Lee, J.S., Grunes, M.R. and Pottier, E., 2001. Quantitative comparison of classification capability: Fully polarimetric versus dual and single-polarization SAR. IEEE Transactions on Geoscience and Remote Sensing, 39(11), pp.2343-2351.

Lee, J.S., 1980. Digital image enhancement and noise filtering by use of local statistics. IEEE transactions on pattern analysis and machine intelligence, (2), pp.165-168.

Lee, J.S., 1981. Speckle Analysis and Smoothing of Synthetic Aperture Radar Images. Computer Graphics and Image Processing, Vol. 17:24-32.

Lee, J. S., 1983. Digital Image Smoothing and the Sigma Filter. Computer Vision, Graphics and Image Processing, 24, 255– 269.

Leibowitz, S.G. and Vining, K.C., 2003. Temporal connectivity in a prairie pothole complex. Wetlands, 23(1), pp.13-25.

Li, J. and Chen, W. 2005: A rule-based method for mapping Canada's wetlands using optical, radar, and DEM data. International Journal of Remote Sensing 26, 5051-69.

Li, J. and Wang, S., 2015. An automatic method for mapping inland surface waterbodies with Radarsat-2 imagery. International Journal of Remote Sensing, 36(5), pp.1367-1384.

Lindsay, J.B., Creed, I.F. and Beall, F.D., 2004. Drainage basin morphometrics for depressional landscapes. Water Resources Research, 40(9).

Lillesand, T., Kiefer, R.W. and Chipman, J., 2014. Remote sensing and image interpretation. John Wiley & Sons.

Lu, J., Giustarini, L., Xiong, B., Zhao, L., Jiang, Y. and Kuang, G., 2014. Automated flood detection with improved robustness and efficiency using multi-temporal SAR data. Remote Sensing Letters, 5(3), pp.240-248.

Lowry, R. T., N. Mudry, and E. J. Langham, 1979. A Preliminary Analysis of SAR Mapping of the Manitoba Flood, May 1979, Satellite Hydrology; Proceedings of the Fifth Annual William T. Pecora Memorial Symposium on Remote Sensing, Sioux Falls, South Dakota.

Long, S., Fatoyinbo, T. E., and Policelli, F. 2014. "Flood extent mapping for Nambia using change detection and thresholding with SAR." Environmental Research Letters, 9, doi:10.1088/1748-9326/9/3/035002

MacDonald Dettwiler and Associates (MDA). 2016. Radarsat-2 Product Description; RN-RP-51–2713; MacDonald Dettwiler and Associates: Richmond, BC, Canada.

Martinis, S., 2010. Automatic near real-time flood detection in high resolution X-band synthetic aperture radar satellite data using context-based classification on irregular graphs (Doctoral dissertation, lmu).

Martinis, S. and Twele, A., 2010. A hierarchical spatio-temporal Markov model for improved flood mapping using multi-temporal X-band SAR data. Remote Sensing, 2(9), pp.2240-2258.

Martinis, S., Twele, A. and Voigt, S., 2009. Towards operational near real-time flood detection using a split-based automatic thresholding procedure on high resolution TerraSAR-X data. Natural Hazards and Earth System Sciences, 9(2), pp.303-314.

Manjusree, P., Kumar, L.P., Bhatt, C.M., Rao, G.S. and Bhanumurthy, V., 2012. Optimization of threshold ranges for rapid flood inundation mapping by evaluating backscatter profiles of high incidence angle SAR images. International Journal of Disaster Risk Science, 3(2), pp.113-122.

Mason, D.C., Horritt, M.S., Dall'Amico, J.T., Scott, T.R. and Bates, P.D., 2007. Improving river flood extent delineation from synthetic aperture radar using airborne laser altimetry. IEEE Transactions on Geoscience and Remote Sensing, 45(12), pp.3932-3943.

Millett, B., Johnson, W.C. and Guntenspergen, G., 2009. Climate trends of the North American prairie pothole region 1906–2000. Climatic Change, 93(1-2), pp.243-267.

Milton, G.R. and Hélie, R., 2003, February. Wetland inventory and monitoring: partnering to provide a national coverage. In Wetland Stewardship in Canada: Contributed Papers from the Conference on Canadian Wetlands Stewardship (pp. 3-5).

Milton, G. et al., 2003. Development of a remote-sensing wetland inventory and classification system for Canada. Back-scatter, 14 (1), Winter 2003. Halifax, Nova Scotia.

McFeeters, S.K., 1996. The use of the Normalized Difference Water Index (NDWI) in the delineation of open water features. International journal of remote sensing, 17(7), pp.1425-1432.

Morena, L.C., et al., 2004, RADARSAT-2 Order handling and mission planning. Canadian journal of remote sensing, 30 (3), 304-320.

Modava, M. and Akbarizadeh, G., 2017. Coastline extraction from SAR images using spatial fuzzy clustering and the active contour method. International Journal of Remote Sensing, 38(2), pp.355-370.

Martz, L.W. and Garbrecht, J., 1992. Numerical definition of drainage network and subcatchment areas from digital elevation models. Computers & Geosciences, 18(6), pp.747-761.

Martz, L.W. and Garbrecht, J., 1998. The treatment of flat areas and depressions in automated drainage analysis of raster digital elevation models. Hydrological processes, 12(6), pp.843-855.

Martz, L.W. and Garbrecht, J., 1999. An outlet breaching algorithm for the treatment of closed depressions in a raster DEM. Computers & Geosciences, 25(7), pp.835-844.

Minke, A.G., Westbrook, C.J. and van der Kamp, G., 2010. Simplified volume-area-depth method for estimating water storage of prairie potholes. Wetlands, 30(3), pp.541-551.

Miller, J.J., Acton, D.F. and St. Arnaud, R.J., 1985. The effect of groundwater on soil formation in a morainal landscape in Saskatchewan. Canadian Journal of Soil Science, 65(2), pp.293-307.

Morena, L.C., Pearce, C., Olfert, L., Elder, C., and Rolland, P. 2004. RADARSAT-2 order handling and mission planning. Canadian Journal of Remote Sensing, Vol. 30, No. 3, pp. 304–320.

Parmuchi, M.G., Karszenbaum, H. and Kandus, P., 2002. Mapping wetlands using multi-temporal RADARSAT-1 data and a decision-based classifier. Canadian Journal of Remote Sensing, 28(2), pp.175-186.

Pal, N.R. and Pal, S.K., 1993. A review on image segmentation techniques. Pattern recognition, 26(9), pp.1277-1294.

Pietroniro, A., Prowse, T. and Peters, D.L., 1999. Hydrologic assessment of an inland freshwater delta using multi-temporal satellite remote sensing. Hydrological Processes, 13(16), pp.2483-2498.

Pomeroy, J. W., and D. M. Gray, 1995: Snow cover accumulation, relocation and management. National Hydrology Research Institute Science Rep. 7, 144 pp. [Available from National Hydrology Research Institute, Saskatoon, SK S7K 0J5, Canada.]

Pomeroy, J.W., Shook, K., Fang, X., Dumanski, S., Westbrook, C. and Brown, T., 2014. Improving and testing the prairie hydrological model at Smith Creek Research Basin. Centre for Hydrology, University of Saskatchewan.

Pounds, N. J., 1963. Political Geography, New York

Pulvirenti, L., Pierdicca, N., Chini, M. and Guerriero, L., 2011. An algorithm for operational flood mapping from Synthetic Aperture Radar (SAR) data using fuzzy logic. Natural Hazards and Earth System Sciences, 11(2), p.529.

Raney, R.K., Runge, H., Bamler, R., Cumming, I.G. and Wong, F.H., 1994. Precision SAR processing using chirp scaling. IEEE Transactions on geoscience and remote sensing, 32(4), pp.786-799.

Ran, Y.H., Li, X., Lu, L. and Li, Z.Y., 2012. Large-scale land cover mapping with the integration of multi-source information based on the Dempster–Shafer theory. International Journal of Geographical Information Science, 26(1), pp.169-191.

Ramsey III, E., Rangoonwala, A., Middleton, B. and Lu, Z., 2009. Satellite optical and radar data used to track wetland forest impact and short-term recovery from Hurricane Katrina. Wetlands, 29(1), pp.66-79.

Richard, A.J., Jia, X., 2006. Remote Sensing Digital Image Analysis: Introduction, 4th ed. Springer-Verleg Berlin Heldelberg, Germany, p. 3.

Rosenberry, D.O. and Winter, T.C., 1997. Dynamics of water-table fluctuations in an upland between two prairie-pothole wetlands in North Dakota. Journal of Hydrology, 191(1-4), pp.266-289.

Rundquist, D.C., Narumalani, S. and Narayanan, R.M., 2001. A review of wetlands remote sensing and defining new considerations.

SAR processing with Geomatica. 2016. Available online: www.pcigeomatics.com/pdf/TrainingGuide-Geomatica. Version 2.5

Sawunyama, T.E.N.D.A.I., Senzanje, A. and Mhizha, A., 2006. Estimation of small reservoir storage capacities in Limpopo River Basin using geographical information systems (GIS) and remotely sensed surface areas: Case of Mzingwane catchment. Physics and Chemistry of the Earth, Parts A/B/C, 31(15-16), pp.935-943.

Schott, J.R., 2007. Remote sensing: the image chain approach. Oxford University Press on Demand.

Schumann, G., Hostache, R., Puech, C., Hoffmann, L., Matgen, P., Pappenberger, F. and Pfister, L., 2007. High-resolution 3-D flood information from radar imagery for flood hazard management. IEEE Transactions on Geoscience and Remote Sensing, 45(6), pp.1715-1725.

Sethre, P.R., Rundquist, B.C. and Todhunter, P.E., 2005. Remote detection of prairie pothole ponds in the Devils Lake Basin, North Dakota. GIScience & Remote Sensing, 42(4), pp.277-296.

Sheng, Y. and Xia, Z.G., 1996, May. A comprehensive evaluation of filters for radar speckle suppression. In Geoscience and Remote Sensing Symposium, 1996. IGARSS'96.'Remote Sensing for a Sustainable Future.', International (Vol. 3, pp. 1559-1561). IEEE.

Shook K, Pomeroy J. 2012. Changes in the hydrological character of rainfall on the Canadian prairies. Hydrological Processes 26(12): 1752–1766. DOI: 10.1002/hyp.9383

Shook, K., Pomeroy, J.W., Spence, C. and Boychuk, L., 2013. Storage dynamics simulations in prairie wetland hydrology models: evaluation and parameterization. Hydrological Processes, 27(13), pp.1875-1889.

Silveira, M. and Heleno, S., 2009. Separation between water and land in SAR images using region-based level sets. IEEE Geoscience and Remote Sensing Letters, 6(3), pp.471-475.

Sokol, J., NcNairn, H. and Pultz, T.J., 2004. Case studies demonstrating the hydrological applications of C-band multipolarized and polarimetric SAR. Canadian Journal of Remote Sensing, 30(3), pp.470-483.

Solbo, S., Malnes, E., Guneriussen, T., Solheim, I. and Eltoft, T., 2003, July. Mapping surface-water with Radarsat at arbitrary incidence angles. In Geoscience and Remote Sensing Symposium, 2003. IGARSS'03. Proceedings. 2003 IEEE International (Vol. 4, pp. 2517-2519). IEEE.

Sloan, C. E. 1972. Ground-water hydrology of prairie potholes in North Dakota. U. S. Geological Survey Professional Paper 585, (C): C1–C28.

Todhunter PE, Rundquist BC. 2004. Terminal lake flooding and wetland expansion in Nelson County, North Dakota. Phys Geogr 25:68–85.

Townsend, P.A., 2002. Relationships between forest structure and the detection of flood inundation in forested wetlands using C-band SAR. International Journal of Remote Sensing, 23(3), pp.443-460.

Töyrä, J. and Pietroniro, A., 2005. Towards operational monitoring of a northern wetland using geomatics-based techniques. Remote Sensing of Environment, 97(2), pp.174-191.

Töyrä, J., Pietroniro, A., Martz, L.W. and Prowse, T.D., 2002. A multi-sensor approach to wetland flood monitoring. Hydrological processes, 16(8), pp.1569-1581.

Töyra¨, J., Pietroniro, A. and Martz, L., 2001. Multisensor hydrologic assessment of a freshwater wetland. Remote sensing of environment, 75, 162173.

Touzi, R., Boerner, W.M., Lee, J.S. and Lueneburg, E., 2004. A review of polarimetry in the context of synthetic aperture radar: concepts and information extraction. Canadian Journal of Remote Sensing, 30(3), pp.380-407.

Touzi, R., Lopes, A. and Bousquet, P., 1988. A statistical and geometrical edge detector for SAR images. IEEE Transactions on geoscience and remote sensing, 26(6), pp.764-773.

Toutin, T. 2011. "Corrigendum to the paper "State-of-the-art of geometric correction of remote sensing data: a data fusion perspective"." International Journal of Image and Data Fusion, 2, pp. 283–286.

Tulbure, M.G. and Broich, M., 2013. Spatiotemporal dynamic of surface water bodies using Landsat time-series data from 1999 to 2011. ISPRS Journal of Photogrammetry and Remote Sensing, 79, pp.44-52.

Tulbure, M.G., Broich, M., Stehman, S.V. and Kommareddy, A., 2016. Surface water extent dynamics from three decades of seasonally continuous Landsat time series at subcontinental scale in a semi-arid region. Remote Sensing of Environment, 178, pp.142-157.

Tulbure, M.G. and Broich, M., 2013. Spatiotemporal dynamic of surface water bodies using Landsat time-series data from 1999 to 2011. ISPRS Journal of Photogrammetry and Remote Sensing, 79, pp.44-52.

Uher, J., Grenier, C. and Lefebvre, G., 2004. RARSAT-2 SAR Antenna. Canadian journal of remote sensing, 30 (3), 287-294.

Ulaby, F.T., Batlivala, P.P. and Dobson, M.C., 1978. Microwave backscatter dependence on surface roughness, soil moisture, and soil texture: Part I-bare soil. IEEE Transactions on Geoscience Electronics, 16(4), pp.286-295.

Van der Kamp, G., Hayashi, M., 2009. Groundwater-wetland ecosystem interaction in the semiarid glaciated plains of North America. Hydrogeol. J. 17, 203–214.

Van der Kamp, G., Hayashi, M. and Gallen, D., 2003. Comparing the hydrology of grassed and cultivated catchments in the semi-arid Canadian prairies. Hydrological Processes, 17(3), pp.559-575.

Van der Kamp, G., Keir, D. and Evans, M.S., 2008. Long-term water level changes in closed-basin lakes of the Canadian prairies. Canadian Water Resources Journal, 33(1), pp.23-38.

Vachon, P. and DeLisle, D., 2012, June. From Radarsat-2 to Radarsat constellation mission data continuity. In Proceedings of the Advanced SAR oceanography (SeaSAR) Symposium, Tromsø, Norway (pp. 18-22).

Wang, L. and Liu, H., 2006. An efficient method for identifying and filling surface depressions in digital elevation models for hydrologic analysis and modelling. International Journal of Geographical Information Science, 20(2), pp.193-213.

White, L., Brisco, B., Pregitzer, M., Tedford, B. and Boychuk, L., 2014. RADARSAT-2 beam mode selection for surface water and flooded vegetation mapping. Canadian Journal of Remote Sensing, 40(2), pp.135-151.

Winter, T.C. and Rosenberry, D.O., 1998. Hydrology of prairie pothole wetlands during drought and deluge: a 17-year study of the Cottonwood Lake wetland complex in North Dakota in the perspective of longer term measured and proxy hydrological records. Climatic Change, 40(2), pp.189-209.

Woodhouse, I.H., 2006. Introduction to microwave remote sensing. CRC press.

Xu, H., 2006. Modification of normalised difference water index (NDWI) to enhance open water features in remotely sensed imagery. International journal of remote sensing, 27(14), pp.3025-3033.

Zhang, F., Xie, C., Li, K., Xu, M., Wang, X. and Xia, Z., 2012. Forest and deforestation identification based on multitemporal polarimetric RADARSAT-2 images in Southwestern China. Journal of Applied Remote Sensing, 6(1), p.063527.

Appendix A

Radarsat-2 product (SLC) description, (MDA, 2016)

	Standard	Fine	Wide Fine	Multi-Look Fine	Wide Multi-Look Fine	Ultra-Fine	Wide Ultra-Fine	Wide	Extended High	Extended Low
Pixel Data Representation	16-bit I and 16-bit Q									
Product Characteristics										
Nominal Image Coverage (ground range x azimuth)	100 km x 100 km	50 km x 50 km	150 km x 150 km	50 km x 50 km	90 km x 50 km	20 km x 20 km	50 km x 50 km	150 km x 150 km	75 km x 75 km	170 km x 170 km
Approximate Pixel Spacing (slant range x azimuth)	8.0 m x 5.1m (S1-2) 11.8 m x 5.1m (S3-8)	4.7 m x 5.1 m	4.7 m x 5.1 m	2.7 m x 2.9 m	2.7 m x 2.9 m	1.3 m x 2.1 m	1.3 m x 2.1 m	11.8 m x 5.1 m	11.8 m x 5.1 m	8.0 m x 5.1 m
Approximate Image Size (pixels x lines)	6000 x 20000	8000 x 10000	24000 x 30000	14000 x 17000	25000 x 17000	9000 x 9500	24000 x 24000	7000 x 30000	5600 x 15000	6200 x 33000
Nominal Product Volume	460 MBytes per polarization	300 MBytes per polarization	2800 Mbytes per polarization	900 MBytes	1600 MBytes	350 MBytes	2200 MBytes	800 MBytes per polarization	320 MBytes	780 MBytes
Processing Parameters										
Number of Range Looks	1	1	1	1	1	1	1	1	1	1
Number of Azimuth Looks	1	1	1	1	1	1	1	1	1	1
Range Look Bandwidth	17.3 MHz (S1-2) 11.6 MHz (S3-8)	30 MHz	30 MHz	50 MHz	50 MHz	100 MHz	100 MHz	11.6 MHz	11.6 MHz	17.3 MHz
Azimuth Look Bandwidth	900 Hz	900 Hz	900 Hz	1500 Hz	1500 Hz	2430 Hz	2430 Hz	900 Hz	900 Hz	900 Hz
Range Spectral Weighting	Kaiser (2.4)	Kaiser (2.4)	Kaiser (2.4)	Kaiser (2.4)	Kaiser (2.4)	Kaiser (2.4)	Kaiser (2.4)	Kaiser (2.4)	Kaiser (2.4)	Kaiser (2.4)
Azimuth Spectral Weighting	Kaiser (2.4)	Kaiser (2.4)	Kaiser (2.4)	Kaiser (2.4)	Kaiser (2.4)	Kaiser (2.4)	Kaiser (2.4)	Kaiser (2.4)	Kaiser (2.4)	Kaiser (2.4)
Typical Image Quality Characteristics										
Nominal Slant Range Resolution	9.0 m (S1-2) 13.5 m (S3-8)	5.2 m	5.2 m	3.1 m	3.1 m	1.6 m	1.6 m	13.5 m	13.5 m	9.0 m
Nominal Azimuth Resolution	7.7 m	7.7 m	7.7 m	4.6 m	4.6 m	2.8 m	2.8 m	7.7 m	7.7 m	7.7 m
Equiv. No. of Independent Looks	1	1	1	1	1	1	1	1	1	1
Noise-Equivalent Sigma-Zero	-29±2.5 dB	-26±3.5 dB	-24±2 dB	-20±4 dB	-19±5 dB	-26.5±5 dB	-22±7 dB	-28±2 dB	-28±4 dB	-27±2 dB
Radiometric Error	<1 dB	<1 dB	<1 dB	<1 dB	<1.5 dB	<1 dB	<1 dB	<1 dB	<1 dB	<1 dB
Absolute Location Error	< 20 m	< 15 m	< 15 m	< 15 m	< 15 m	< 15 m	< 15 m	< 20 m	< 20 m	< 30 m
Relative Phase Error	<3°	<3°	<3°	<3°	<3°	<3°	<3°	<3°	<3°	<3°

	Standard Quad Pol.	Wide Standard Quad Pol.	Fine Quad Pol.	Wide Fine Quad Pol.	Spotlight	Extra-Fine (Full Res)	Extra-Fine (Fine Res)	Extra-Fine (Std Res)	Extra-Fine (Wide Res)
Pixel Data Representation	16-bit I and 16-bit Q								
Product Characteristics									
Nominal Image Coverage (ground range x azimuth)	25 km x 25 km	50 km x 25 km	25 km x 25 km	50 km x 25 km	18 km x 8 km	125 km x 125 km	125 km x 125 km	125 km x 125 km	125 km x 125 km
Approximate Pixel Spacing (slant range x azimuth)	8.0 m x 5.1m (near) 11.8 m x 5.1m (far)	8.0mx5.1m (near) 11.8mx5.1m (far)	4.7 m x 5.1 m	4.7 m x 5.1 m	1.3 m x 0.4 m	2.7 x 2.9	4.3 x 5.8	7.1 x 5.8	10.6 x 5.8
Approximate Image Size (pixels x lines)	1500 x 5000	3000 x 5000	3300 x 5000	6600 x 5000	8000 x 20000	27000 x 43000	17000 x 22000	10000 x 22000	7000 x 22000
Nominal Product Volume	30 MBytes per polarization	60 MBytes per polarization	60 MBytes per polarization	130 MBytes per polarization	400 to 1500 MBytes	4600 MBytes	1500 MBytes	900 MBytes	600 MBytes
Processing Parameters									
Number of Range Looks	1	1	1	1	1	1	1	1	1
Number of Azimuth Looks	1	1	1	1	1	1	1	1	1
Range Look Bandwidth	17.3 MHz (near) 11.6 MHz (far)	17.3 MHz (near) 11.6 MHz (far)	30 MHz	30 MHz	100MHz	50 MHz	30 MHz	17.3 MHz	11.6 MHz
Azimuth Look Bandwidth	900 Hz	900 Hz	900 Hz	900 Hz	9400 Hz	1500 Hz	900 Hz	900 Hz	900 Hz
Range Spectral Weighting	Kaiser (2.4)	Kaiser (2.4)	Kaiser (2.4)	Kaiser (2.4)	Kaiser (2.4)	Kaiser (2.4)	Kaiser (2.4)	Kaiser (2.4)	Kaiser (2.4)
Azimuth Spectral Weighting	Kaiser (2.4)	Kaiser (2.4)	Kaiser (2.4)	Kaiser (2.4)	Kaiser (3.5)	Kaiser (2.4)	Kaiser (2.4)	Kaiser (2.4)	Kaiser (2.4)
Typical Image Quality Characteristics									
Nominal Slant Range Resolution	9.0m (SQ1-SQ11) 13.5m (SQ12-SQ31)	9.0m (SQ1-SQ11) 12.8m (SQ12-SQ21)	5.2 m	5.2 m	1.6 m	3.1 m	5.2 m	8.9 m	13.3 m
Nominal Azimuth Resolution	7.6 m	7.6 m	7.6 m	7.6 m	0.8 m	4.6 m	7.6 m	7.6 m	7.6 m
Equiv. No. of Independent Looks	1	1	1	1	1	1	1	1	1
Noise-Equivalent Sigma-Zero	-38±3 dB	-35±6 dB	-35±4 dB	-33±6 dB	Centre: -28.5 ± 4.5dB Corners: -19.5 ± 3.5dB	-21±2.5 dB	-23±2.5 dB	-23±2.5 dB	-23±2.5 dB
Radiometric Error	<1 dB	<1 dB	<1 dB	<1 dB	<1 dB	<1 dB	<1 dB	<1 dB	<1 dB
Absolute Location Error	< 20 m	< 20 m	< 15 m	< 15 m	< 15 m	< 15 m	< 15 m	< 15 m	< 15 m
Relative Phase Error	<3°,5° inter-pol	<3°,5° inter-pol	<3°,5° inter-pol	<3°,<5° inter-pol	<3°	<3°	<3°	<3°	<3°

Appendix B

Standard, Wide, Extended Low, Extended High, Fine, Wide Fine Swaths (MDA 2016)

Beam/ Swath Position	Near Incidence Angle (degs)	Far Incidence Angle (degs)	Nominal Near Range Resolution (m)	Nominal Far Range Resolution (m)		Beam/ Swath Position	Near Incidence Angle (degs)	Far Incidence Angle (degs)	Nominal Near Range Resolution (m)	Nominal Far Range Resolution (m)
S1	20.0	27.2	26.8	20.0		F23	30.0	33.4	10.4	9.4
S2	24.0	31.3	22.6	17.6		F23F	30.8	34.2	10.2	9.3
S3	30.4	37.0	27.0	22.7		F22N	31.6	34.9	9.9	9.1
S4	33.5	39.7	24.8	21.4		F22	32.4	35.7	9.7	8.9
S5	36.3	42.2	23.1	20.3		F22F	33.1	36.4	9.5	8.8
S6	41.2	46.5	20.7	18.8		F21N	33.9	37.1	9.3	8.6
S7	44.4	49.3	19.5	18.0		F21	34.7	37.8	9.1	8.5
S8	48.5	52.1	18.2	17.3		F21F	35.4	38.5	9.0	8.3
						F1N	36.1	39.2	8.8	8.2
W1	20.0	31.9	40.0	25.9		F1	36.9	39.9	8.7	8.1
W2	30.6	39.5	26.9	21.5		F1F	37.7	40.6	8.5	8.0
W3	38.7	45.3	21.9	19.2		F2N	38.5	41.4	8.4	7.9
						F2	39.3	42.1	8.2	7.8
F0W1	20.4	31.9	14.9	9.9		F2F	40.0	42.8	8.1	7.7
F0W2	30.6	39.5	10.2	8.2		F3N	40.7	43.5	8.0	7.6
F0W3	38.7	45.3	8.3	7.3		F3	41.4	44.1	7.9	7.5
						F3F	42.0	44.7	7.8	7.4
EL1	10.0	23.1	52.7	23.3		F4N	42.7	45.3	7.7	7.3
						F4	43.3	45.9	7.6	7.2
EH1	48.5	52.1	18.2	17.3		F4F	43.9	46.5	7.5	7.2
EH2	50.0	53.4	17.8	17.0		F5N	44.5	47.1	7.4	7.1
EH3	51.6	54.9	17.4	16.7		F5	45.2	47.7	7.3	7.0
EH4	54.4	57.0	16.8	16.3		F5F	45.7	48.2	7.3	7.0
EH5	55.5	58.1	16.6	16.1		F6N	46.3	48.7	7.2	6.9
EH6	56.8	59.3	16.3	15.9		F6	46.9	49.3	7.1	6.9
						F6F	47.5	49.9	7.1	6.8

Appendix C

Summary of RADARSAT-2 Beam Modes and Product Characteristics

BEAM MODE	PRODUCT [1, 2]	Nominal Pixel Spacing [3,4] [Rng × Az] (m)	Nominal Resolution [5] [Rng x Az] (m)	Nominal Scene Size [6] [Rng x Az] (km)	Nominal Incidence Angle Range [deg]	No. Looks [Rng x Az]	Polarization Options	BAQ Level (bits)
Spotlight	SLC	1.3 x 0.4	1.6 x 0.8	18 x 8	20 to 54 [(7)]	1 x 1	Single Co or Cross (HH or VV or HV or VH)	3
	SGX	1 or 0.8 x 1/3	4.6 – 2.0 x 0.8					
	SGF	0.5 x 0.5						
	SSG, SPG	0.5 x 0.5						
Ultra-Fine	SLC	1.3 x 2.1	1.6 x 2.8	20 x 20	20 to 54 [(7)]	1 x 1	Single Co or Cross (HH or VV or HV or VH)	3
	SGX	1 x 1 or 0.8 x 0.8	4.6 – 2.0 x 2.8					
	SGF	1.56 x 1.56						
	SSG, SPG	1.56 x 1.56						
Wide Ultra-Fine	SLC	1.3 x 2.1	1.6 x 2.8	50 x 50	29 to 50	1 x 1	Single Co or Cross (HH or VV or HV or VH)	2
	SGX	1 x 1	3.3 – 2.1 x 2.8					
	SGF	1.56 x 1.56						
	SSG, SPG	1.56 x 1.56						
Multi-Look Fine	SLC	2.7 x 2.9	3.1 x 4.6	50 x 50	30 to 50	1 x 1	Single Co or Cross (HH or VV or HV or VH)	3
	SGX	3.13 x 3.13	10.4 – 6.8 x 7.6			2 x 2		
	SGF	6.25 x 6.25						
	SSG, SPG	6.25 x 6.25						
Wide Multi-Look Fine	SLC	2.7 x 2.9	3.1 x 4.6	90 x 50	29 to 50	1 x 1	Single Co or Cross (HH or VV or HV or VH)	2
	SGX	3.13 x 3.13	10.8 – 6.8 x 7.6			2 x 2		
	SGF	6.25 x 6.25						
	SSG, SPG	6.25 x 6.25						
Extra-Fine	SLC (Full Res)	2.7 x 2.9	3.1 x 4.6	125 x 125	22 to 49	1 x 1	Single Co or Cross (HH or VV or HV or VH)	2
	SLC (Fine Res)	4.3 x 5.8	5.2 x 7.6					
	SLC (Std Res)	7.1 x 5.8	8.9 x 7.6					
	SLC (Wide Res)	10.6 x 5.8	13.3 x 7.6					
	SGX (1 look)	2.0 x 2.0	8.4 – 4.1 x 4.6			1 x 1		
	SGX (4 looks)	3.13 x 3.13	14 – 6.9 x 7.6			2 x 2		
	SGX (28 looks)	5.0 x 5.0	24 – 12 x 23.5			4 x 7		
	SGF (1 look)	3.13 x 3.13	8.4 – 4.1 x 4.6			1 x 1		
	SGF (4 looks)	6.25 x 6.25	14 – 6.9 x 7.6			2 x 2		
	SGF (28 looks)	8.0 x 8.0	24 – 12 x 23.5			4 x 7		
	SSG, SPG	3.13 x 3.13	8.4 – 4.1 x 4.6			1 x 1		
Fine	SLC	4.7 x 5.1	5.2 x 7.7	50 x 50	30 to 50	1 x 1	Single Co or Cross (HH or VV or HV or VH) or Dual (HH+HV or VV+VH)	3
	SGX	3.13 x 3.13	10.4 – 6.8 x 7.7					
	SGF	6.25 x 6.25						
	SSG, SPG	6.25 x 6.25						
Wide Fine	SLC	4.7 x 5.1	5.2 x 7.7	150 x 150	20 to 45	1 x 1	Single Co or Cross (HH or VV or HV or VH) or Dual (HH+HV or VV+VH)	3
	SGX	3.13 x 3.13	14.9 – 7.3 x 7.7					
	SGF	6.25 x 6.25						
	SSG, SPG	6.25 x 6.25						
Standard	SLC	8 or 11.8 x 5.1	9.0 or 13.5 x 7.7	100 x 100	20 to 52	1 x 1	Single Co or Cross (HH or VV or HV or VH) or Dual (HH+HV or VV+VH)	3
	SGX	8 x 8	26.8 – 17.3 x 24.7			1 x 4		
	SGF	12.5 x 12.5						
	SSG, SPG	12.5 x 12.5						
Wide	SLC	11.8 x 5.1	13.5 x 7.7	150 x 150	20 to 45	1 x 1	Single Co or Cross (HH or VV or HV or VH) or Dual (HH+HV or VV+VH)	3
	SGX	10 x 10	40.0 – 19.2 x 24.7			1 x 4		
	SGF	12.5 x 12.5						
	SSG, SPG	12.5 x 12.5						

BEAM MODE	PRODUCT [1, 2]	Nominal Pixel Spacing [3,4] [Rng × Az] (m)	Nominal Resolution [5] [Rng x Az] (m)	Nominal Scene Size [6] [Rng x Az] (km)	Nominal Incidence Angle Range [deg]	No. Looks [Rng x Az]	Polarization Options	BAQ Level (bits)
Extended High	SLC	11.8 x 5.1	13.5 x 7.7	75 x 75	49 to 60	1 x 1	Single (HH only)	3
	SGX	8 x 8	18.2 – 15.9 x 24.7			1 x 4		
	SGF	12.5 x 12.5						
	SSG, SPG	12.5 x 12.5						
Extended Low	SLC	8.0 x 5.1	9.0 x 7.7	170 x 170	10 to 23	1 x 1	Single (HH only)	3
	SGX	10 x 10	52.7 – 23.3 x 24.7			1 x 4		
	SGF	12.5 x 12.5						
	SSG, SPG	12.5 x 12.5						
Fine Quad-Pol	SLC	4.7 x 5.1	5.2 x 7.6	25 x 25	18 to 49	1 x 1	Quad (HH+VV+HV+VH)	3
	SGX	3.13 x 3.13	16.5 – 6.8 x 7.6					
	SSG, SPG	3.13 x 3.13						
Wide Fine Quad-Pol	SLC	4.7 x 5.1	5.2 x 7.6	50 x 25	18 to 42	1 x 1	Quad (HH+VV+HV+VH)	3
	SGX	3.13 x 3.13	17.3–7.8 x 7.6					
	SSG, SPG	3.13 x 3.13						
Standard Quad-Pol	SLC	8 or 11.8 x 5.1	9.0 or 13.5 x 7.6	25 x 25	18 to 49	1 x 1	Quad (HH+VV+HV+VH)	3
	SGX	8 x 3.13	28.6 – 17.7 x 7.6					
	SSG, SPG	8 x 3.13						
Wide Standard Quad-Pol	SLC	8 or 11.8 x 5.1	9.0 or 13.5 x 7.6	50 x 25	18 to 42	1 x 1	Quad (HH+VV+HV+VH)	3
	SGX	8 x 3.13	30.0 –16.7 x 7.6					
	SSG, SPG	8 x 3.13						
ScanSAR Narrow	SCN, SCF, SCS	25 x 25	81–38 x 40-70	300 x 300	20 to 46	2 x 2	Single Co or Cross (HH or VV or HV or VH) or Dual (HH+HV or VV+VH)	SCNA:4 SCNB:3
ScanSAR Wide	SCW, SCF, SCS	50 x 50	163–73 x 78-106	500 x 500	20 to 49	4 x 2	Single Co or Cross (HH or VV or HV or VH) or Dual (HH+HV or VV+VH)	4
Ship Detection (Detection of Vessels)	SCF	40 x 40	103-71 x 40-81	450 x 500	35 to 56	16 x 2 [(8)]	Single (HH only)	1
	SCS	20 x 20	33-23 x 19-77			5 x 1		
Ocean Surveillance	SCF	50 x 50	118-53 x 53-104	500 x 500	20 to 50	6 x 2 [(8)]	Single Co or Cross (HH or VV or HV or VH) or Dual (HH+HV or VV+VH)	2
	SCS	35 x 25	80-36 x 27-99			4 x 1		

NOTES:

1. Products available: Single Look Complex (SLC); Path Image Plus (SGX); Path Image (SGF); ScanSAR Narrow (SCN); ScanSAR Wide (SCW); ScanSAR Fine (SCF); ScanSAR Sampled (SCS); Map Image (SSG); Precision Map Image (SPG).
2. SLC, SGX, SGF, SCN, SCW, SCF and SCS are georeferenced and aligned with the satellite track. SSG and SPG are geocorrected on a map projection (SPG requires ground control points).
3. For SLC products the range pixel spacing is in radar slant range. For other georeferenced products (i.e. for ground range products) the range pixel spacing is in ground range. For geocorrected products the pixel spacings are in map projected coordinates (horizontal x vertical).
4. For SLC products the azimuth pixel spacing depends on the pulse repetition frequency.
5. Range resolution is in radar slant range for SLC products and ground range for all other products. Ground range resolution varies with incidence angle.
6. Actual scene size may vary with incidence angle.
7. Incidence angles above 50 degrees in the Spotlight and Ultra-Fine beam modes are not yet available commercially.
8. For Ship Detection and Ocean Surveillance modes, azimuth multi-looking of SCF products is done by spatial averaging and decimation by a factor of 2.
9. All modes and product characteristics are subject to change. Some restrictions may apply.
10. The RADARSAT-2 SAR sensor is extremely flexible and programmable post-launch; nominal resolution and swath width are examples of programmable characteristics. Custom and new beam modes will be introduced in response to client needs and market conditions.